



TRANSIENT AND STEADY PERFORMANCE OF AN
ION ROCKET THRUST AUGMENTOR

prepared for
NATIONAL AERONAUTICS AND SPACE ADMINISTRATION

Grant Ns G-570 GPO PRICE \$ _____

CFSTI PRICE(S) \$ _____

January 1966

Hard copy (HC) 4.00

Microfiche (MF) 1.00

ff 653 July 65

FLUID DYNAMICS AND DIFFUSION LABORATORY
COLLEGE OF ENGINEERING
COLORADO STATE UNIVERSITY
FORT COLLINS, COLORADO

FACILITY FORM 502

N66 36786	N66 36790
(ACCESSION NUMBER)	(THRU)
130	1
(PAGES)	(PAGES)
CR-77855	28
(NASA CR OR TMX OR AD NUMBER)	(CATEGORY)

CER66-67VAS3

FINAL REPORT

**TRANSIENT AND STEADY PERFORMANCE OF AN
ION ROCKET THRUST AUGMENTOR**

Prepared for

NATIONAL AERONAUTICS AND SPACE ADMINISTRATION

January 1966

Grant Ns G-570

**Technical Management
NASA Lewis Research Center
Cleveland, Ohio
Electron Propulsion Office
John Ferrante**

CER66-67VAS3

NASA FINAL REPORT

SUMMARY

INTRODUCTION

OPERATION OF AN ION ACCELERATOR WITH ELECTRON EMISSION TEST SET UP

EXPERIMENTAL RESULTS

- a) Maximum Beam Current
- b) Optimum Operation of the Electron Emitter
- c) Optics Study
- d) Electron Collector Study

APPENDIX A

OPERATION OF A SECONDARY ELECTRON-ELECTRON BOMBARDMENT ✓

APPENDIX B

EXPERIMENTAL DATA

APPENDIX C

Langevin Probe Measurements ✓ ~~COLLECTOR PROBE STUDY OF THE ION BEAM~~

APPENDIX D

SECONDARY ELECTRON EMISSION STUDY ✓

APPENDIX E

HEAT TRANSFER FROM LARGE DIAMETER PIRANI GAGES OPERATING DOWN TO A MICROTorr ✓

TRANSIENT AND STEADY PERFORMANCE OF AN ION ROCKET THRUST AUGMENTOR

SUMMARY

The increase in beam current of an ion thruster by the emission of electrons in the accelerator region has been evaluated in detail. It is demonstrated that conditions of ion limited current is possible for all accelerator conditions investigated when electron emission is employed. The electrons are emitted between the positive ionizer and the negative accelerator. The optimum operation of the electron emission accelerator is found to be for conditions where the electrons are in a potential trap between the accelerators. The electron trap observations suggest the accelerator of ions is not due to counter current electron flow. The results also demonstrate that the effect is not directly an effect due to secondary electron emission at the ionizer. An adequate explanation of the electron emission accelerator was not found.

Detailed measurements of the beam spreading effects of the electron emission accelerator are given. All measurements were made with simple Pierce type accelerator geometry, which unfortunately are designed for space charge limited beam flows. However, since the electron emission accelerator operated at ion limited flow conditions, the actual focus of the beam was quite poor. Design of an accelerator

which would focus at ion limited flow operation was not accomplished during the funding period.

A new type of secondary electron-electron bombardment ion thruster was operated successfully during the year. This engine employed the electron emitter in the accelerator to also ionize the cesium. This thruster can employ the best features of the electron bombardment type ionizer together with the electron emission accelerator to obtain a highly efficient ion thruster.

Detailed evaluation of the secondary emission of electrons of a porous tungsten surface was also obtained. The emission shows selected energy levels where the number of secondary electrons emitted is markedly reduced. These results are quite different from solid tungsten emission and will require a more detailed study of the structure of porous tungsten in order to obtain an adequate explanation.

INTRODUCTION

The use of ion thrusters to propel space vehicles depends on the electrostatic acceleration of ions. The electrostatic accelerator uses an electro-optical gun similar to that used for electron acceleration. The electro-optical gun is limited in the number of ions it may accelerate, due to space charge limitations. Sandborn and Baldwin, ref. 1, have demonstrated that the space charge limitations can be removed by introducing electrons into the accelerator region.

The effect of electrons in the accelerator region is not understood. First observations appeared to indicate that the electrons produced secondary electrons at the ionizer, and these secondary electrons altered the space charge limits. The present program was designed to investigate the secondary electron model. Systematic evaluation of the electron-accelerator phenomena has led to a rejection of the secondary electron model. The acceleration is found to work best when the electrons are trapped in the accelerator region. The trapped electron concept is demonstrated in the present report; however, no consistent model to explain the phenomena was forthcoming at the present time. The major finding of the research must be that in all cases investigated it was possible to obtain ion limited operation of an ion thruster.

EXPERIMENTAL PROGRAM

The experimental study was carried out in the NASA-CSU vacuum facility. This facility was described in the previous contract reports, ref. 2. During the current research year a 16-inch diameter by 26-inch long "bell jar" was added to the end of the facility to increase the flexibility of the system.

Several ion thruster systems were operated during the current experimental program. The most detailed study was carried out with a one-half inch diameter, porous tungsten ionizer, ion thruster built by

the Electro-Optical Company. Details of the EOS ion thruster are included in Apx. A.

A counter-current, electron bombardment, ion thruster system was also studied during the current year. Details of this system was reported in the midterm report, ref. 2. A second type of electron emission, porous steel, thruster was operated on a first trial basis during the later part of the current study. This thruster was a first attempt to incorporate the "electron trap" rather than counter current-electron bombardment ionization.

Figure 1 is a schematic and photograph of the "electron trap" thruster system. A one-half inch diameter porous steel (approximate 5μ pore size) flow distributor was employed as the positive electrode. The electron emitters were a grid of 0.01-inch diameter throated-tungsten wires. The distance between the porous steel flow distributor and the electron emitters was approximately 0.25 inches and the negative accelerator was 0.50 inches from the porous steel. Mechanical difficulty in operating the first system was encountered due to sputtering of the copper negative accelerator. Due to the apparent great increase in ion beam power directly around the grid wire, the copper negative accelerator was etched almost completely through in lines directly corresponding to the wire grid. The etching was over a very narrow region no more than approximately twice the thickness of the grid wires. The operation was terminated when the sputtered copper coated the insulators around the grid wires.

An experimental study of the emission of secondary electrons from porous tungsten surfaces is reported in Apx. D. Appendix E is a report of the evaluation of a sensitive pressure gage which was developed during the current study. The pressure gage was intended as a possible neutral atom detector, but only the pressure aspects were completed during the current program.

Appendix C demonstrates preliminary studies made with a collector probe in the ion beam. This study was made as a possible means of demonstrating that the apparent increase in ion beam density was in no way due to accelerated electrons.

RESULTS AND DISCUSSION

The major result of the research program is summarized in fig. 2. Figure 2 shows the maximum observed ion beam currents obtained with the electron emission accelerator and the 1/2-inch EOS thruster. The solid curve is computed as the ion limited curve for the EOS porous tungsten as reported by Kuskevics and Thompson, ref. 3. The maximum acceleration voltage obtained during the research program was $\Delta V = 8000$ volts (limited by power supplies available). Thus, the maximum available space charge limited beam current available for the $L/D = 1$ accelerator was computed to be 4.8 milliamps. With electron emission, the maximum observed beam current was 32 milliamps. Over the operating range shown in fig. 2, it may be concluded that the only restriction on the beam current is the number of ions

available to accelerate. The points at 425°C (note as $\Delta V = 4000$ volts) do not quite reach the ion limited curve, but this was due to the inability to produce sufficient electron emission. No evidence of space charge restrictions are found in this accelerator system.

The second important result of the experimental program is the demonstration of the electron trap rather than counter flow operation of the accelerator. This effect is demonstrated in fig. 3 and demonstrated in more detail in Apx. A. Figure 3 demonstrates the effect of ion beam current due to the potential on the electron emitter. The electron emitter must be below 500 volts in order that the electrons do not have to climb a potential hill to escape the emitter field. This conclusion is based on an analog two-dimension determination of the potential field. It may, of course, be a wrong conclusion that the two-dimension analog is valid for the ion limited flow, although it is hard to conceive that it can have changed the field potentials by over 300 volts. It appears to be conclusively demonstrated that the electron emission accelerator works best when the trend is away from a counter flow of electrons and toward an electron trap.

Detailed studies of the operation of an accelerator with a local potential "hill" have been made. Appendix B is a tabulation of the experimental measurements, including the ion beam distribution and spreading. This study was undertaken to obtain data for the design of an efficient electron emission accelerator system. The problem of an adequate focusing system for the electron emission accelerator system

is the most important problem in the practical application of this phenomena. The present study failed to produce a good focusing control of these large ion beams. The apparent approach is to design an accelerator system for one operating level, rather than a general system, as is the case of space charge limited accelerator systems.

Also, included in Apx. B is the data obtained for the electron emission-porous steel ion thruster. This data demonstrates that this new type of hybrid engine is feasible; however, more detailed development of the concept is required. The engine may operate either as an electron bombardment ionization or surface ionization at the electron grid wires. No doubt a combination of the two possible means of ionization would prove the most efficient.

The use of collector probes in ion beams has been reported by several investigators. Appendix C shows data obtained with a 0.013-inch diameter by 1/4-inch long tungsten wire collector probe in the present experimental program. This data was taken to assure that the apparent increase in ion beam power with electron emission could not be due to very high energy electrons. The results indicate no major change in electron density due to emission in the accelerator region. As might be expected, the major effect on electron density (and the resulting "plasma potential"), is related directly to the screen potential around the engine.

Details and results on the study of secondary electron emission from porous tungsten is given in detail in Apx. D. The development of a heat transfer gage for measurement of low pressures (10^{-5} to 10^{-6} torr), which was supported in part by the present grant, is reported in Apx. E.

CONCLUSIONS

Two specific conclusions have been obtained from the present research program.

1. A electron emission accelerator system can produce ion limited beam currents for all conditions investigated.
2. The electron emission accelerator depends on an electron trap rather than a counter flow of electrons.

REFERENCES

1. Sandborn, V. A. and Baldwin, L. V., Hot-Wire Calorimeter Study of Ion Production and Acceleration. AIAA Jour., vol. 2, no. 4, pp. 660-666, 1964.
2. Transient and Steady Performance of an Ion Rocket Thrust Augmentor. NASA Grant Ns-570. Fluid Dynamics and Diffusion Laboratory, Colorado State University, Fort Collins, Colorado, 1964-1965.
3. Kuskevics, G. and Thompson, B. L., Comparison of Commercial Spherical Powder and Wire Bundle Tungsten Ionizers. AIAA Jour., vol. 2, no. 2, 1964.

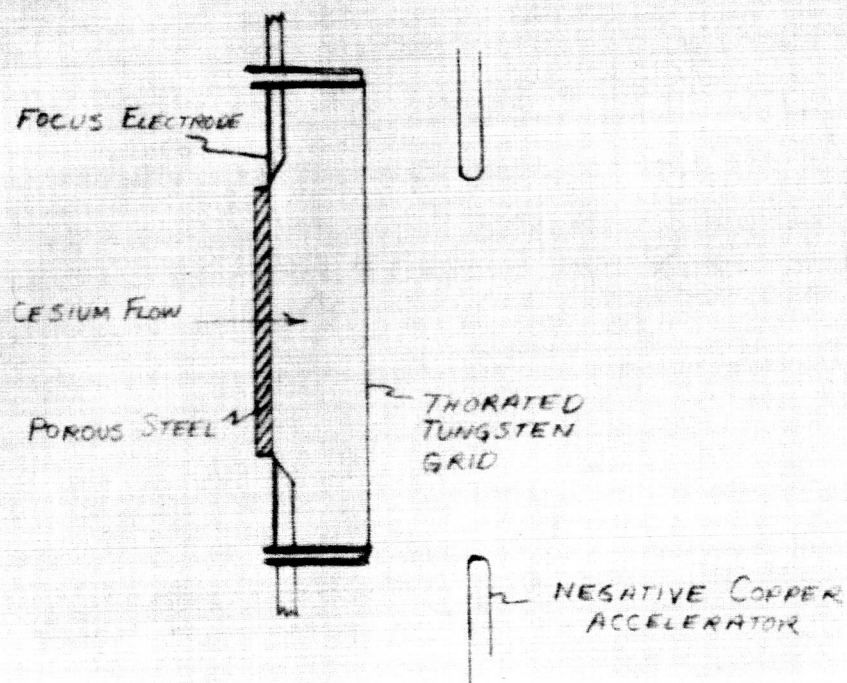
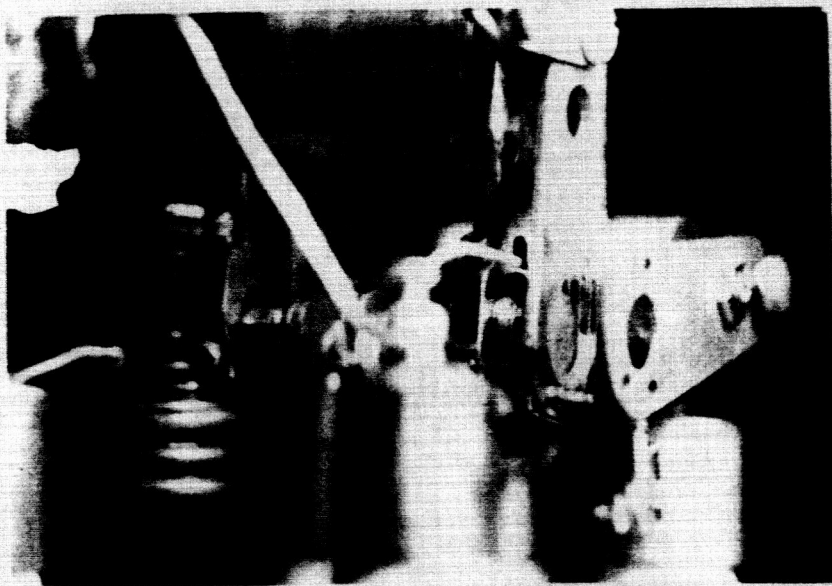


FIGURE 1: ELECTRON EMISSION, POROUS STEEL ION THRUSTER.

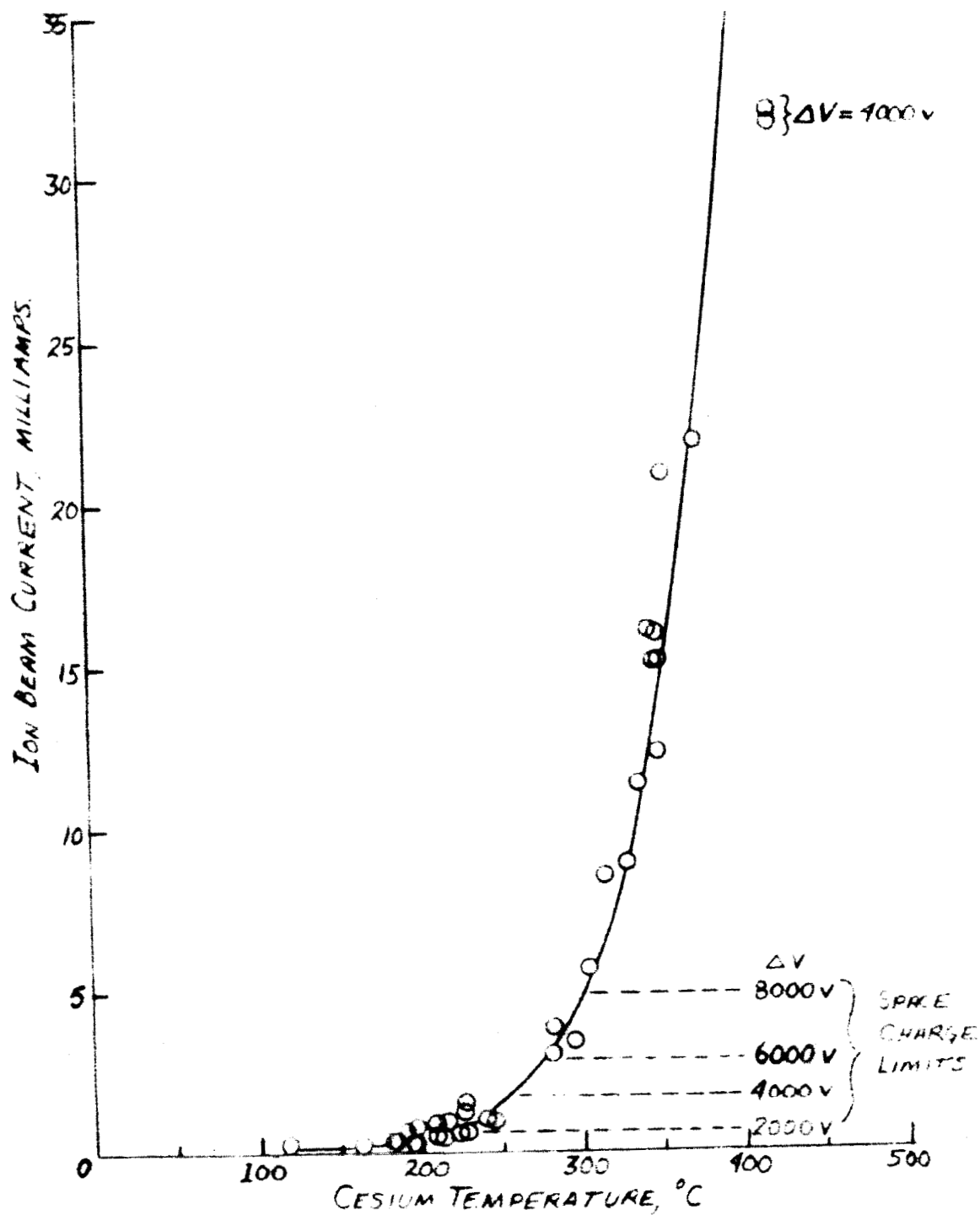


FIGURE 2-MAXIMUM ION CURRENT OBSERVED FOR A $\frac{1}{4}$ INCH DIAMETER ECS ION THRUSTER. $L/D=1$

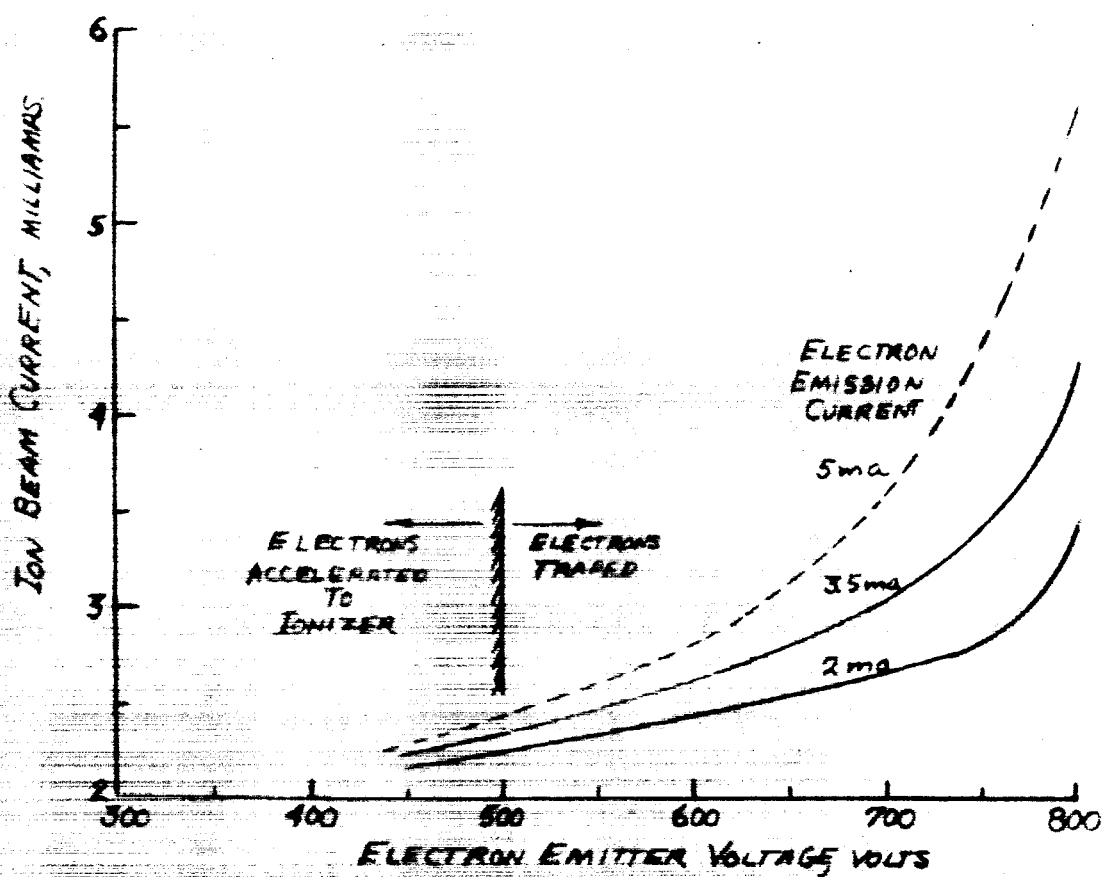


FIGURE 3.- ION CURRENT INCREASE AS A FUNCTION OF EMITTER VOLTAGE AND ELECTRON EMISSION.

~~APPENDIX A~~OPERATION OF A ONE-HALF INCH DIAMETER ION THRUSTOR
WITH A COUNTERCURRENT ELECTRON ACCELERATOR

by

V. A. Sandborn, J. E. Braly, and R. L. Atchley

SUMMARY

An Electro Optical Systems, one-half inch diameter, porous tungsten surface ionization thruster was operated with a countercurrent electron accelerator system. Increases over space charge limited ion beam currents up to a factor of 7 was obtained with the present geometry. The increase in ion current was proportional to the electron emission. The operation of the electron emitter was limited by electrical breakdown between the ionizer and the emitter. Evidence is also found to indicate that the electron emitter tends to over focus the beam. The over focus leads to excessive impingement on the negative accelerator for the present accelerator geometry.

INTRODUCTION

This memorandum is a report of tests of the countercurrent electron accelerator operation with a $\frac{1}{2}$ inch diameter EOS ion thruster. Specific details on the countercurrent accelerator were reported previously in references 1, 2, and 3. Previous tests were made on a $\frac{1}{4}$ inch porous tungsten ion thruster. These previous tests were only partly successful due to the small size of the accelerator system. The present large size ionizer has resulted in a more successful operation of the accelerator. The present test is part of a systematic set to determine the characteristics of the electron emission accelerator. The major attempt is to improve the optics of the system for a practical accelerator system. The ion density obtained from the accelerator system over the space charge limited operation appears limited only by the number of ions present. On the other hand it is found that major defocusing of the ion beam occurs when the electron emission is employed.

TEST SETUP AND PROCEDURE

The present test was made in the NASA-CSU vacuum facility. The pressure for the test was 7×10^{-6} mm Hg. This pressure was somewhat higher than normal for the facility, and was traced to a leak in a cooling line to the ion thruster. Details of the facility and the instrumentation are given in reference 1 and 2.

EOS ION THRUSTOR.- A one-half inch diameter, porous tungsten, contact ionization, cesium ion thruster was employed in this test. The complete thruster with a simple focus and negative accelerator electrode was built by the Electro Optical Systems Company. The focus electrode was made of 0.060 inch molybdenum sheet with a 45° tapered hole for the ionizer. A 0.060 inch copper negative accelerator is employed. The copper accelerator uses a 7/16 inch diameter hole with a radius of 0.030 at the edge. This system was employed directly for the present tests, with the addition of a loop of 0.01 diameter thorated-tungsten wire placed 1/8 of an inch from the ionizer. The thorated-tungsten electron emitter was 0.547 inches in diameter, as shown in figure 1. The EOS electrode system would appear to over focus the ion beam near the ionizer and then over spread it at the negative accelerator. The result may be a reasonable focus at the exit, however, the addition of the electron emitter loop will alter the focus. The optics of the wire loop with electron emission simply is not known at the present time. The wire loop was constructed as shown in figure 1. A small gap was left near the top of the loop simply to make the loop easy to mount. The calorimeter surveys indicate a slightly non symmetry to the ion beam, indicating the gap in the loop caused a disturbance. In future tests the loop was constructed to prevent the gap.

The present test was run at an ionizer temperature of approximately 1080°C . The ionizer voltage was held at +1000 volts and the negative accelerator was operated at -3000 volts. The main parameter varied was the electron emitter voltage and current. The negative acceleration was at a distance of 0.50 inches from the ionizer.

SPACE CHARGE LIMITED OPERATION.- The use of an electron emission source within an ion accelerator system has been shown to greatly improve the power that can be obtained from a space charge limited accelerator system. The first attempts of Sandborn and Baldwin, ref. 4, produced a reasonably well focused ion beam. Since this first set of data, it has been possible to produce the high current density beams (see reference 2). However, the increase is always done at the expense of badly defocusing the ion beam. The present test is one in a series to attempt to better understand the defocusing and accelerator action of the countercurrent electron accelerator.

The accelerator voltages were set at +1000 and -3000 with the electron emitter loop set as near the ionizer voltage as possible (+990 volts). The cesium vaporizer was brought up to a temperature of 340⁰ C. The ionizer current for these conditions is shown plotted in figure 2. After the test a slight leak was discovered in the reservoir cap, which may in part explain to apparent difference between the measurements and the ion limited curve. The accelerator system for the conditions of figure 2 was space charge limited at a beam current of 1.22 milliamps. This is well below the Childs law prediction, and also well below the suggested correction for aperture effect given by Sandborn and Baldwin, ref. 4. Changing the electron emitter voltage, as shown in figure 3, was found to increase the ionizer current. It appears that the space charge limited calculation with aperture correction of 1.7 milliamps will be approached for a electron emitter voltage of roughly 350 volts. Unfortunately, the approach to theoretical space charge conditions also causes a sharp rise in the impingment on the negative accelerator.

A two-dimensional analog simulation of the accelerator system indicated that the electron emitter would have no effect on the electrical field at a potential of 500 volts. Figure 4 shows the undisturbed field (dashed curves) obtained from a resistance paper analog. The electric field for an electron emitter wire voltage of +990 volts is shown in figure 4 a) and that for an electron emitter voltage of +800 volts is shown in figure 4 b). The results of figure 4 would appear to indicate an over focusing of the beam near the ionizer. However, as shown by the insert on figure 3 the actual beam impingment on the negative accelerator was least for the 800 volt case. The 500 volt case caused the impingment to double.

The first impression from figure 4 was that it would be necessary to operate the electron emitter wire at voltages around 500 volts in order to improve the ion acceleration. For the two cases of 990 and 800 volts shown in figure 4 a) and 4 b) there is a dip in the voltage field between the wire and the ionizer (see sketch).

This might imply that the electron would be trapped at the emitter wire. This then would suggest that electrons from the wire are not likely to bombard the ionizer.

However, as shown in figure 5, the greatest increase was obtained at 800 volts rather than at 500 volts. (Electrical breakdown between the electron emitter and the ionizer prevented the operation of the 800 volt test beyond 5 milliamps emission. The 500 volt case was still steady at 10 millamps emission. However, it was not carried to higher emission currents for fear of burning out the electron emitter.) The impingement on the negative accelerator is plotted on figure 6 for the runs shown on figure 5.

The present results all indicated that a condition of an electron trap around the emission wire was required to greatly effect space charge ion acceleration. A further test of the results was made by moving the electron emitter out to a position half-way between the ionizer and the negative accelerator. The two-dimensional accelerator field lines for this condition are shown on figure 7. The "floating" potential of the electron emitter wire was +100 volts for the case of ionizer at +2000 volts and negative accelerator at -2000 volts. Operation of the electron emitter wire at +1500 volts in this field produced an ionizer beam current increase of roughly 7.5 times. Figure 8 is a comparison of the hot wire calorimeter trace of the beam before and after electron emission. Again the beam is poorly focused, and more than 70% of the ionizer beam current was caught by the negative accelerator. The common ground current increase was approximately a factor of five, which is that demonstrated by the calorimeter trace. Figure 9 is the figure corresponding to figure 5 for the different placement of the electron emission wire. Unfortunately, the poorer focus of the system of figure 7 (emitter half way between) led to a rather fast coating of all parts with cesium and sputtered copper.

The coating resulted in excessive leakage currents, which terminated the test prematurely. The hot wire calorimeter failed when it was being withdrawn from the larger beam of figure 8.

The present set of experiments appear to greatly alter the original concepts advanced to explain the operation of the "countercurrent" accelerator. Indeed it now appears that the electrons may not actually flow countercurrent to the ion beam. The two-dimensional analog is of course only a crude approximation to a system with a space charge ion cloud and electrons being emitted at the wire. However, if primary and secondary electrons were the major factor it would appear that the curves of figure 5 are reversed. Indeed the results of figure 5 for the 500 volt case is roughly explained by assuming the space charge cloud moves out to the electron emission wire location. The 500 volt case would correspond to the results found by Marazzi, ref. 5.

The second factor of concern is the reversal of current flow in the electron emission wire circuit as it is heated. Figure 9 shows a plot of the current flow for the electron emission wire at the half-way location of figure 7. Similar results were observed for the 800 and 750 volt cases of figure 5, however, at the time it was impossible to measure the reversed current flow. The first speculation to explain this unexpected behavior might be as follows:

- 1) With the unheated wire the impingement of ions on the wire produces a flow of electrons to the wire.
- 2) As the wire is heated neutral cesium atoms are ionized at the wire surface and electrons flow away from the wire.
- 3) When the wire is further heated more electrons than ions are produced and apparently some escape the vicinity of the wire.

The apparent production of cesium ions at the electron emitter masks the accelerator effect of the electrons. Further study will be required in which the number of neutral cesium atoms is reduced. The tests of figure 9 were done with an ionizer temperature of approximately 1200°C , which may be somewhat low for most efficient ionization. Even if it were assumed that the accelerator length were cut in half by the presence of the electron emitter, the space charge limited current would have been approximately 6 ma. Thus, it would be impossible to observe more than 6 millamps of current even if more ions are produced at the ionizer.

The run of figure 5 was done with the bare system exposed to the vacuum tank. As a check of possible external electrons affecting to measurements, a copper screen was placed around the system for the run of figure 7. Since the results are roughly the same for the two cases it is doubtful that external electrons had a major effect on any of the measurements. Figure 10 compares the hot wire calorimeter measurements with the common ground meter reading for the screened operation. Within the accuracy of evaluation the two independent measurements are in agreement.

The power required to heat the electron emitter to a given emission condition is much less when ions are present. For example it required a power of 10.4 watts to obtain a 1 milliamp emission for the curve of figure 9. In the no cesium present "cold" case a power of 16.4 watts could only produce an emission of 0.4 milliamps.

CONCLUDING REMARKS

The use of counter current electron accelerator to overcome space charge limits is again demonstrated. For the first time sufficient variation of parameters was possible to indicate definite trends to the process. At present the concept of secondary electron breaking up the space charge seems highly questionable. In general the two-dimensional analog use to estimate electrical fields is a reasonable first approximation. Certainly, the analog technique is valid for the straight forward surface ionizer type systems. Any effects of three-dimensionality or space charge are of second order importance. Whether it can be assumed that the presence of the electrons completely invalidates the two-dimensional analog is of course the major question. It is doubtful that the presence of electrons completely reverses the trends indicated by the analog, thus it is inescapable that the condition of an electron trap is necessary for the operation of the accelerator system.

REFERENCES

1. Transient and Steady Performance of an Ion Rocket Thrust Augmentor. Summary Report- NASA Grant Ns G-570. Fluid Dynamics and Diffusion Laboratory, Colorado State University, Fort Collins, Colorado, 1964.
2. Sandborn, V. A. and Kummer, J. W.: Preliminary Operation of a Ion Thruster with Provisions for a Countercurrent Electron Accelerator. RM No. 3, Fluid Dynamics and Diffusion Laboratory, Colorado State University, Fort Collins, Colorado, 1965.
3. Transient and Steady Performance of an Ion Rocket Thrust Augmentor. Interim Report- NASA Grant Ns G-570. Fluid Dynamics and Diffusion Laboratory, Colorado State University, Fort Collins, Colorado, 1965.
4. Sandborn, V. A. and Baldwin, L. V.: Hot-Wire Calorimeter Study of Ion Production and Acceleration. AIAA Journal, Vol. 2, No.4, pp.660-666, 1964.
5. Marazzi, C.A.: Secondary Emission Effects in Ion Beams. Thesis M S Electrical Engineering, Colorado State University, Fort Collins, Colorado, Nov. 1964 also in Transient and Steady Performance of an Ion Rocket Thrust Augmentor. Summary Report- NASA Grant Ns G- 570. Fluid Dynamics and Diffusion Laboratory, Colorado State University, Fort Collins, Colorado, 1964.

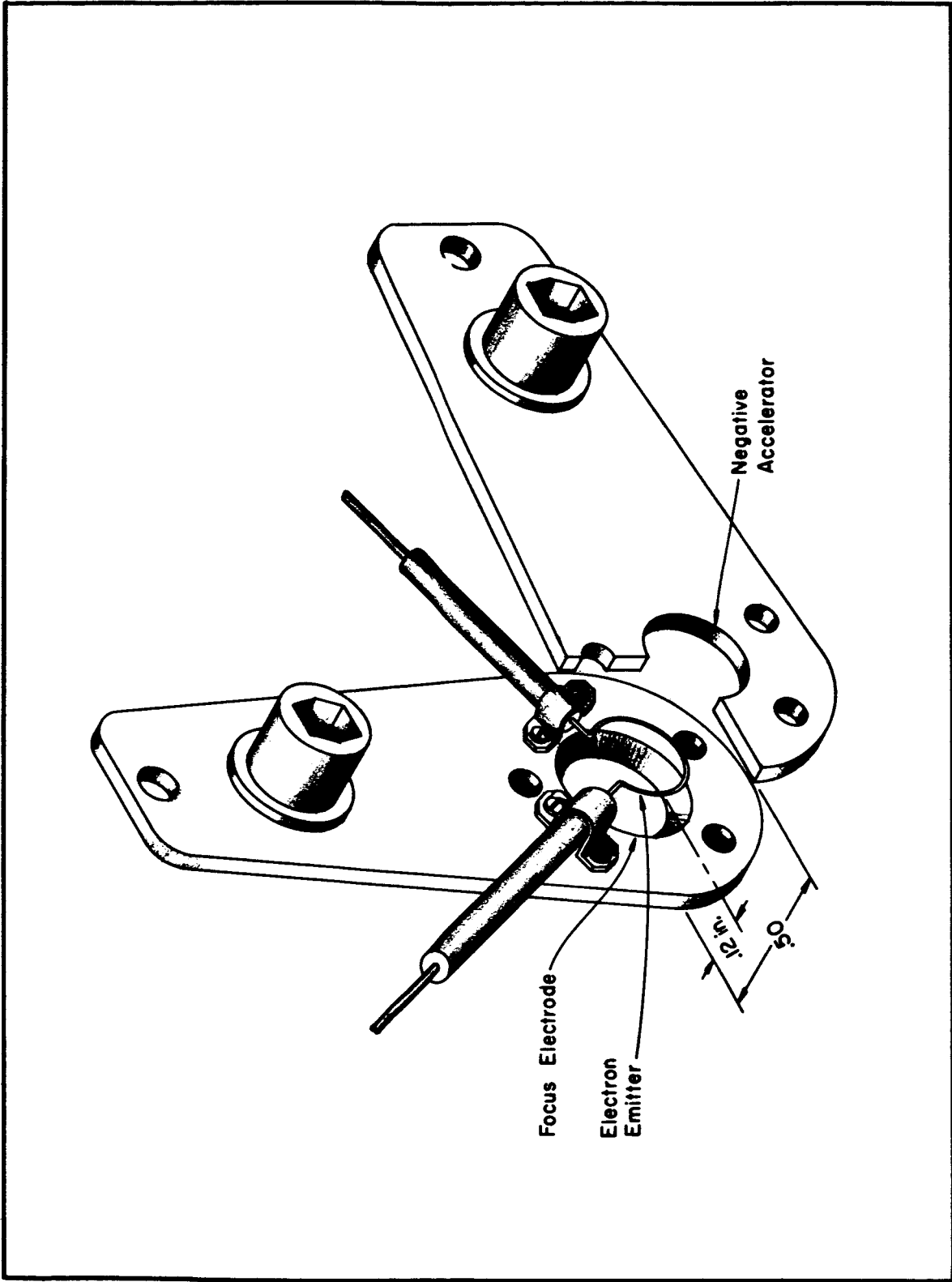


FIG. 1 Electron Emission Accelerator System.

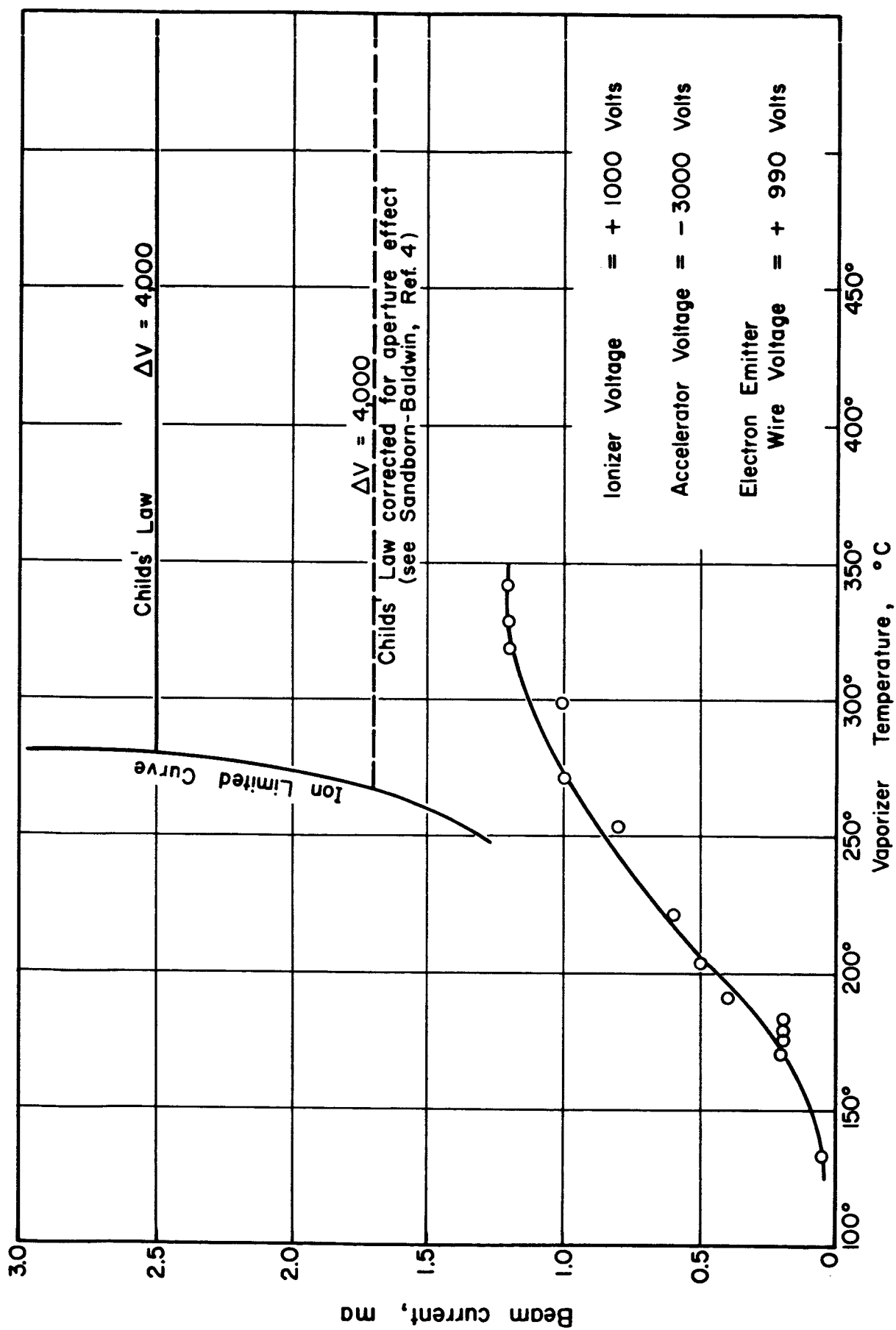


FIG. 2 Space charge limited operation compared with Childs' Law prediction.

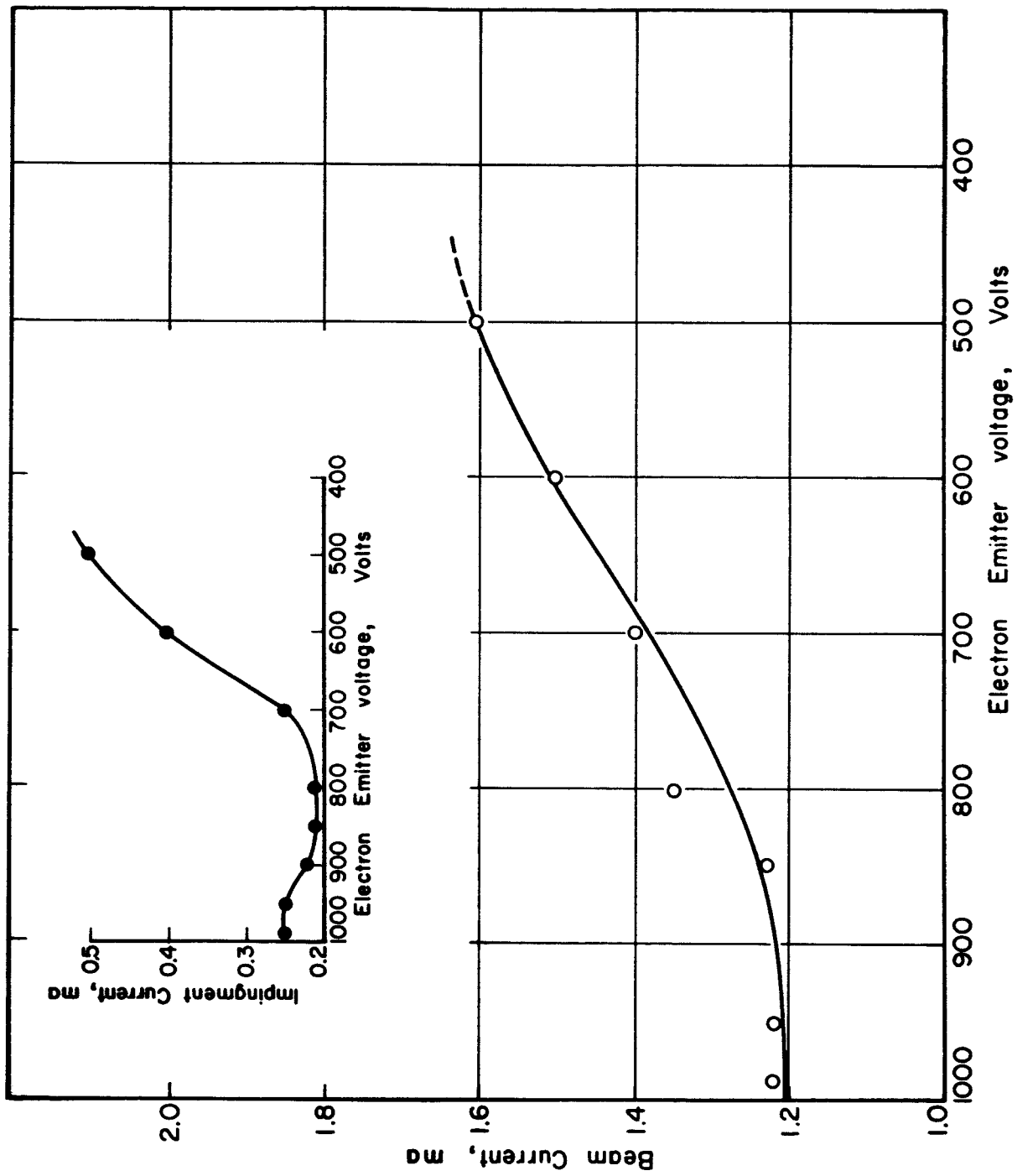
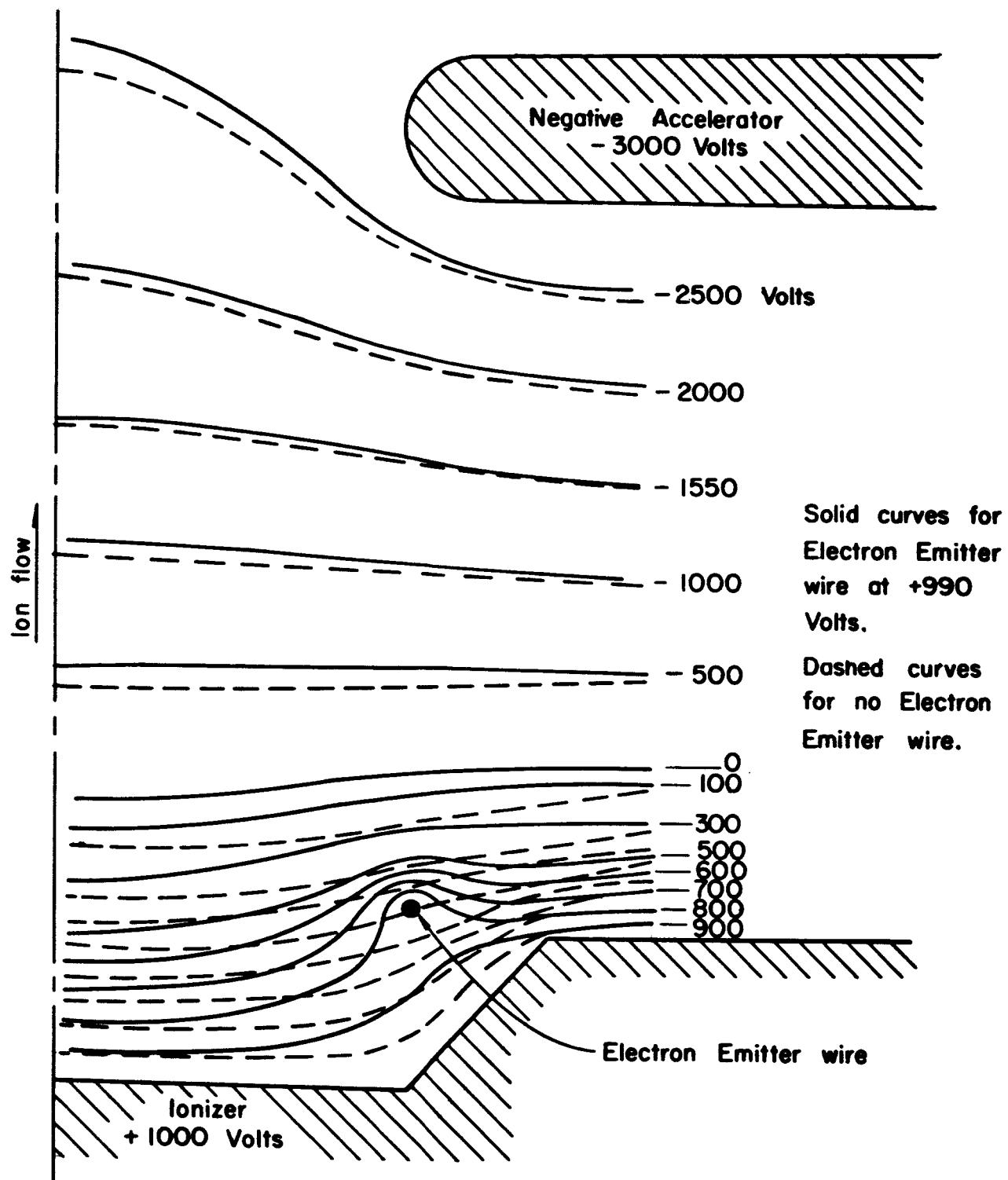
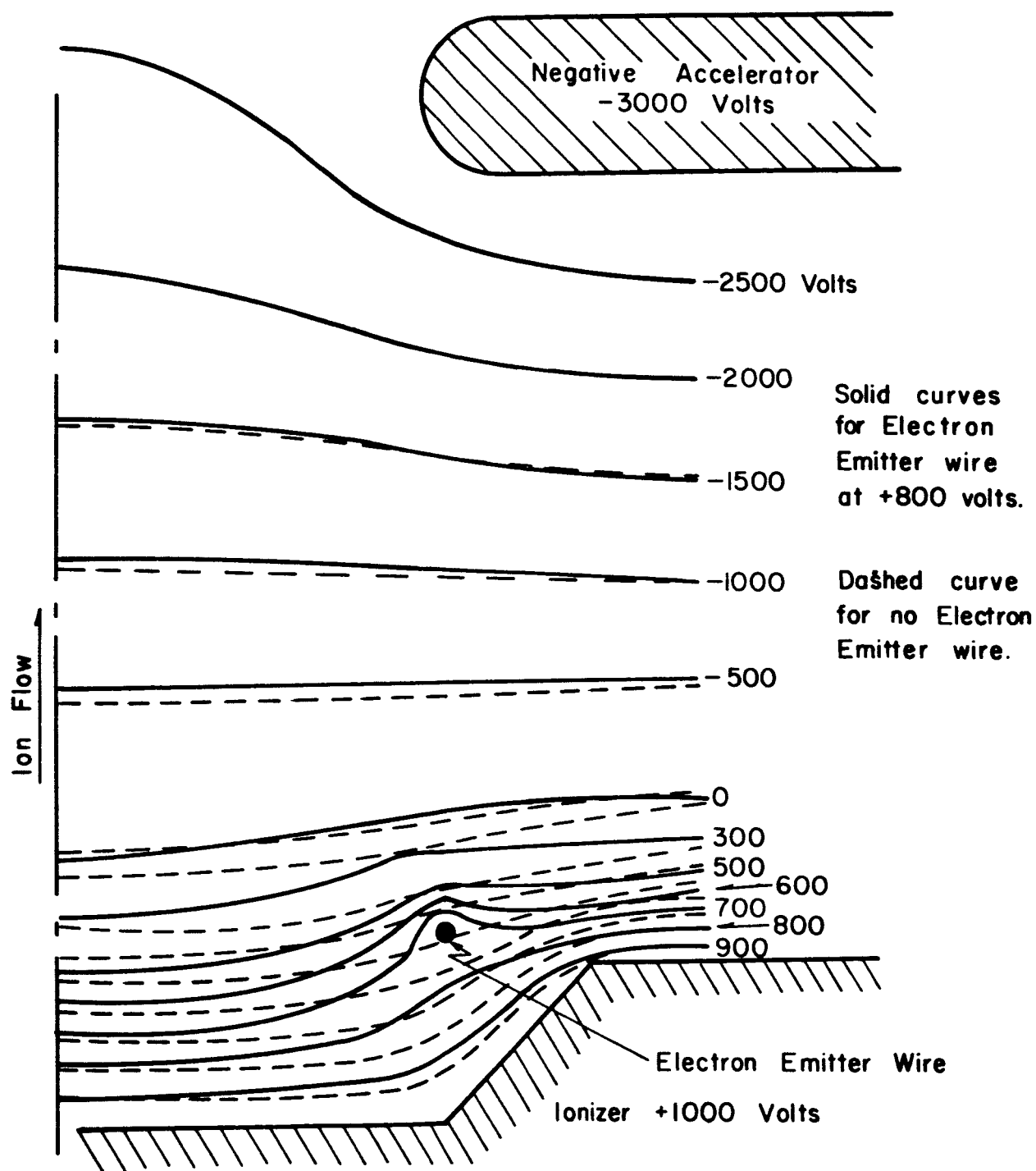


FIG. 3 Effect of varying Electron Emitter voltage without electron emission.



a.) Electron Emitter at +990 Volts

FIG. 4 Two-Dimensional analog of the accelerator voltage field with the Electron Emitter wire.



b) Electron Emitter At +800 Volts

FIG. 4 (concluded) Two-Dimensional analog of the accelerator voltage field with the Electron Emitter wire.

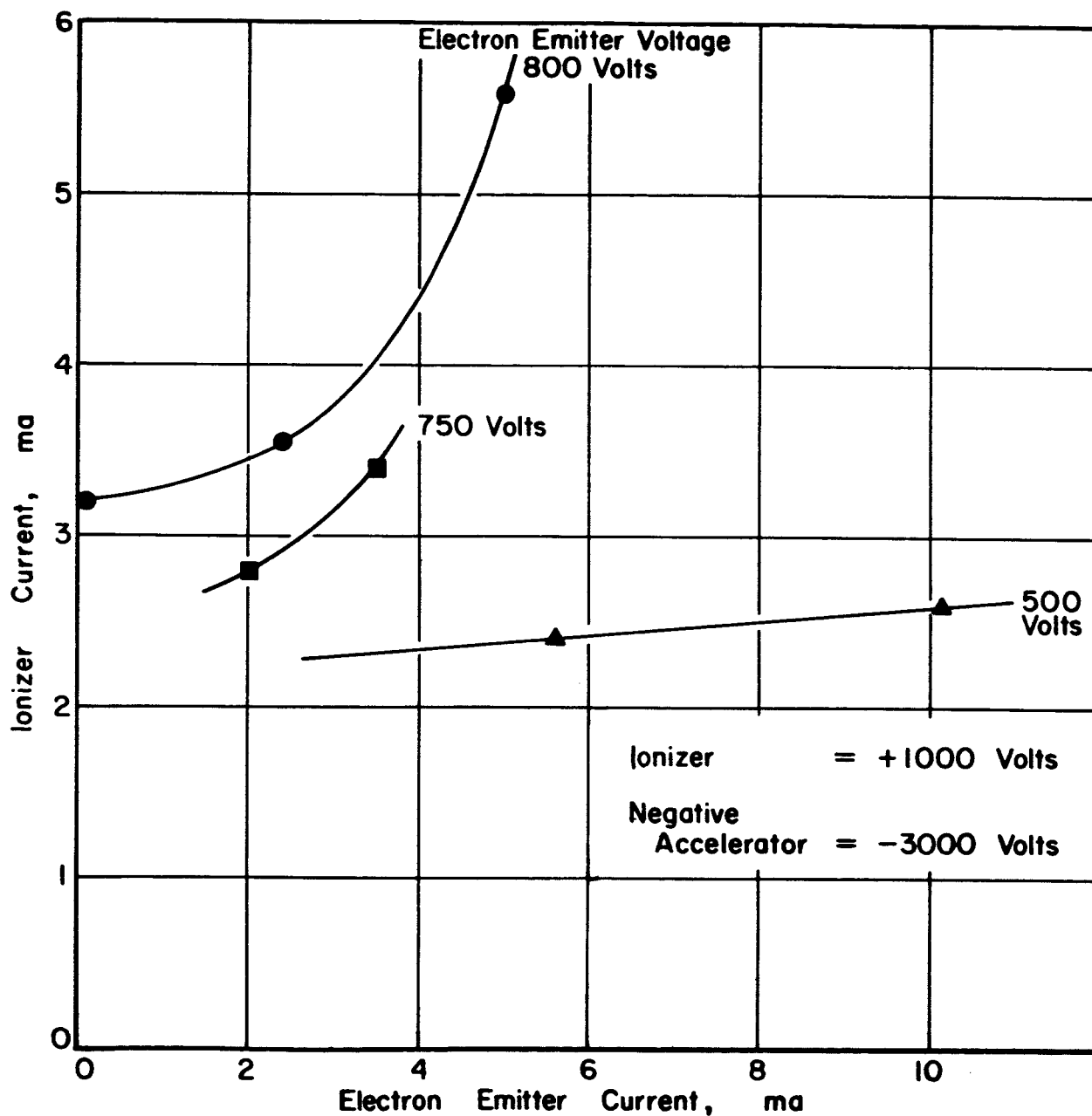


FIG. 5 Increase in ionizer current as a function of Electron Emitter Current.

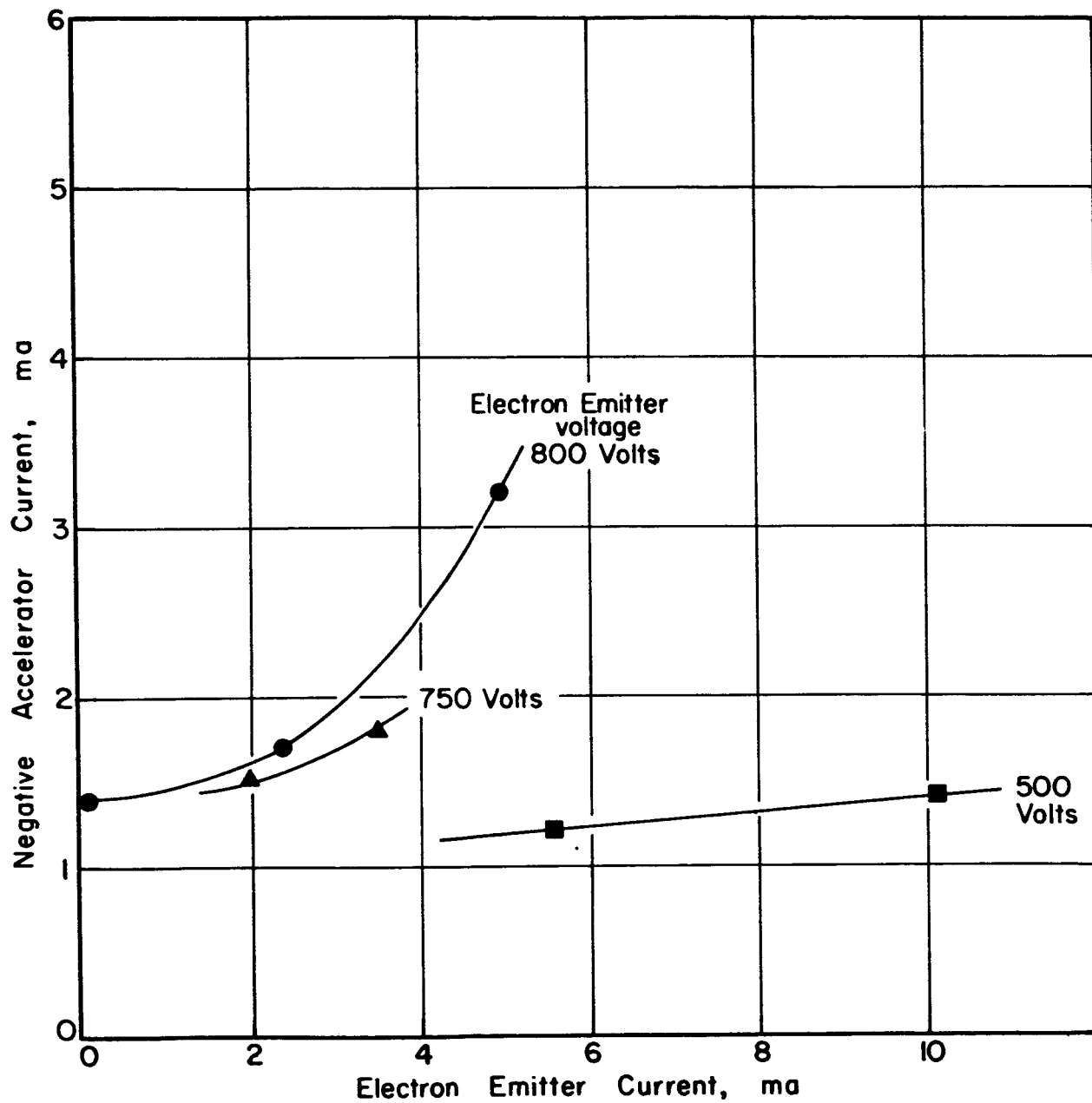


FIG. 6 Impingement current as a function of electron emission current.

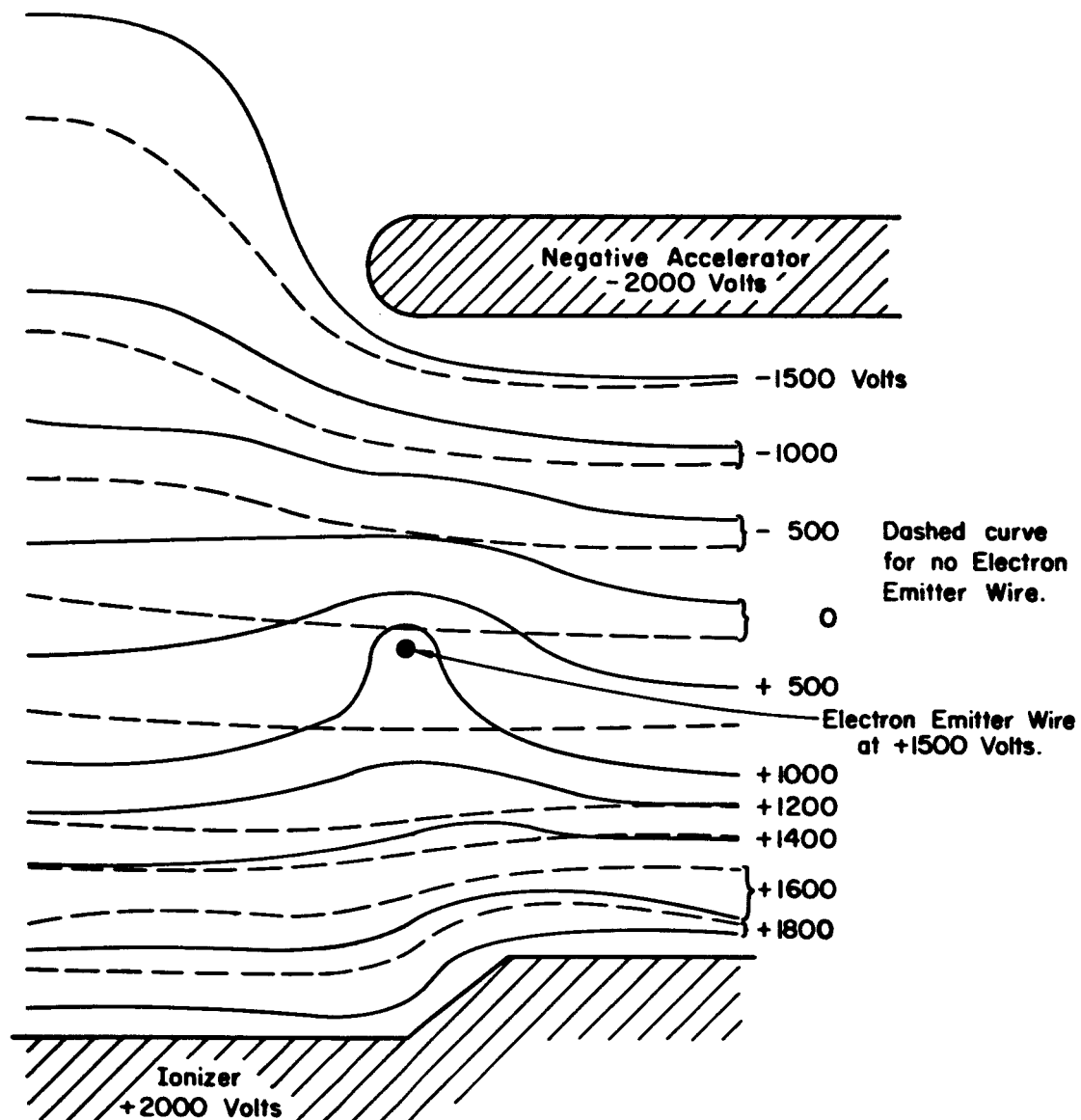
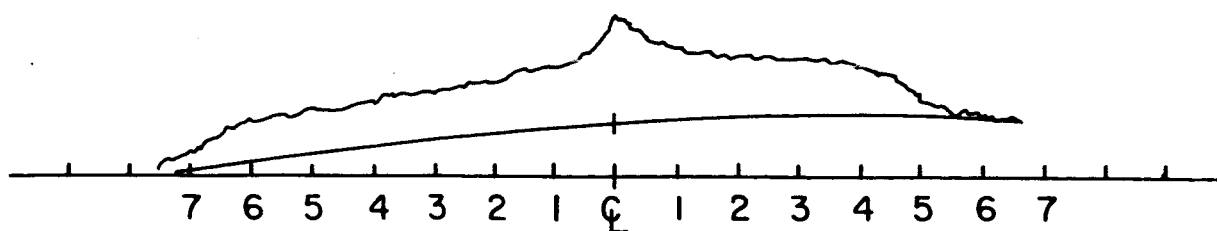
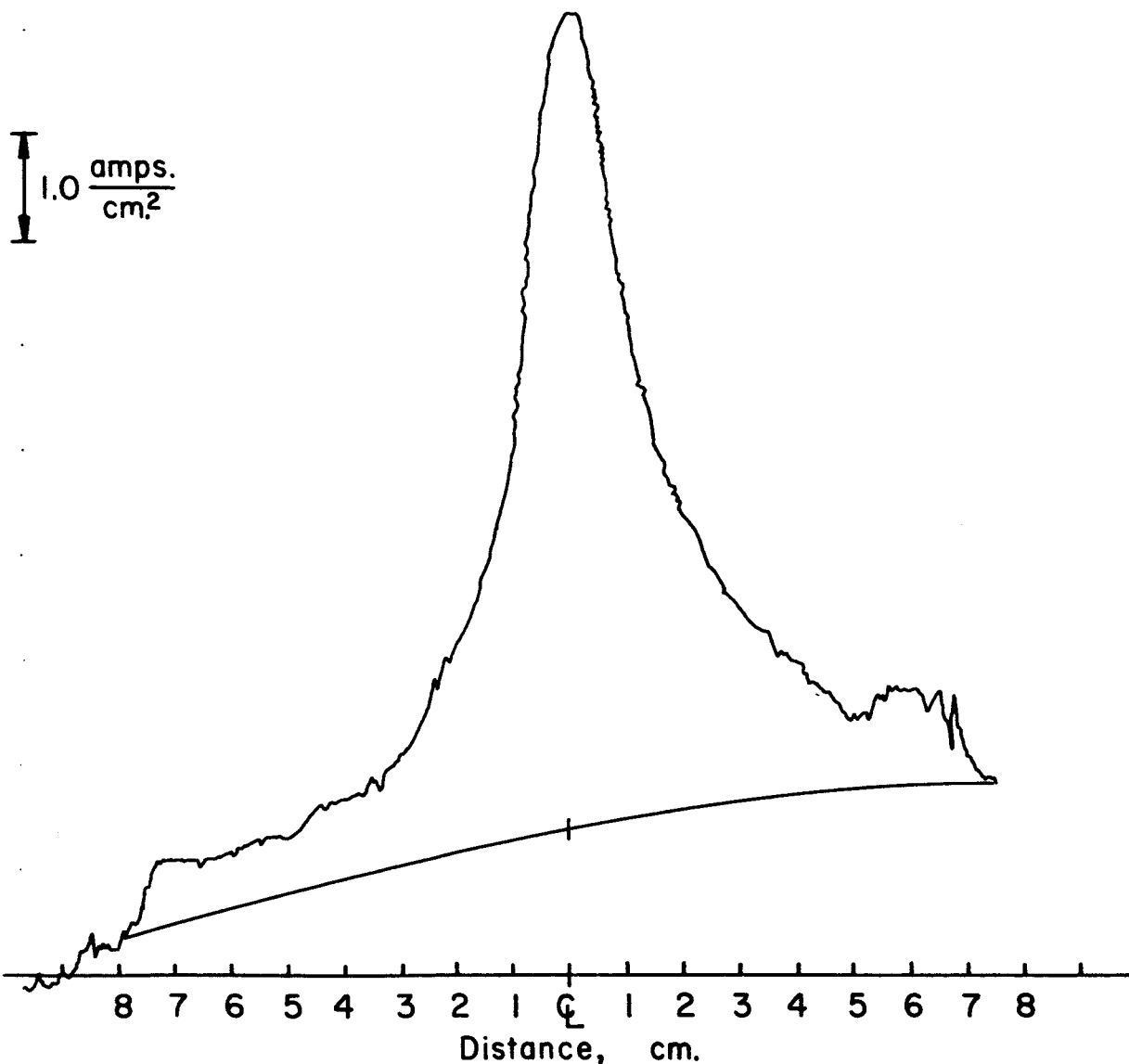


FIG. 7 Two-dimensional Analog of the accelerator voltage field for the Electron Emitter Wire half way between the Ionizer and the accelerator.



a.) No Electron Emission.



b.) 0.9 milliamps Electron Emission.

FIG. 8 Comparison of Ion beam kinetic energy profiles with and without Electron Emission.

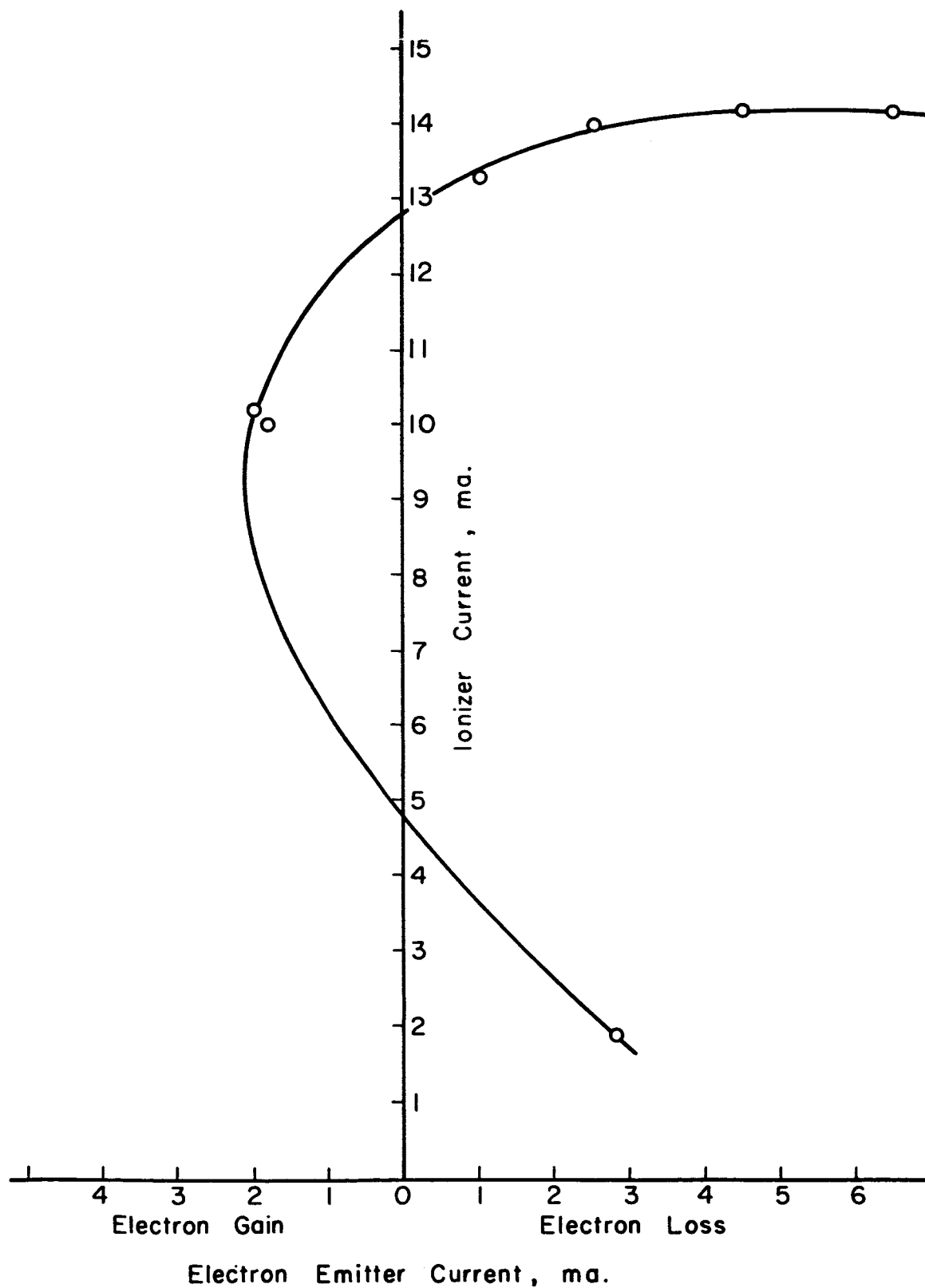


FIG. 9 Increase in ionizer current as a function of electron emitter current for the conditions shown in Fig. 7

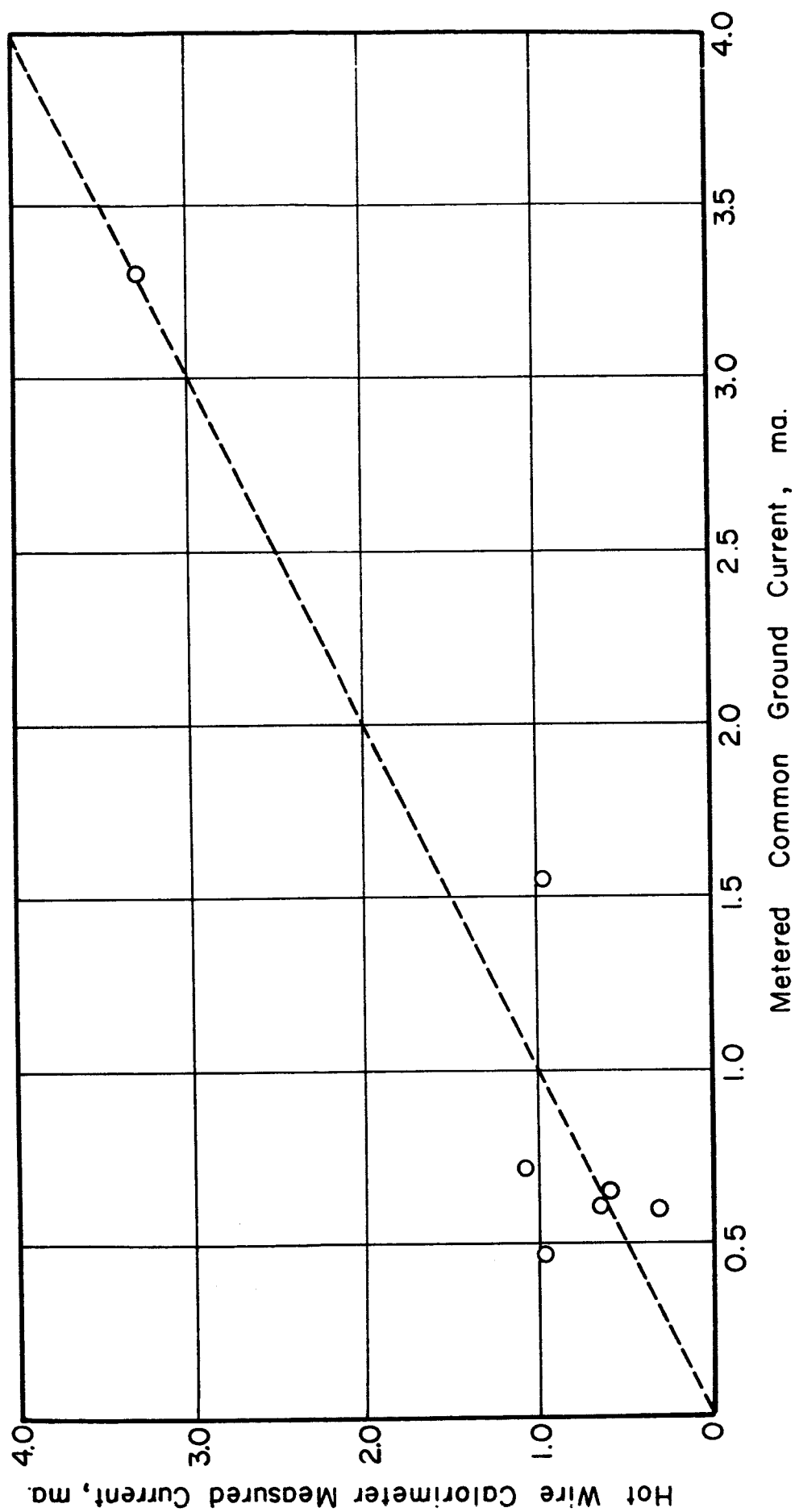


FIG. 10 Comparison of metered and hot wire calorimeter beam currents

APPENDIX B

EXPERIMENTAL DATA

Two sets of experimental data are given in the following figures. The first set is for the 1/2-inch EOS ion thruster, and the second set is for the electron emission, porous steel ion thruster.

A. EOS 1/2-Inch Ion Thruster - The EOS standard button ionizer, ion thruster was modified slightly for the present study. The porous tungsten ionizer is 1/2-inch in diameter. The focus electrode was made of 0.060-inch molybdenum sheet with a 45° tapered hole in the center. The negative accelerator was of 0.060-inch diameter copper with a 0.55-inch diameter hole. The hole of the copper accelerator was rounded to approximately 0.030 at the edge. An electron emitter wire of 0.010-inch diameter was placed at a distance of 0.25 inches from the porous tungsten. The electron emitter was approximately 0.55 inches in diameter. The negative accelerator was 0.50 inches from the porous tungsten.

Figure A-1 gives the results of varying the electron emitter voltage on the ion beam current. The data of fig. A-1 are for several different cesium flow rates. Figure A-2 shows the effect of varying the cesium flow rate with the other conditions held constant. Figure A-3 shows the effect of accelerator voltage on the ion beam current,

and fig. A-4 shows the effect of electron emission current on the ion beam current. In each figure, the variation of beam spreading width is shown. Symbols that appear on figures A-1 through A-4 are

E_+ = Ionizer voltage

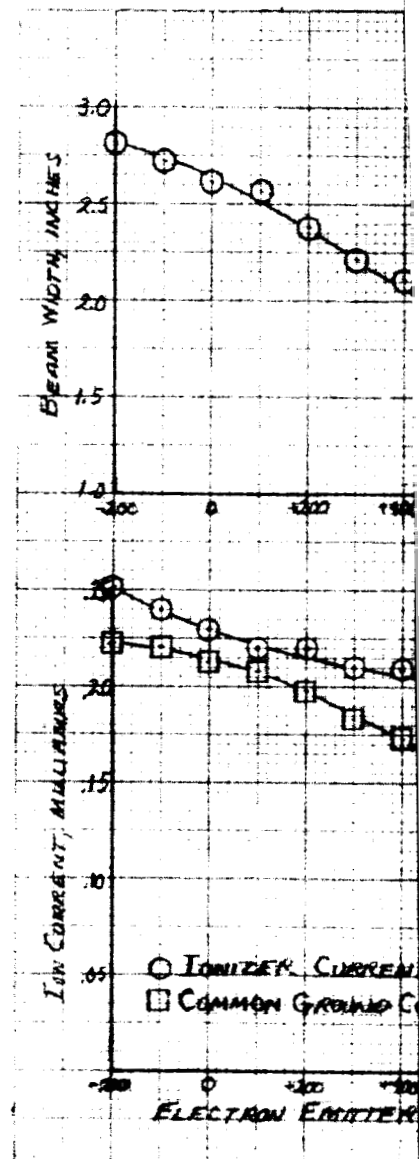
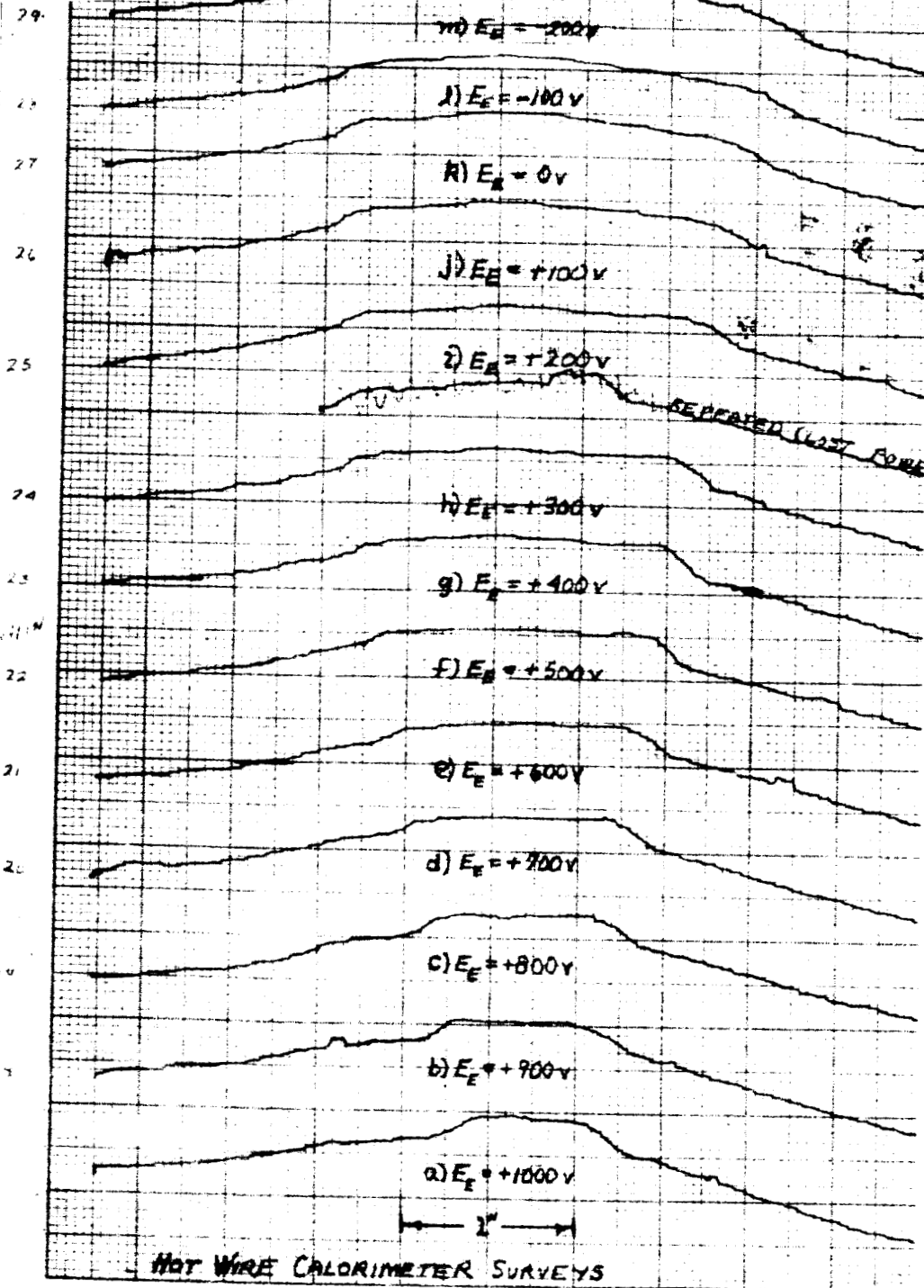
E_- = Negative accelerator voltage

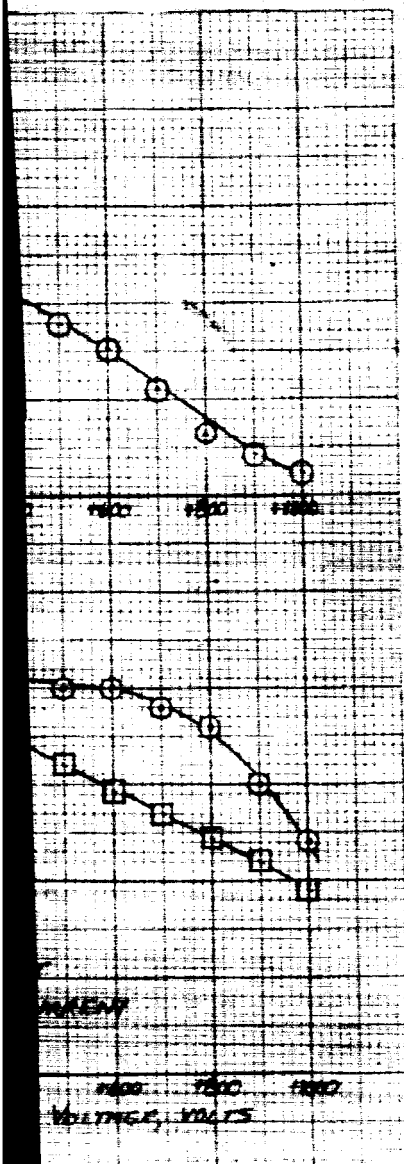
E_E = Electron emitter voltage

T_C = Cesium reservoir temperature

ΔV = $E_+ - E_-$

B. Electron Emission Ion Thrustor - Figure A-5 gives the actual measurements and hot-wire calorimeter profiles obtained with the porous steel thrustor shown in fig. 1. As may be seen from the data, maximum ion beam current can be obtained with an electron emission of roughly 1.5 milliamps. Further increase in electron emission failed to produce an increase in ion beam power.





PROFILE	IONIZER CURRENT	COMMON GROUND CURRENT	ELECTRON EMITTER CURRENT	IONIZER TEMP	CESIUM RESERVOIR TEMP
a	0.12 ma	0.096 ma	- *	1210 °C	109 °C
b	0.15	0.110	0.2 ma	1209	110
c	0.18	0.121	0.5	1209	111
d	0.19	0.136	3.0	1211	112
e	0.20	0.147	3.6	1210	113
f	0.20	0.160	6.5	1210	114
g	0.21	0.173	3.0	1210	115
h	0.21	0.183	9.1	1210	115
i	0.22	0.198	3.1	1211	116
j	0.22	0.208	3.2	1210	117
k	0.23	0.213	3.5	1210	118
l	0.24	0.221	2.6	1210	119
m	0.25	0.222	4.0	1209	119

IONIZER VOLTAGE = +1000 VOLTS

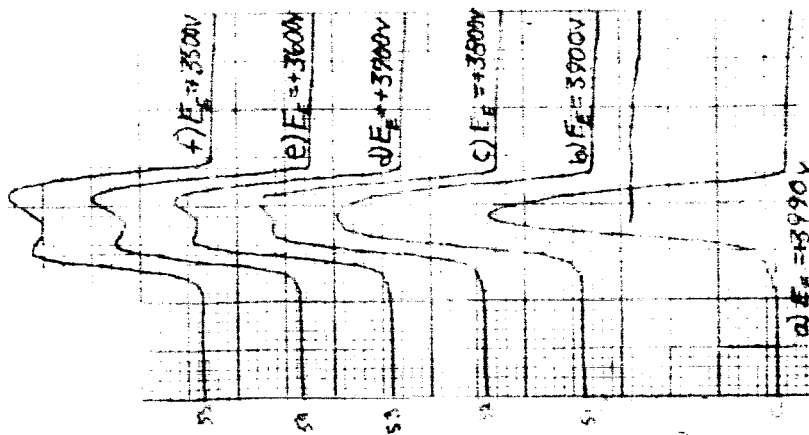
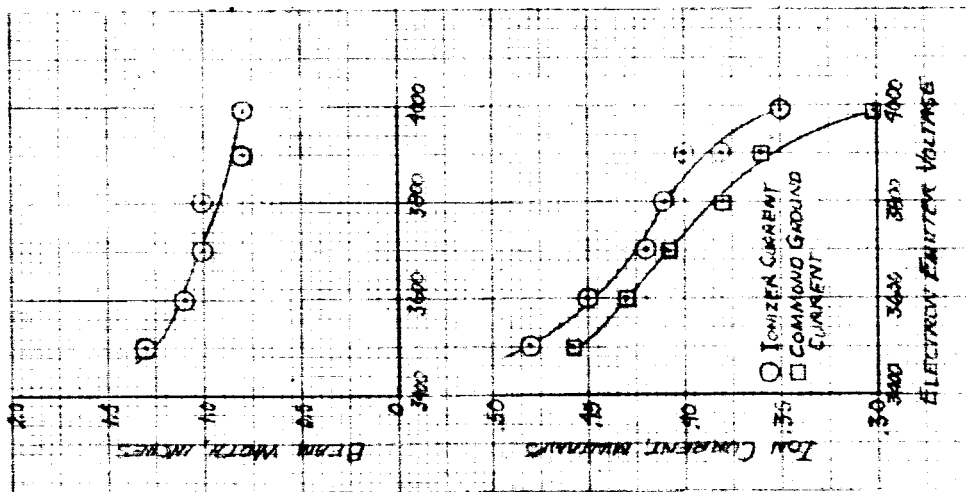
NEGATIVE ACCELERATION = -1000 VOLTS

*ELECTRON EMITTER WAS NOT OPERATED AS AN ELECTRON SOURCE DURING THESE TESTS.

(a)

FIGURE A-1 - EFFECT OF THE ELECTRON EMITTER VOLTAGE ON ION BEAM CURRENT.

of



PROG. #	IONIZER CURRENT	COMMAND GROUND CURRENT	ELECTRON Emitter CURRENT	INITIAL TEMP	DESIGN AIR TEMPERATURE
a	0.35 ma	0.30 ma	- *	1209 C	201 C
b	0.4	0.360	0	1210	202
c	0.41	0.380	0.3 ma	1210	210
d	0.42	0.408	0.1	1210	212
e	0.45	0.431	0.1	1210	214
f	0.48	0.453	0.1	1210	215

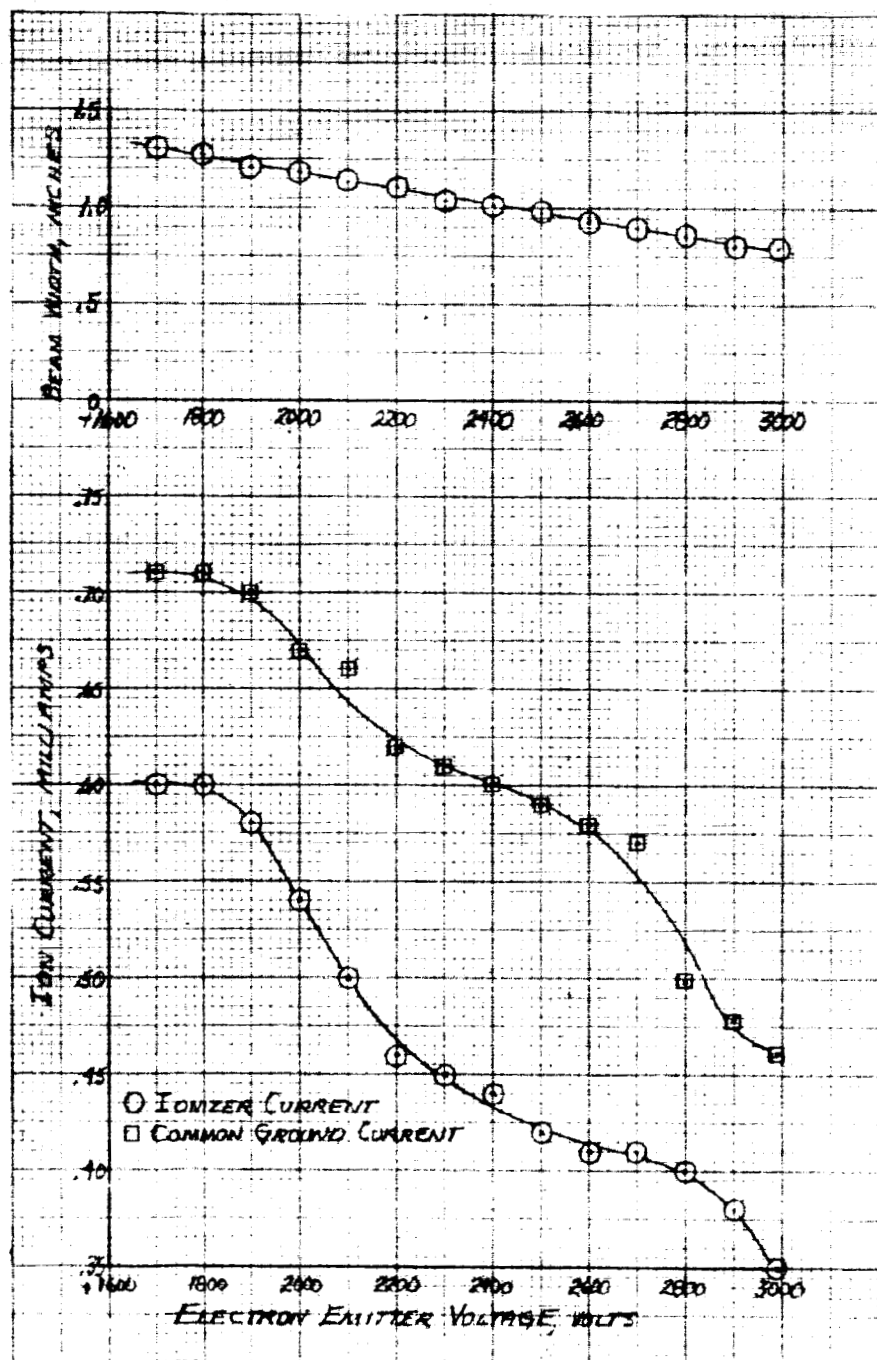
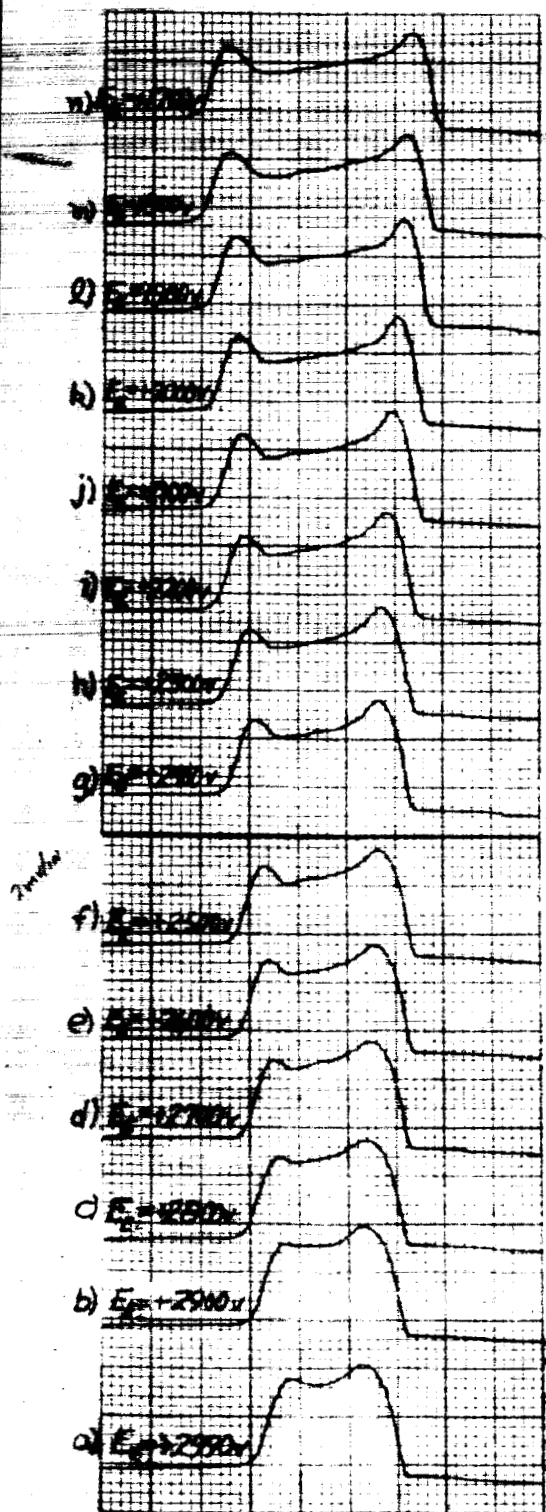
IONIZER VOLTAGE = +4000 VOLTS

HEAT SINK TEMPERATURE = +900 VOLTS

* ELECTRON Emitter WAS NOT OPERATED AS AN ELECTRON SOURCE DURING THESE TESTS

(b)

FIGURE 1: EFFECT OF ELECTRON Emitter VOLTAGE ON ION BEAM CURRENT



PROBE	IONIZER CURRENT	COMMON GROUND CURRENT	ELECTRON EMITTER CURRENT	IONIZER TEMP	CESIUM ACTIVATION TEMP
a	0.35 ma	0.46 ma	0 ma *	1210°C	220°C
b	0.38	0.476	0	"	221
c	0.40	0.495	0	"	223
d	0.41	0.570	0.1	"	224
e	0.41	0.550	0.1	"	225
f	0.42	0.590	0.2	"	226
g	0.44	0.600	0.5	"	227
h	0.45	0.610	0.6	"	227
i	0.46	0.620	0.6	"	228
j	0.50	0.660	0.7	"	229
k	0.54	0.670	1.1	"	229
l	0.58	0.700	2.2	"	230
m	0.60	0.710	2.3	"	230
n	0.60	0.710	2.6	"	231

IONIZER VOLTAGE = +3000 VOLTS

NEGATIVE ACCELERATION = -4000 VOLTS

* ELECTRON EMITTER WAS NOT OPERATED AS AN ELECTRON SOURCE DURING THESE TESTS.

(C)

FIGURE A-1 - EFFECT OF THE ELECTRON EMITTER VOLTAGE ON ION BEAM CURRENT.

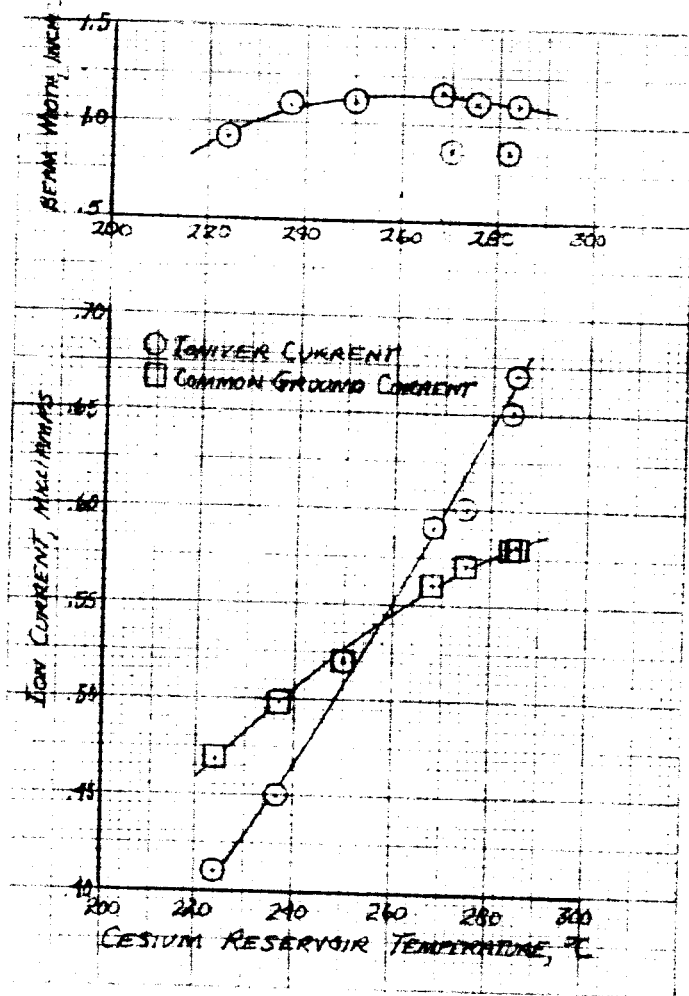
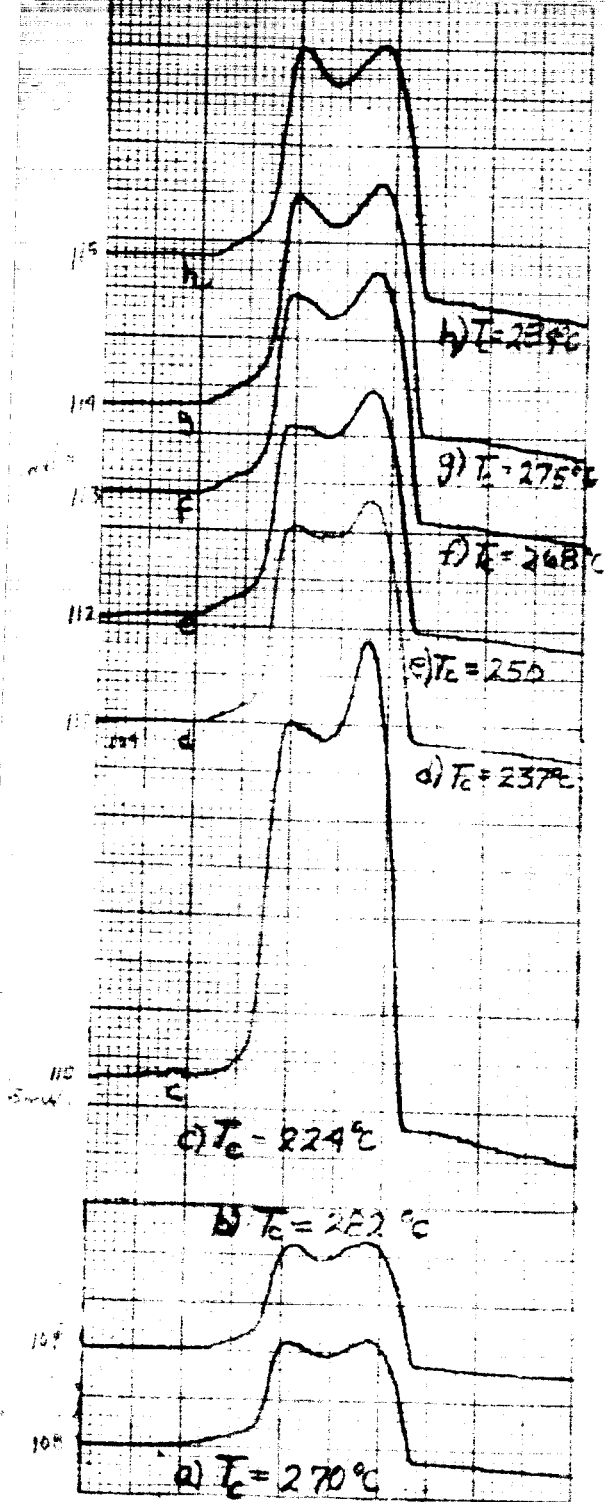
28

Source	Ion Beam Current (mA)	Electron Beam Current (mA)	Ion Beam Voltage (kV)	Electron Beam Voltage (kV)
a	1.1574	.5072	0	12.5
b	1.0	.600	0	12.5
c	.41	.468	0	12.5
d	.45	.45	0	12.5
e	.52	.500	0	12.5
f	.59	.500	0	12.5
g	.60	.500	0	12.5
h	.65	.500	0	12.5

ION BEAM CURRENT = 1.000 mA
 ELECTRON BEAM CURRENT = 1.000 mA
 ELECTRON BEAM VOLTAGE = 12.5 kV

FIGURE A-2 - EFFECT OF ION BEAM RATE
 ON ION BEAM CURRENT

2



PROFILE	IONIZER VOLTAGE	NEGATIVE ACCELERATION VOLTAGE	IONIZER CURRENT	COMMON GROUND CURRENT	IONIZER TEMP	REFILL RESERVOIR TEMP
a	+1000V	-1000V	0.10 ma	0.086 ma	1203°C	172°C
b	+1000V	-2000V	0.18	0.135	1203	178
c	+1000V	-3000V	0.20	0.178	1202	180
d	+1000V	-4000V	0.21	0.199	1202	188
e	+2000V	-4000V	0.22	0.212	1201	192
f	+3000V	-4000V	0.23	0.292	1210	196
g	+4000V	-4000V	0.23	0.262	1210	200

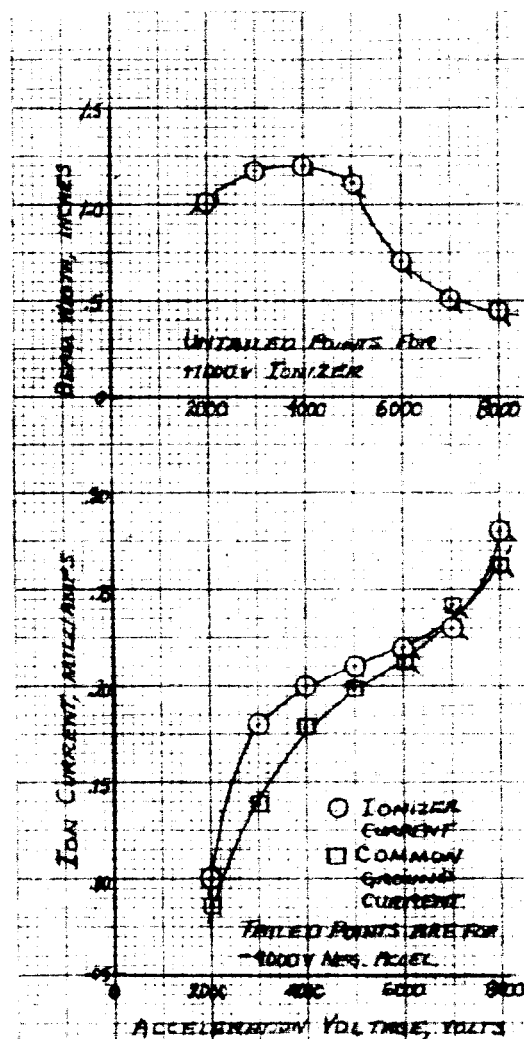
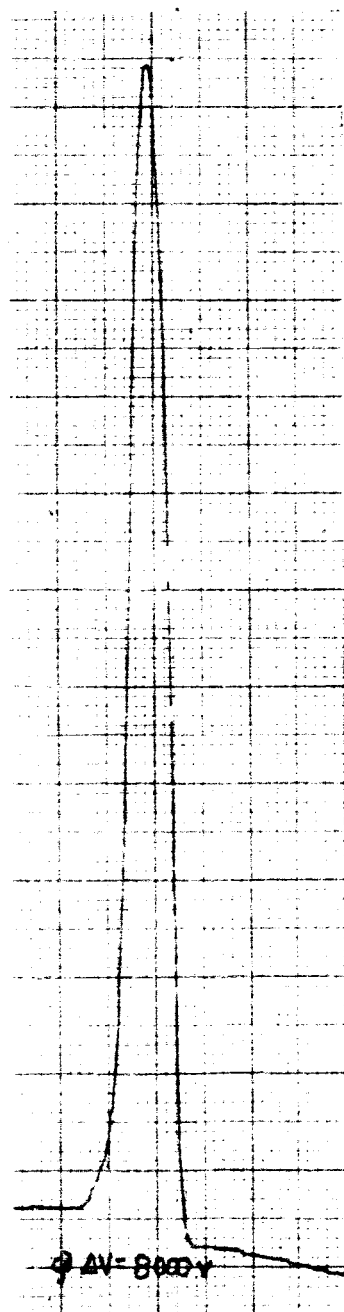
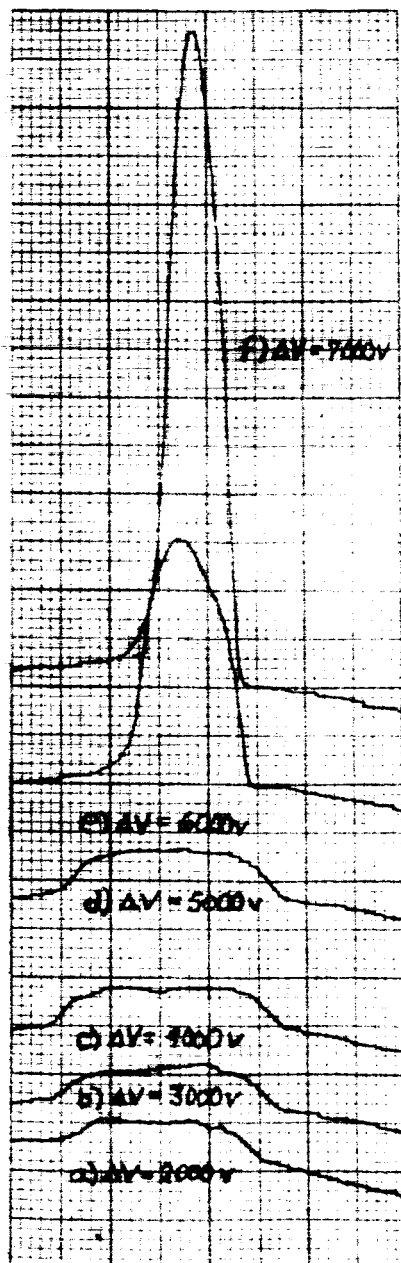
ELECTRON EMITTER AT +990 VOLTS

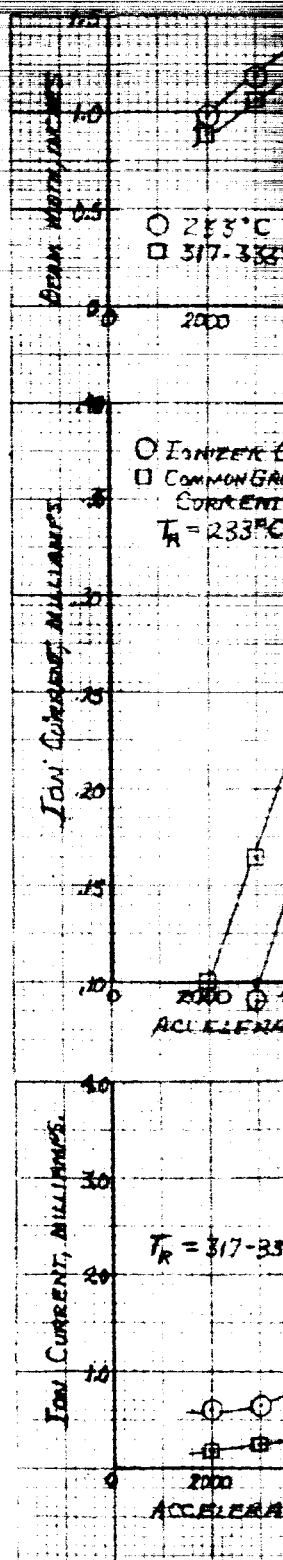
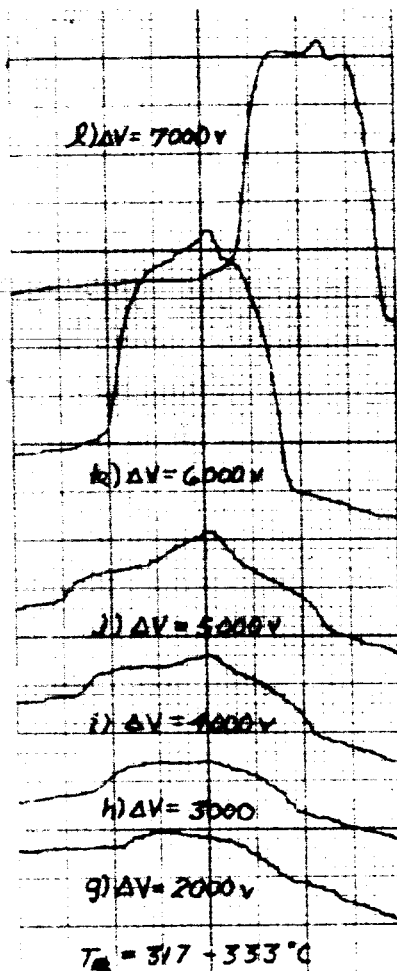
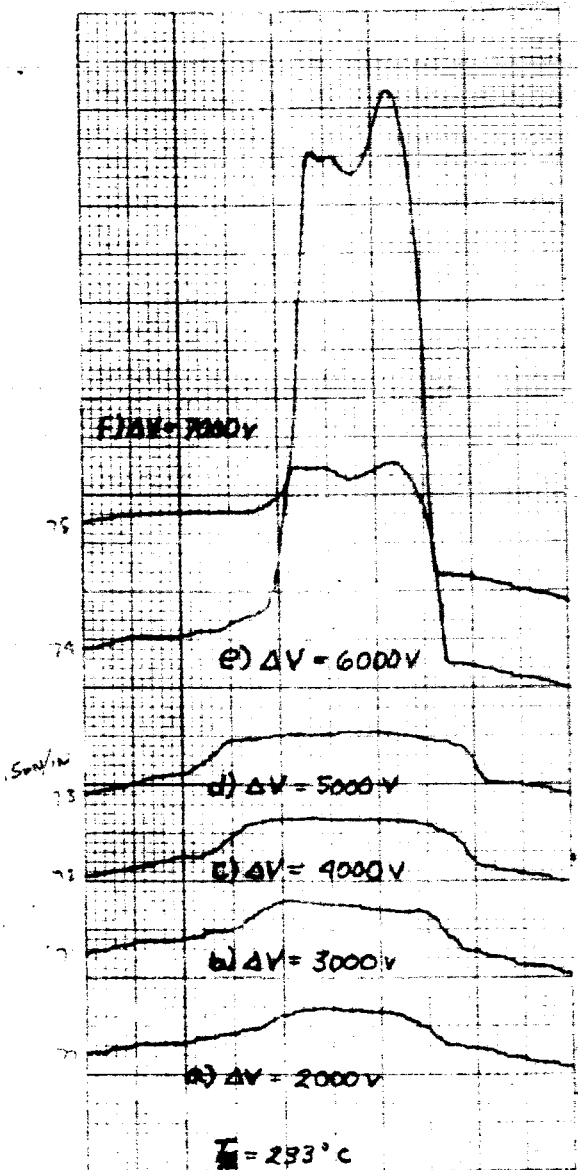
NO OBSERVED CURRENT ON THE ELECTRON EMITTER

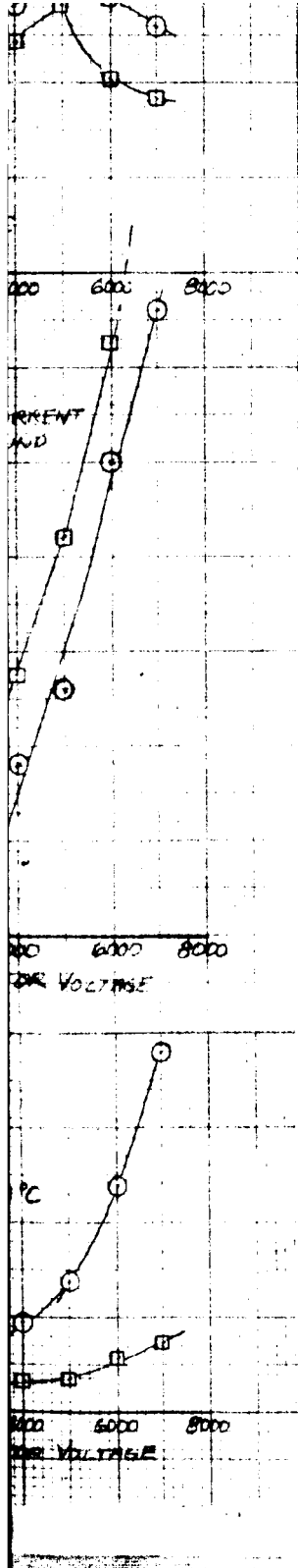
(2)

FIGURE A-3-EFFECT OF ACCELERATION VOLTAGE
ON ION BEAM CURRENT

2







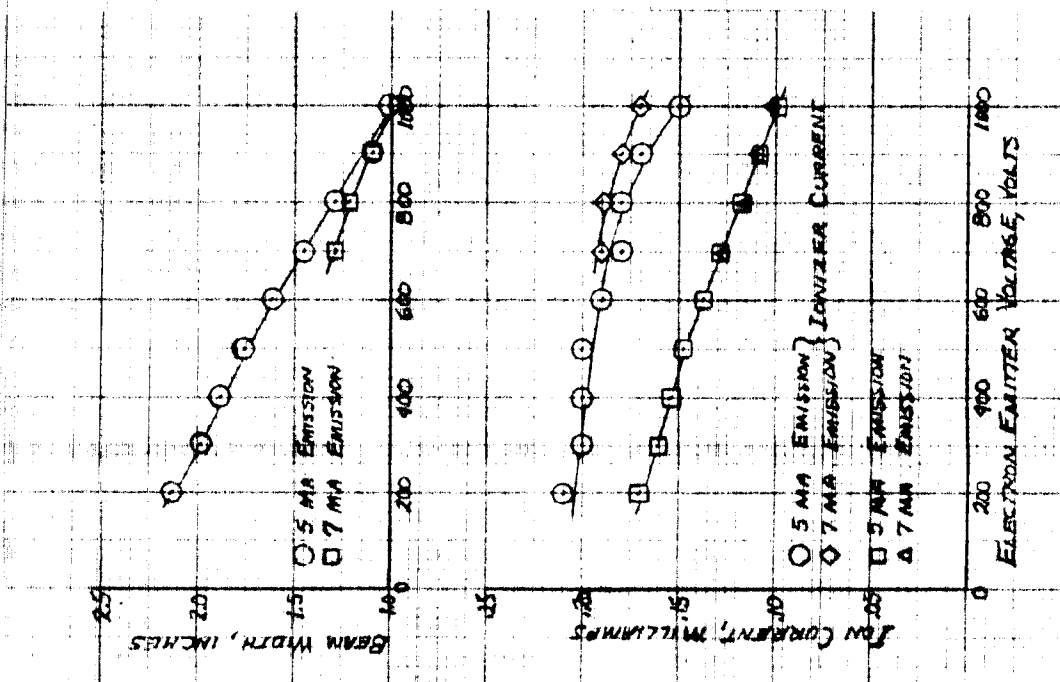
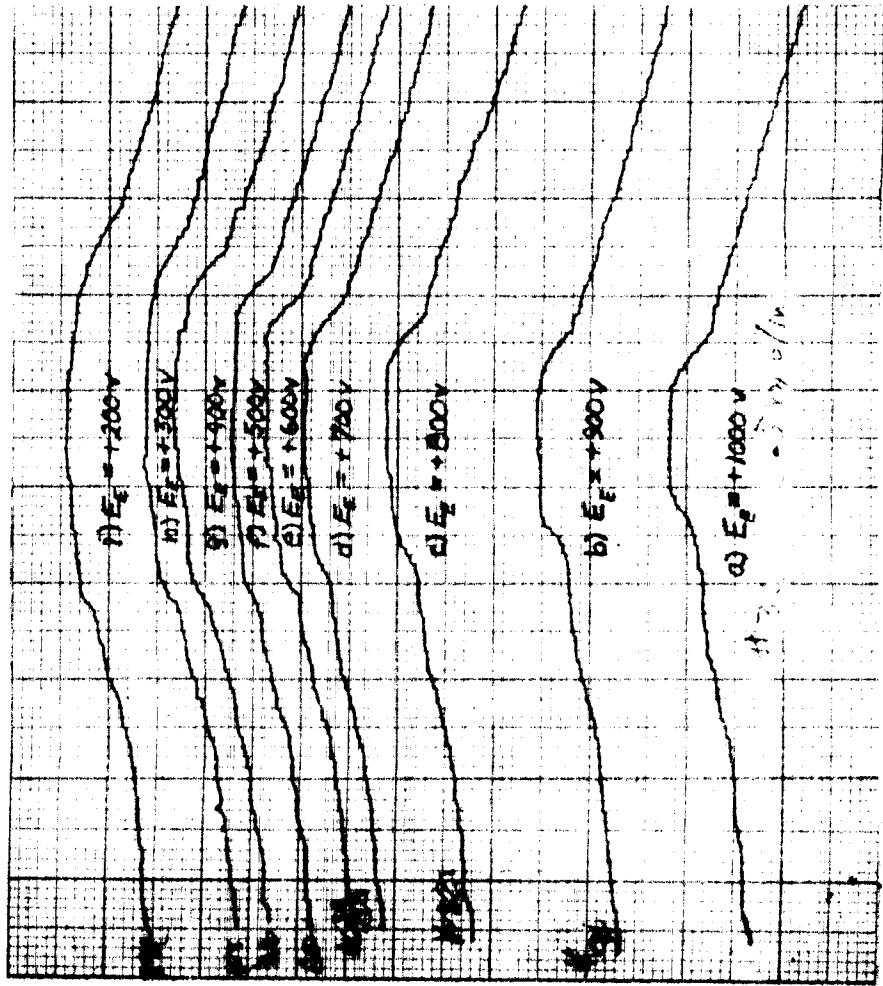
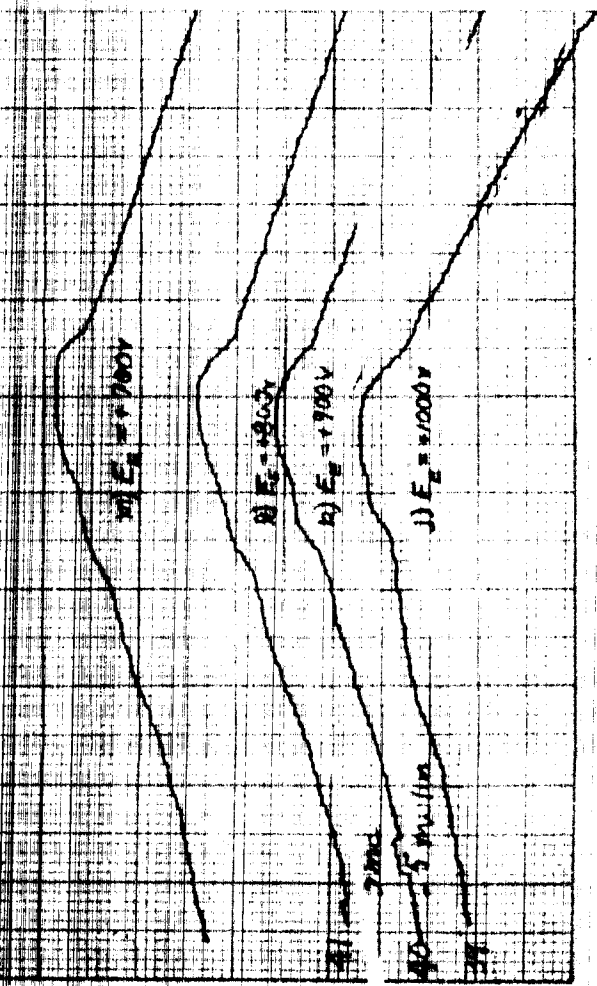
PROFILE	IONIZER VOLTAGE	NEGATIVE ACCELERATOR VOLTAGE	IONIZER CURRENT	COMMON GROUND CURRENT	IONIZER TEMP	CESIUM RESERVOIR TEMP
a	+1000V	-1000V	-	0.100 ma	1211°C	232°C
b	+1000V	-2000V	0.09 ma	0.165	"	232
c	+1000V	-3000V	0.19	0.238	"	233
d	+1000V	-4000V	0.23	0.310	"	233
e	+2000V	-4000V	0.35	0.413	"	233
f	+3000V	-4000V	0.43	0.570	"	234

INCREASED CESIUM FLOW RATE							IMPALEMENT CURRENT
g	+1000V	-1000V	0.60 ma	0.190 ma	1232°C	317°C	0.40 ma
h	+1000V	-2000V	0.65	0.258	1230	323	0.42
i	+1000V	-3000V	0.95	0.315	1228	326	0.60
j	+1000V	-4000V	1.38	0.352	1230	328	1.10
k	+2000V	-4000V	2.38	0.580	1233	333	2.00
l	+3000V	-4000V	3.80	0.730	1248	333	3.40

ELECTRON EMITTER VOLTAGE WITHIN 10 VOLTS OF THE IONIZER VOLTAGE.

(b)

FIGURE A-3-EFFECT OF THE ACCELERATOR VOLTAGE ON ION BEAM CURRENT



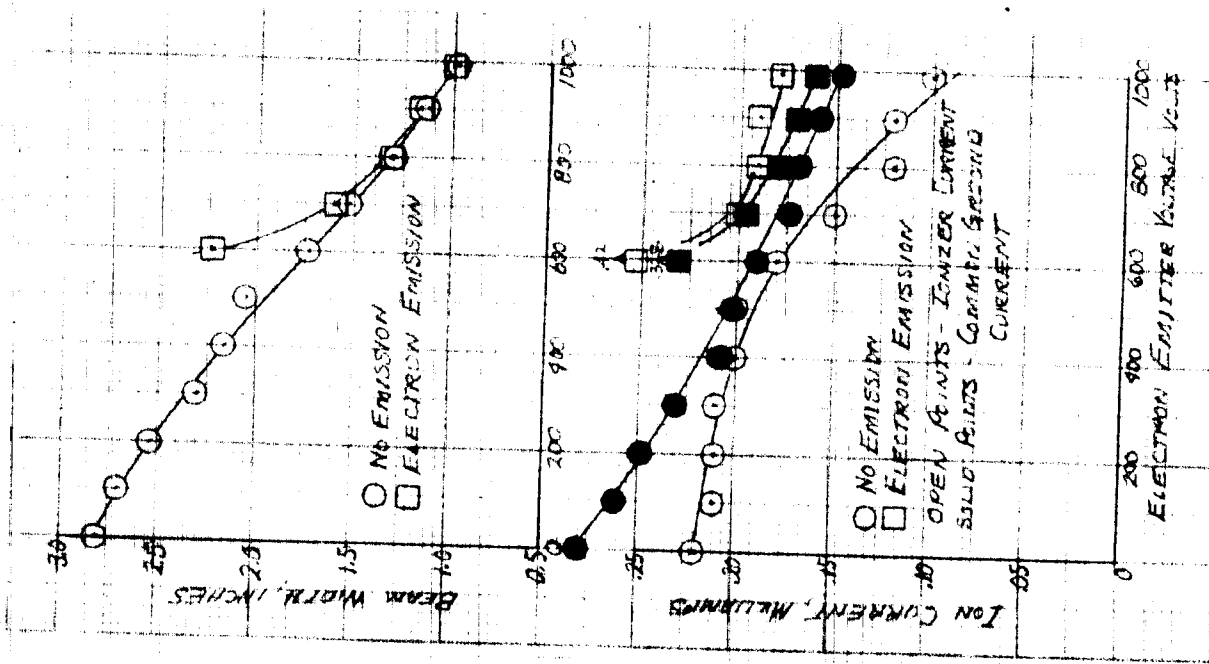
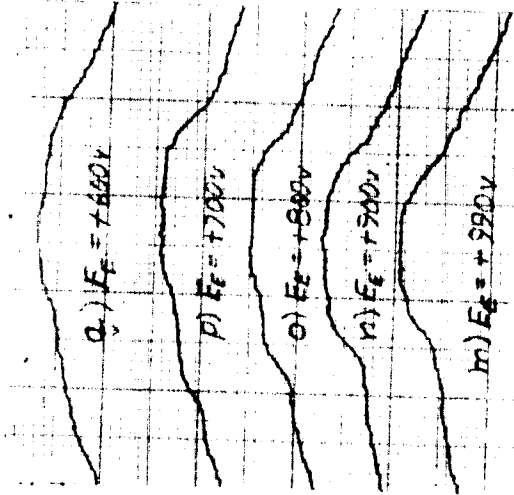
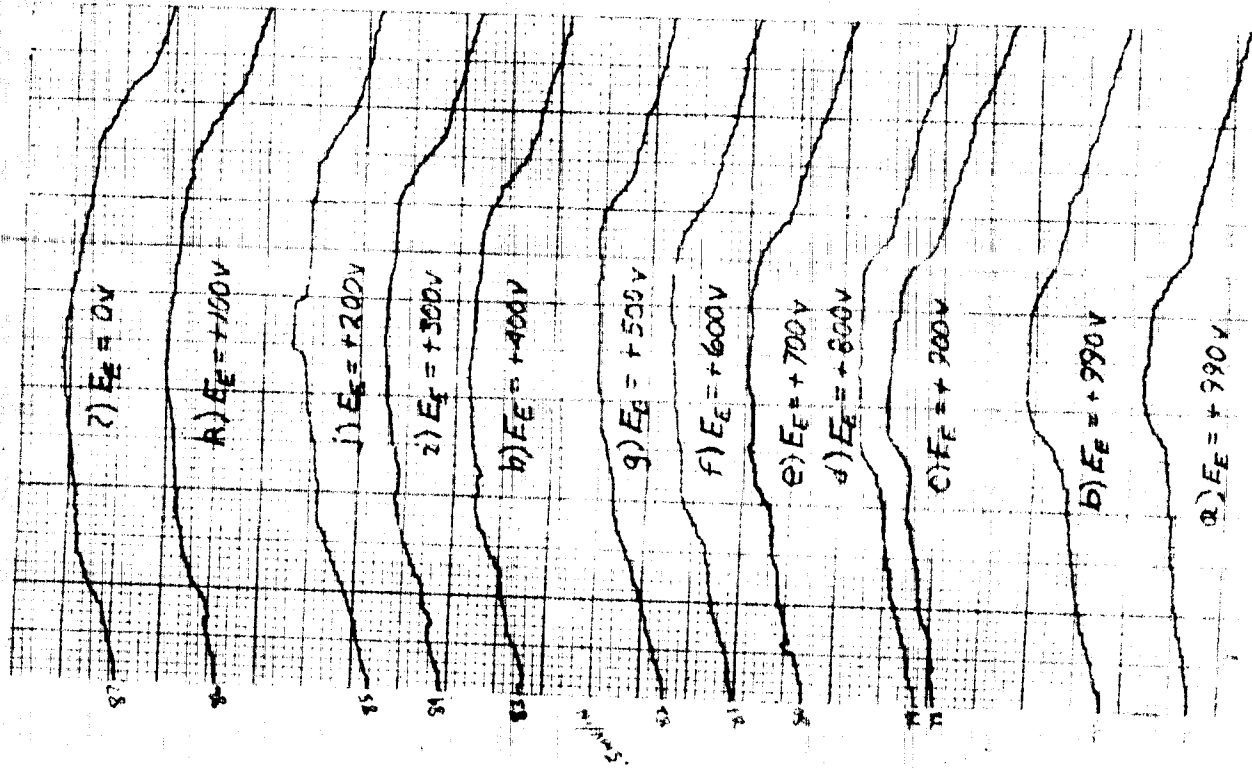
PROFILE	IONIZER CURRENT	COMMON GROUND CURRENT	ELECTRON EMISSION	IONIZER TEMP.	CESIUM RESERVOIR TEMP.
a	0.15 mA	0.09 mA	-	121.5°C	121°C
b	0.17	0.109	0 mA	121.7°C	121
c	0.18	0.109	0.1	121.8	123
d	0.18	0.125	0.5	121.1	122
e	0.19	0.137	0.7	121.1	123
f	0.20	0.148	1.5	121.1	123
g	0.20	0.153	2.3	121.1	124
h	0.20	0.161	3.3	121.1	124
i	0.21	0.170	19.0	123.0	125
j	0.17	0.101	-	123.0	126
k	0.18	0.109	0.5	121.2	127
l	0.19	0.114	2.0	122.0	127
m	0.19	0.127	9.2	122.0	128

IONIZER VOLTAGE = +1000 VOLTS
NEGATIVE ACCELERATOR = -1000 VOLTS

(a)

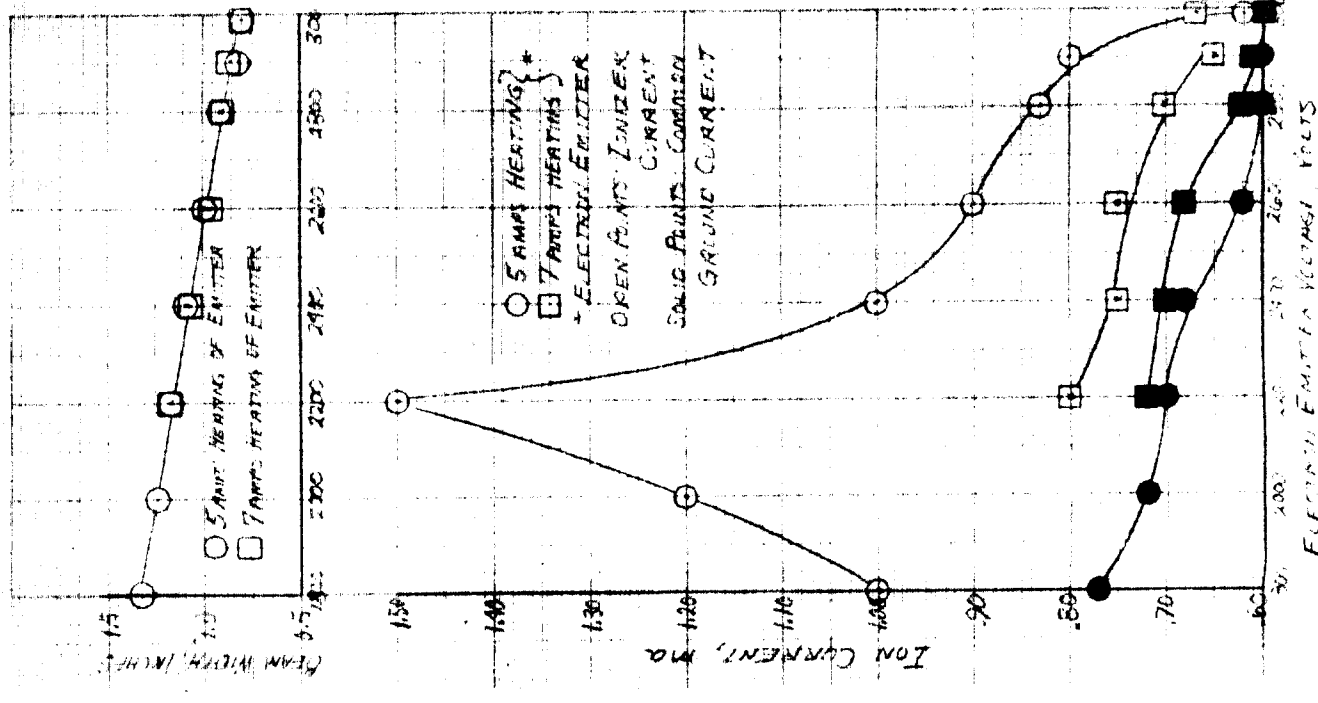
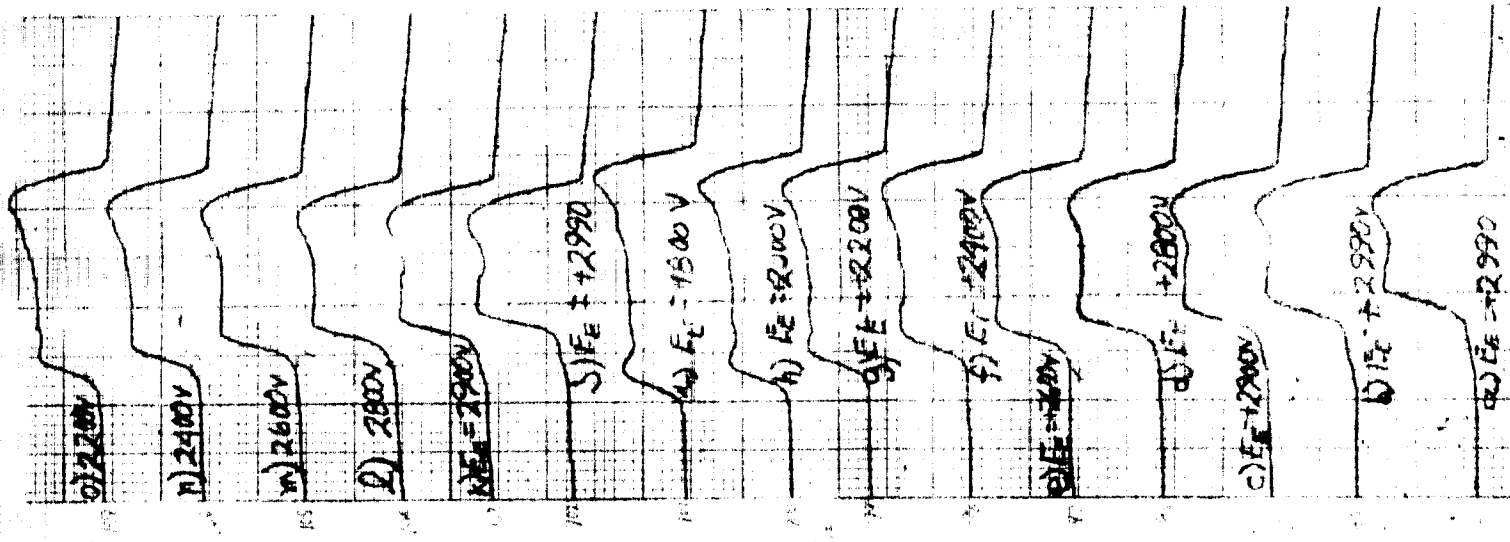
FIGURE A-4.- EFFECT OF ELECTRON EMISSION ON THE ACCELERATION OF IONS.

2



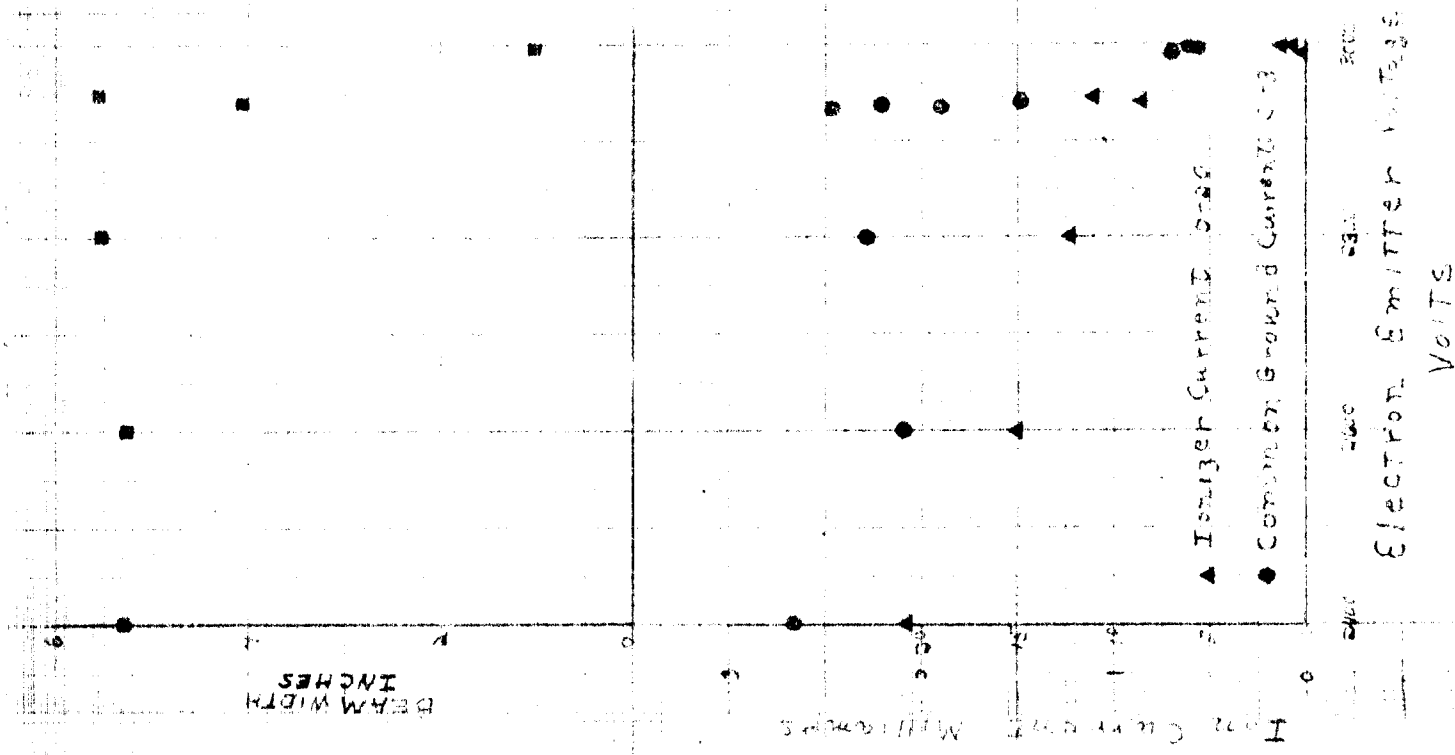
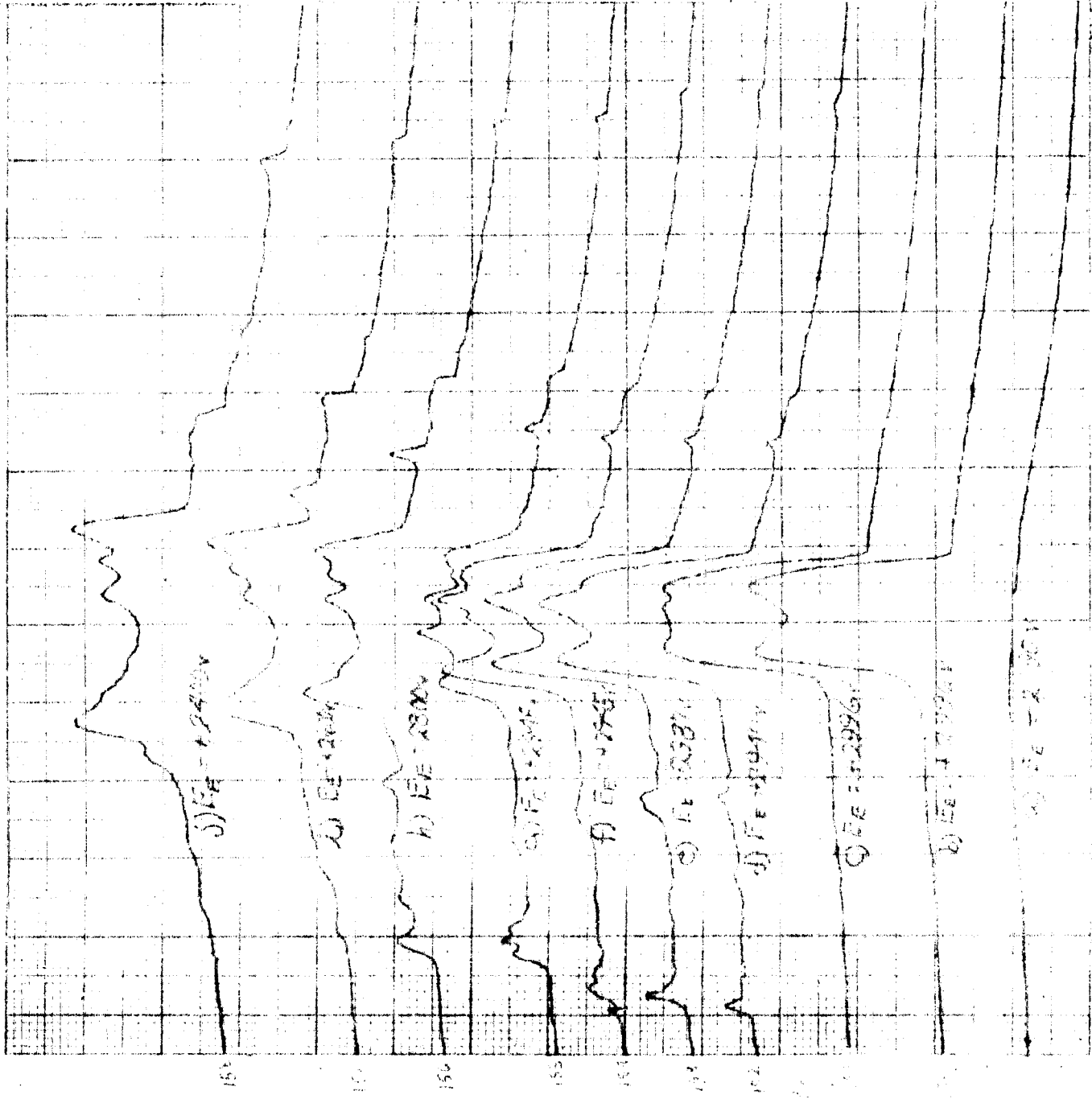
Emitter Voltage, Volts	Ion Current, mA	Electron Emitter Current, mA	Beam Width, Inches
0	0.00	0.00	0.00
100	0.00	0.00	0.00
200	0.00	0.00	0.00
300	0.00	0.00	0.00
400	0.00	0.00	0.00
500	0.00	0.00	0.00
600	0.00	0.00	0.00
700	0.00	0.00	0.00
800	0.00	0.00	0.00
900	0.00	0.00	0.00
1000	0.00	0.00	0.00

FIGURE 1. EFFECT OF IONIZER VOLTAGE ON ELECTRON EMISSION AND BEAM WIDTH.



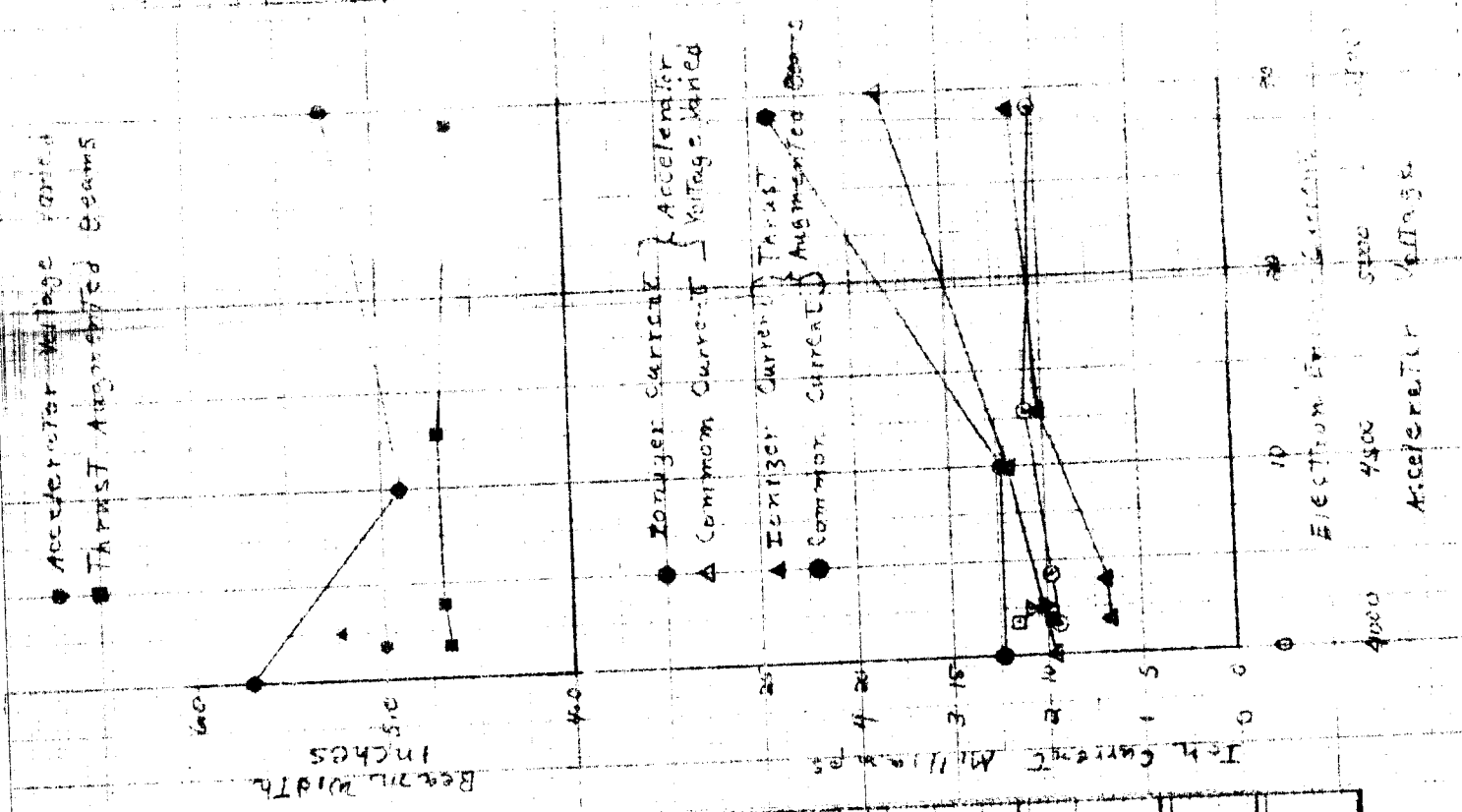
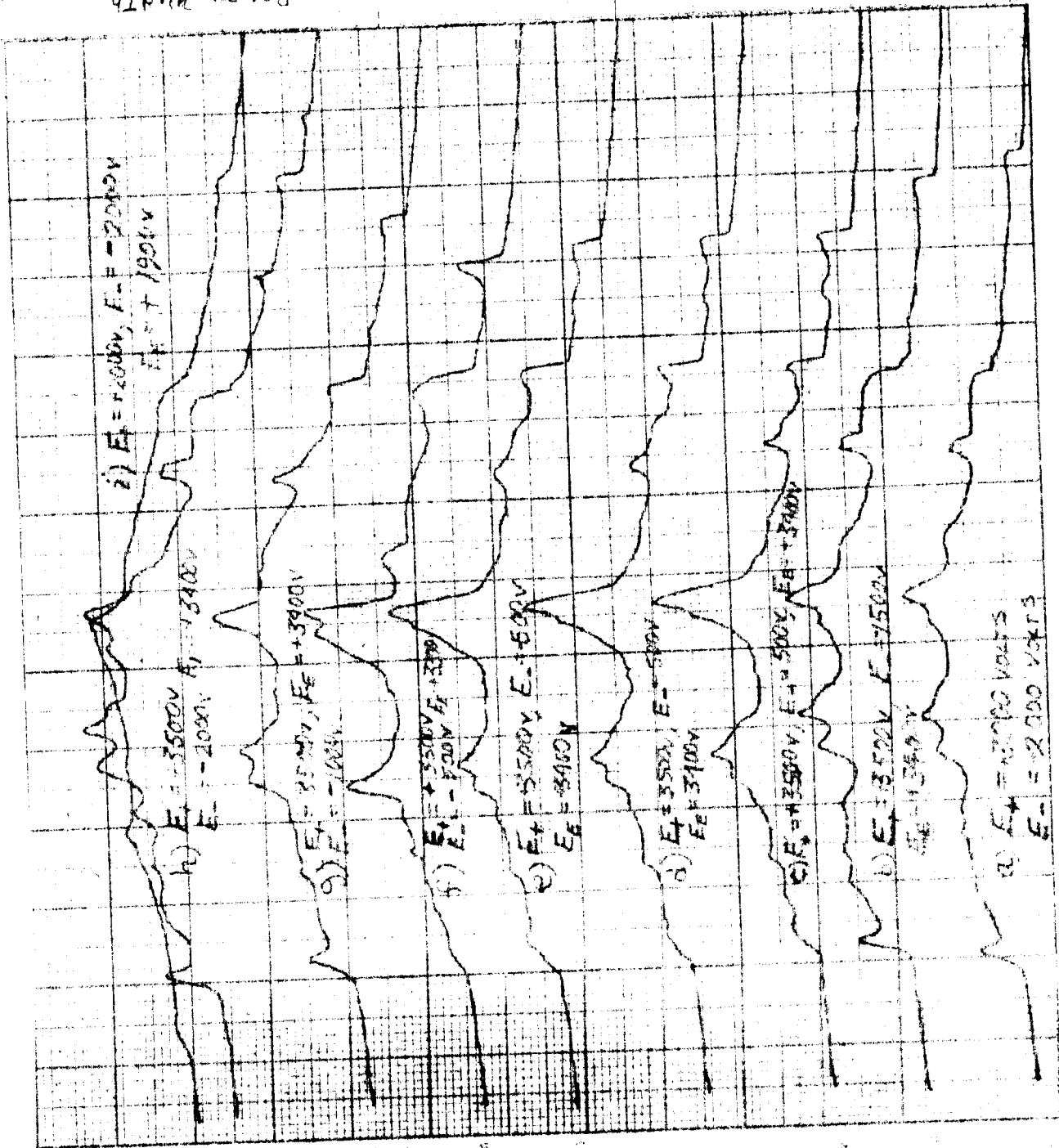
Emitter Voltage, V	Ionizer Current, mA	Electron Emitter Current, mA	Ionizer Current, mA	Electron Emitter Current, mA
0	0.45	0.57	0.45	0.57
0.2	0.62	0.60	0.62	0.60
0.4	0.80	0.60	0.80	0.60
0.6	0.90	0.60	0.90	0.60
0.8	1.00	0.60	1.00	0.60
1.0	1.10	0.60	1.10	0.60
1.2	1.20	0.60	1.20	0.60
1.4	1.30	0.60	1.30	0.60
1.6	1.40	0.60	1.40	0.60
1.8	1.50	0.60	1.50	0.60
2.0	1.60	0.60	1.60	0.60
2.2	1.70	0.60	1.70	0.60
2.4	1.80	0.60	1.80	0.60
2.6	1.90	0.60	1.90	0.60
2.8	2.00	0.60	2.00	0.60
3.0	2.10	0.60	2.10	0.60
3.2	2.20	0.60	2.20	0.60
3.4	2.30	0.60	2.30	0.60
3.6	2.40	0.60	2.40	0.60
3.8	2.50	0.60	2.50	0.60
4.0	2.60	0.60	2.60	0.60
4.2	2.70	0.60	2.70	0.60
4.4	2.80	0.60	2.80	0.60
4.6	2.90	0.60	2.90	0.60
4.8	3.00	0.60	3.00	0.60
5.0	3.10	0.60	3.10	0.60
5.2	3.20	0.60	3.20	0.60
5.4	3.30	0.60	3.30	0.60
5.6	3.40	0.60	3.40	0.60
5.8	3.50	0.60	3.50	0.60
6.0	3.60	0.60	3.60	0.60
6.2	3.70	0.60	3.70	0.60
6.4	3.80	0.60	3.80	0.60
6.6	3.90	0.60	3.90	0.60
6.8	4.00	0.60	4.00	0.60
7.0	4.10	0.60	4.10	0.60
7.2	4.20	0.60	4.20	0.60
7.4	4.30	0.60	4.30	0.60
7.6	4.40	0.60	4.40	0.60
7.8	4.50	0.60	4.50	0.60
8.0	4.60	0.60	4.60	0.60
8.2	4.70	0.60	4.70	0.60
8.4	4.80	0.60	4.80	0.60
8.6	4.90	0.60	4.90	0.60
8.8	5.00	0.60	5.00	0.60
9.0	5.10	0.60	5.10	0.60
9.2	5.20	0.60	5.20	0.60
9.4	5.30	0.60	5.30	0.60
9.6	5.40	0.60	5.40	0.60
9.8	5.50	0.60	5.50	0.60
10.0	5.60	0.60	5.60	0.60

FIGURE A-4 - EFFECT OF EMITTER HEATING ON THE ACCELERATION OF IONS



Beam Width (inches)	Ion Current (mA)	Collector Ground Current (mA)
0.0	0.0	0.0
0.1	0.0	0.0
0.2	0.0	0.0
0.3	0.0	0.0
0.4	0.0	0.0
0.5	0.0	0.0
0.6	0.0	0.0
0.7	0.0	0.0
0.8	0.0	0.0
0.9	0.0	0.0
1.0	0.0	0.0
1.1	0.0	0.0
1.2	0.0	0.0
1.3	0.0	0.0
1.4	0.0	0.0
1.5	0.0	0.0
1.6	0.0	0.0
1.7	0.0	0.0
1.8	0.0	0.0
1.9	0.0	0.0
2.0	0.0	0.0
2.1	0.0	0.0
2.2	0.0	0.0
2.3	0.0	0.0
2.4	0.0	0.0
2.5	0.0	0.0
2.6	0.0	0.0
2.7	0.0	0.0
2.8	0.0	0.0
2.9	0.0	0.0
3.0	0.0	0.0
3.1	0.0	0.0
3.2	0.0	0.0
3.3	0.0	0.0
3.4	0.0	0.0
3.5	0.0	0.0
3.6	0.0	0.0
3.7	0.0	0.0
3.8	0.0	0.0
3.9	0.0	0.0
4.0	0.0	0.0
4.1	0.0	0.0
4.2	0.0	0.0
4.3	0.0	0.0
4.4	0.0	0.0
4.5	0.0	0.0
4.6	0.0	0.0
4.7	0.0	0.0
4.8	0.0	0.0
4.9	0.0	0.0
5.0	0.0	0.0
5.1	0.0	0.0
5.2	0.0	0.0
5.3	0.0	0.0
5.4	0.0	0.0
5.5	0.0	0.0
5.6	0.0	0.0
5.7	0.0	0.0
5.8	0.0	0.0
5.9	0.0	0.0
6.0	0.0	0.0
6.1	0.0	0.0
6.2	0.0	0.0
6.3	0.0	0.0
6.4	0.0	0.0
6.5	0.0	0.0
6.6	0.0	0.0
6.7	0.0	0.0
6.8	0.0	0.0
6.9	0.0	0.0
7.0	0.0	0.0
7.1	0.0	0.0
7.2	0.0	0.0
7.3	0.0	0.0
7.4	0.0	0.0
7.5	0.0	0.0
7.6	0.0	0.0
7.7	0.0	0.0
7.8	0.0	0.0
7.9	0.0	0.0
8.0	0.0	0.0
8.1	0.0	0.0
8.2	0.0	0.0
8.3	0.0	0.0
8.4	0.0	0.0
8.5	0.0	0.0
8.6	0.0	0.0
8.7	0.0	0.0
8.8	0.0	0.0
8.9	0.0	0.0
9.0	0.0	0.0
9.1	0.0	0.0
9.2	0.0	0.0
9.3	0.0	0.0
9.4	0.0	0.0
9.5	0.0	0.0
9.6	0.0	0.0
9.7	0.0	0.0
9.8	0.0	0.0
9.9	0.0	0.0
10.0	0.0	0.0

Beam Width (inches)	Ion Current (mA)	Collector Ground Current (mA)
0.0	0.0	0.0
0.1	0.0	0.0
0.2	0.0	0.0
0.3	0.0	0.0
0.4	0.0	0.0
0.5	0.0	0.0
0.6	0.0	0.0
0.7	0.0	0.0
0.8	0.0	0.0
0.9	0.0	0.0
1.0	0.0	0.0
1.1	0.0	0.0
1.2	0.0	0.0
1.3	0.0	0.0
1.4	0.0	0.0
1.5	0.0	0.0
1.6	0.0	0.0
1.7	0.0	0.0
1.8	0.0	0.0
1.9	0.0	0.0
2.0	0.0	0.0
2.1	0.0	0.0
2.2	0.0	0.0
2.3	0.0	0.0
2.4	0.0	0.0
2.5	0.0	0.0
2.6	0.0	0.0
2.7	0.0	0.0
2.8	0.0	0.0
2.9	0.0	0.0
3.0	0.0	0.0
3.1	0.0	0.0
3.2	0.0	0.0
3.3	0.0	0.0
3.4	0.0	0.0
3.5	0.0	0.0
3.6	0.0	0.0
3.7	0.0	0.0
3.8	0.0	0.0
3.9	0.0	0.0
4.0	0.0	0.0
4.1	0.0	0.0
4.2	0.0	0.0
4.3	0.0	0.0
4.4	0.0	0.0
4.5	0.0	0.0
4.6	0.0	0.0
4.7	0.0	0.0
4.8	0.0	0.0
4.9	0.0	0.0
5.0	0.0	0.0
5.1	0.0	0.0
5.2	0.0	0.0
5.3	0.0	0.0
5.4	0.0	0.0
5.5	0.0	0.0
5.6	0.0	0.0
5.7	0.0	0.0
5.8	0.0	0.0
5.9	0.0	0.0
6.0	0.0	0.0
6.1	0.0	0.0
6.2	0.0	0.0
6.3	0.0	0.0
6.4	0.0	0.0
6.5	0.0	0.0
6.6	0.0	0.0
6.7	0.0	0.0
6.8	0.0	0.0
6.9	0.0	0.0
7.0	0.0	0.0
7.1	0.0	0.0
7.2	0.0	0.0
7.3	0.0	0.0
7.4	0.0	0.0
7.5	0.0	0.0
7.6	0.0	0.0
7.7	0.0	0.0
7.8	0.0	0.0
7.9	0.0	0.0
8.0	0.0	0.0
8.1	0.0	0.0
8.2	0.0	0.0
8.3	0.0	0.0
8.4	0.0	0.0
8.5	0.0	0.0
8.6	0.0	0.0
8.7	0.0	0.0
8.8	0.0	0.0
8.9	0.0	0.0
9.0	0.0	0.0
9.1	0.0	0.0
9.2	0.0	0.0
9.3	0.0	0.0
9.4	0.0	0.0
9.5	0.0	0.0
9.6	0.0	0.0
9.7	0.0	0.0
9.8	0.0	0.0
9.9	0.0	0.0
10.0	0.0	0.0

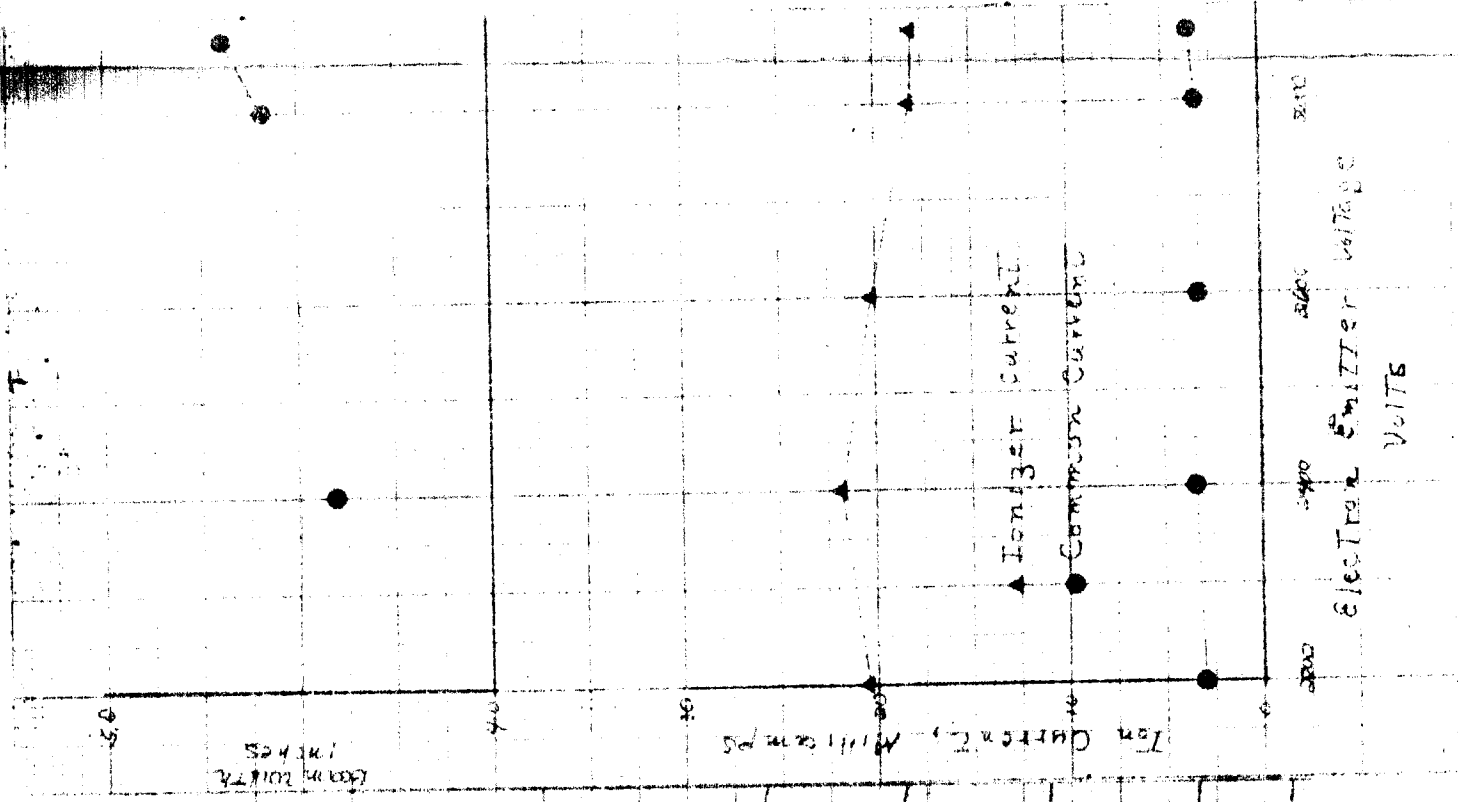
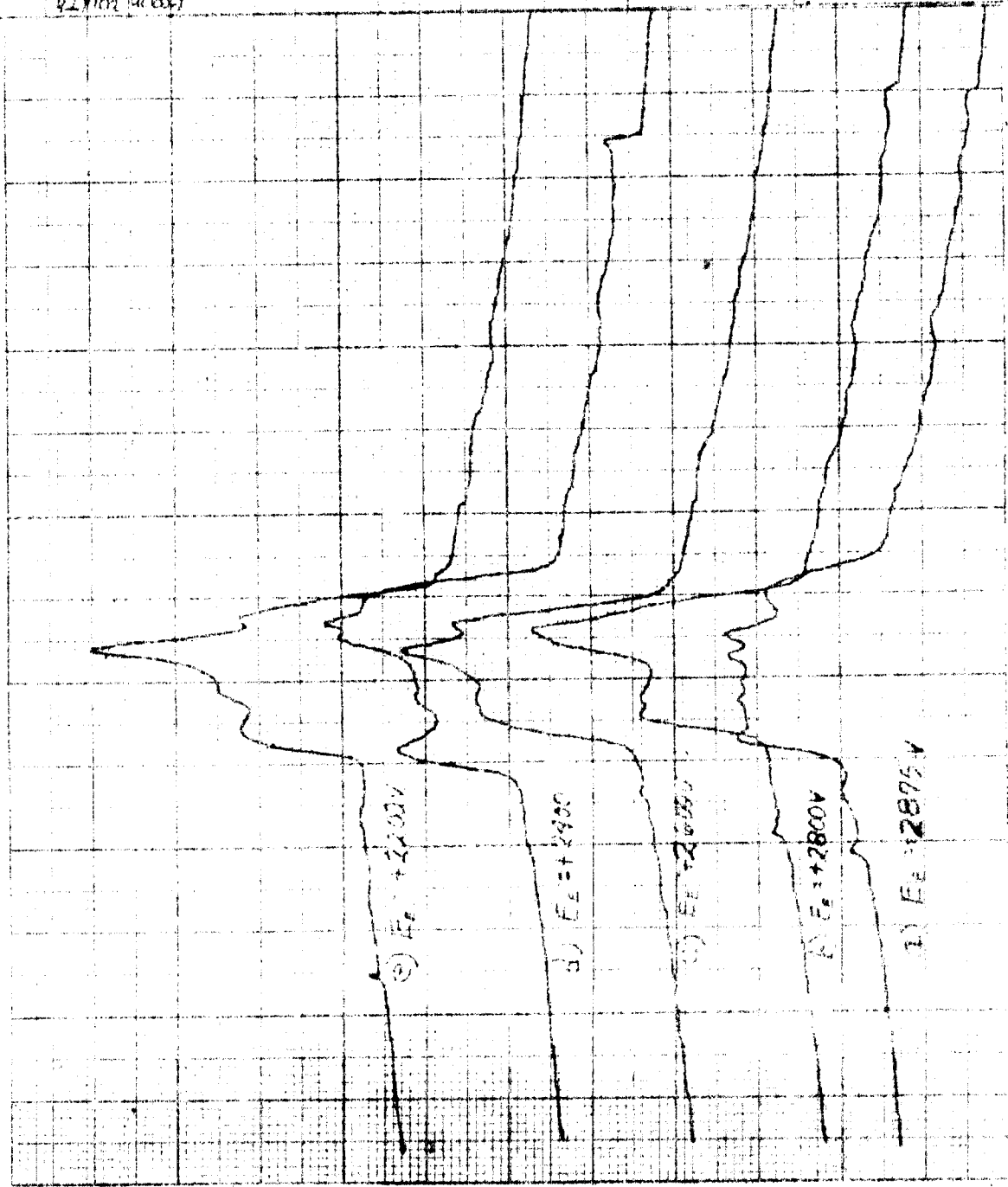


Beam Width (inches)	Accelerator Voltage (kV)
6.0	4000
5.0	4500
4.0	5000

Beam Width (inches)	Accelerator Voltage (kV)
6.0	4000
5.0	4500
4.0	5000

Beam Width (inches)	Accelerator Voltage (kV)
6.0	4000
5.0	4500
4.0	5000

Beam Width (inches)	Accelerator Voltage (kV)
6.0	4000
5.0	4500
4.0	5000

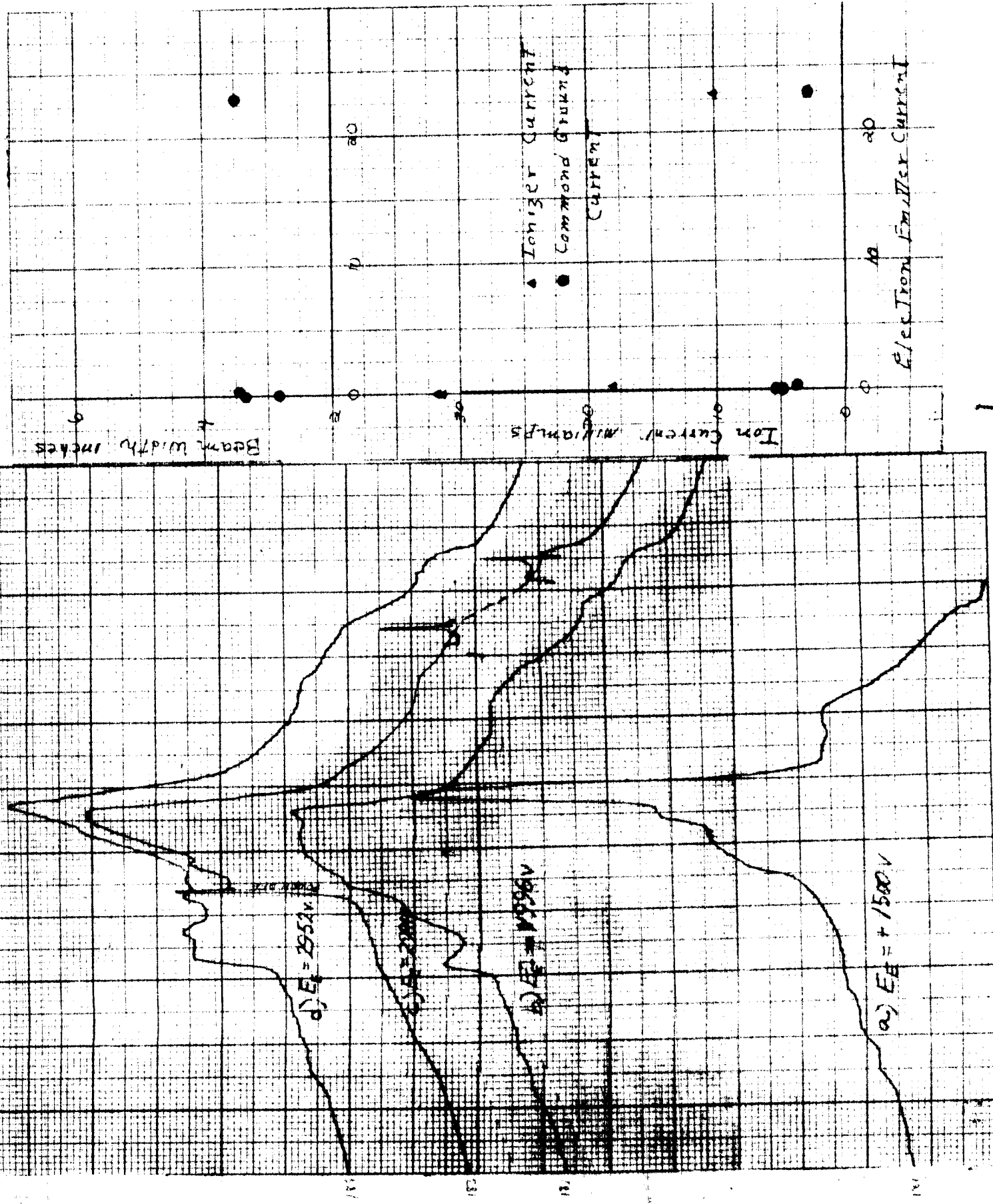


Temp	Ion Current
2875V	1.0
2800V	0.8
2650V	0.6
2400V	0.4
2200V	0.2

Prof. Is	Ionizer Current	Common Ground Current	Electron Gun Current	Electron Gun Voltage
a	10 ma	2.7 ma	23 ma	256 V
b	8	3.8	18	256 V
c	31.5	5.5	0	420 V
d	31.8	4.6	?	420 V

IONIZER VOLTAGE = 4200 V
HEAT = 100 W

FIGURE 1
EMISSION OF THE IONIZER
OF IONS.



Appendix C- Langmuir Probe Measurements

A probe is a conducting surface, often a wire, inserted into a discharge which in most cases is a uniform plasma. Thus the number densities N^+ and N_e of ions and electrons are equal, and the ion and electron temperatures T_i and T_e are independent of position: at low gas pressures $T_e > T_{\text{gas}}$.

Consider a single probe P connected to a voltage source V_B as in figure 1 to this appendix, and immersed in such a uniform plasma. With the anode A connected to the other side of the voltage source, the relationship

$$V_B = V_{AS} + V_{SP}$$

holds, where S is a point in the plasma just outside the zone of influence of the probe, and V_{AS} , V_{SP} are the potential drops between A and S, and S and the probe respectively.

When V_B is large and its polarity such that P is negative with respect to S, all the electrons in the plasma are repelled from the probe, but an ion current flows to it. A fall space develops in front of P with an electric field that decreases from the probe to the boundary of the plasma, where it is zero: the thickness of this space is d . Thus ions cross the boundary by virtue of their thermal velocities, v^+ being the average. Their number per cm^2 and sec is

$$n^+ = \frac{1}{4} N^+ v^+$$

where the positive ion current density at the probe is en^+ which is independent of V_{SP} and depends on N^+ and T^+ only.

In the absence of collisions in the fall space between the ions

and the ambient gas molecules, the current density at the probe is the same as if there were an ion emitting electrode at the plasma boundary,

$$j^+ = \frac{1}{9\pi} \left(\frac{2e}{m^+} \right)^{1/2} \frac{V_{SP}^{3/2}}{d^2} = \frac{1}{4} e N^+ v^+$$

If the probe is too large (that is greater than the mean free paths for ions or electrons) the ions collected come from a larger volume of the plasma, and the plasma boundary may become blurred. Ionizing collisions in d would make j^+ increase with V_{SP} , and ions as well as photons and metastables would fall on the cathode, producing secondary electrons. The probe would finally become the cathode of a glow discharge.

For any V_{SP} the measured current density at the probe is

$$j = j^+ + j_e$$

and hence the electron current density can be found by allowing for j^+ . The variation of $j_e = f(V_B)$ can be obtained by varying V_B so that a larger fraction of slow electrons in the distribution can reach the probe. As V_{SP} is reduced the sheath thickness d becomes smaller. Thus the probe field acts on a region through which electrons of temperature T_e fall without colliding with molecules, but are retarded by a potential V_{SP} . This gives rise to a current

$$j_e = en_e = \frac{1}{4} e N_e v_e \exp(-eV_{SP}/kT_e).$$

Thus

$$\frac{\partial (\ln j_e)}{\partial V_{SP}} = \frac{-e}{kT_e} \quad (V_{AS} = \text{const})$$

showing that the slope of the semi-log plot $\ln j_e = f(V_B)$ gives T_e .

When $V_B = V_{\text{zero}}$ for $j = 0$ and $j^+ + j_e = 0$, V_{zero} is negative with respect to P and the rate of arrival of ions and electrons is equal. Then at the plasma boundary

$$(N_e v_e / 4) \exp \left\{ \frac{-eV_{sp}}{kT_e} \right\} = (N^+ v^+ / 4)$$

$$\text{and } V_{sp} = \frac{kT_e}{e} \ln \frac{v_e}{v^+} = \frac{kT_e}{e} \ln \frac{v_e}{v_{gas}} = \frac{kT_e}{2e} \ln \left(\frac{T_e}{T_{gas}} \cdot \frac{m^+}{m_e} \right)$$

since $N_e \sim N^+$ and $v^+ \approx v_{gas}$.

When $V_B = V_{AS}$ the relation for $j_e = f(V_{sp})$ should suddenly change into a less steeply sloping function, the kink indicating that the probe is at plasma potential ($V_{sp} = 0$). For larger positive potentials the probe acts as an anode, attracting electrons from the depths of the plasma until the whole discharge current flows into the probe.

Figure 2 shows a typical Langmuir single probe characteristic.

It is clear that the insertion of a probe into the Cs ion beam in the experimental facility is not the same as the case described above, and interpretation of results in the light of the above analysis is fraught with danger. However it is known that simple results have been obtained under conditions where 'the probe theory' was invalid ¹⁾, and the experiment itself is simple to perform.

The probe, consisting of a small tungsten wire connected to a variable power supply, was constrained to move along a line mutually at right angles to the beam axis and the locus of the hot wire probe. It might be expected to receive positive

1) A. von Engel: Ionized Gases Clarendon Press, Oxford (1965)

ions from the beam and electrons which are attracted to the region: the case is somewhat similar to that treated by Langmuir ²⁾ for a beam of electrons having a high drift velocity and a small superimposed Maxwellian distribution.

Figures 3,4 and 5 show probe characteristics for different beams, measured essentially on axis and at the beam edge. These plots are on a linear scale, with the probe potentials measured relative to ground. The low knee of the curve is the point where electrons as well as ions reach the probe. All characteristics show that several hundred volts must be applied to the probe to reach the point ($j = 0$) where ion and electron currents are equal. As the voltage is made more positive, the electron current rises approximately exponentially, but the point which might be said to correspond to plasma potential was never reached. It should be remembered that the anode was at 2 kv positive potential with respect to ground in these experiments.

The meaningful interpretation of these characteristics was negated by a further experiment: figure 6 shows the effect of altering the potential of the screen.

no paragraph This is clearly because the screen repels electrons originating at the walls of the chamber, and has a profound ~~effect~~ influence on the number density and distribution of electrons in the neighbourhood of the probe.

2) I. Langmuir and H.M. Mott-Smith: Phys. Rev. 28, 727 (1926)

It might be said in conclusion that although they are not amenable to treatment by the usual probe theory, our results do show some of the same features. Despite the wide departure from an ideal plasma in our experiments, the resultant characteristics are both interesting and almost predictable.

Figure Captions

1. A single Langmuir probe.
 2. A typical probe characteristic.
 3. Experimental probe characteristic.
 4. Experimental probe characteristic.
 5. Experimental probe characteristic.
 6. The effect on the probe characteristic when the screen potential is altered.
-

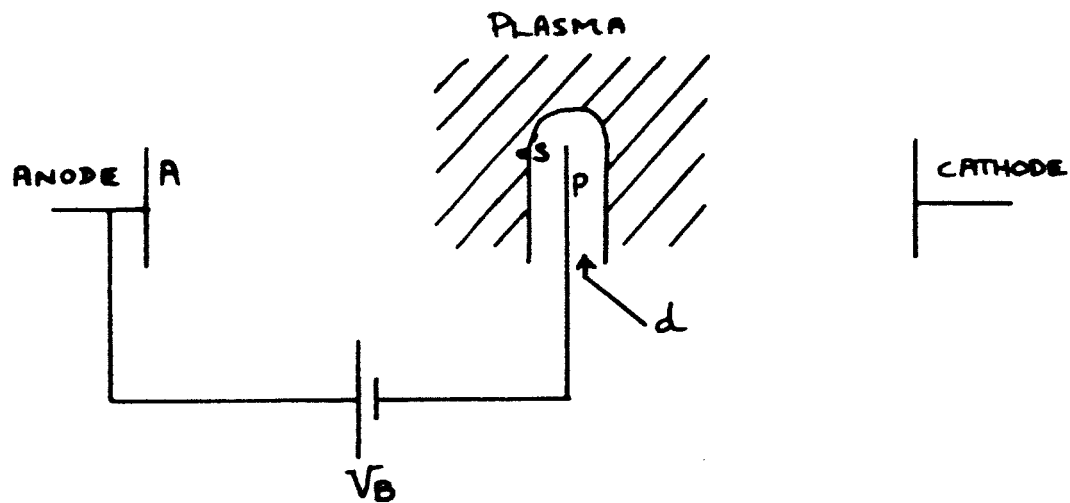


Figure-1

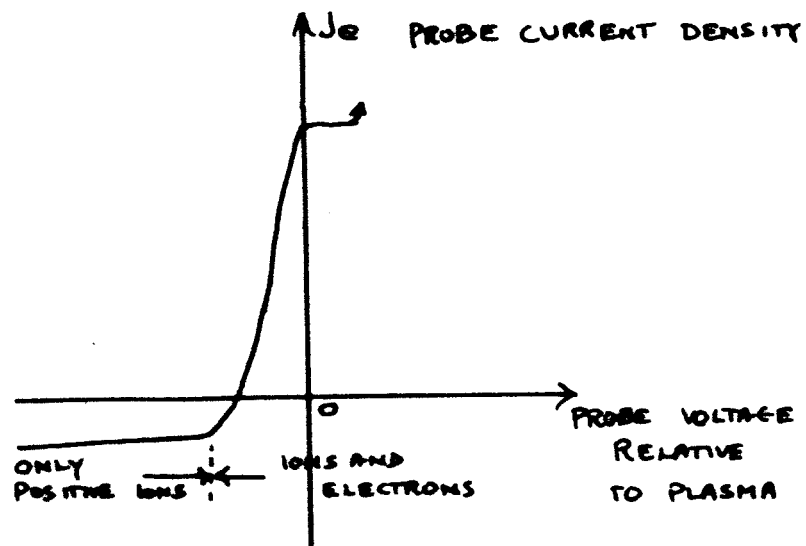


figure 2.

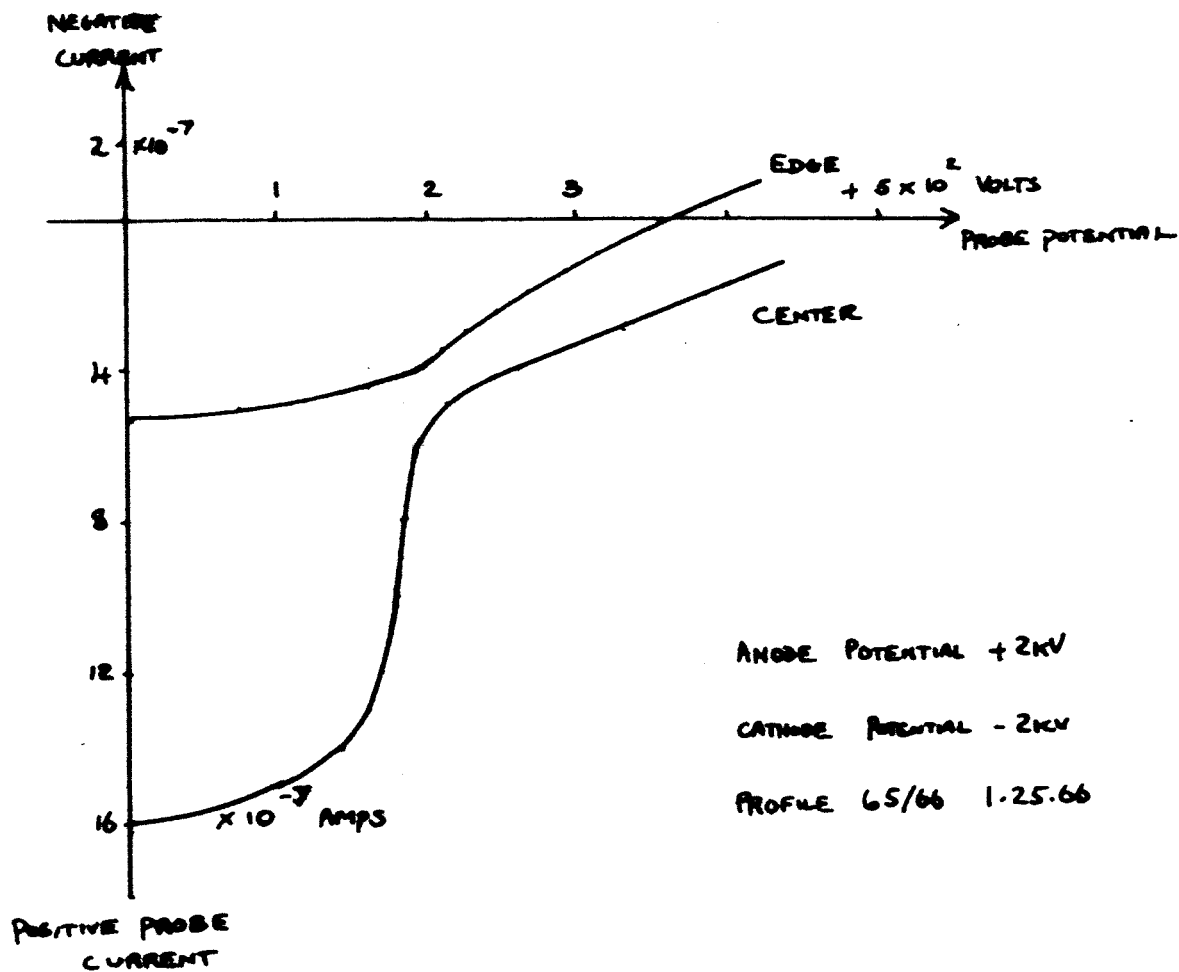


figure 3

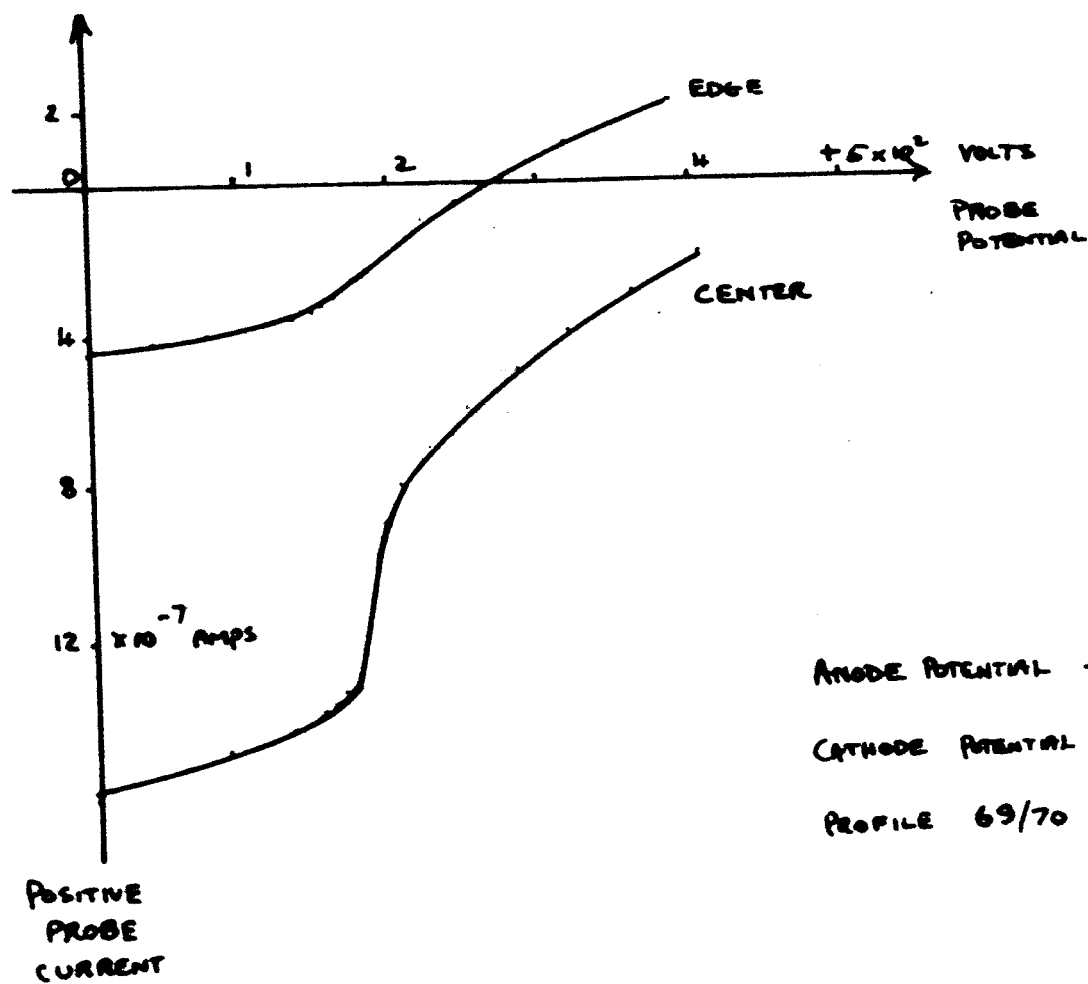


Figure 4

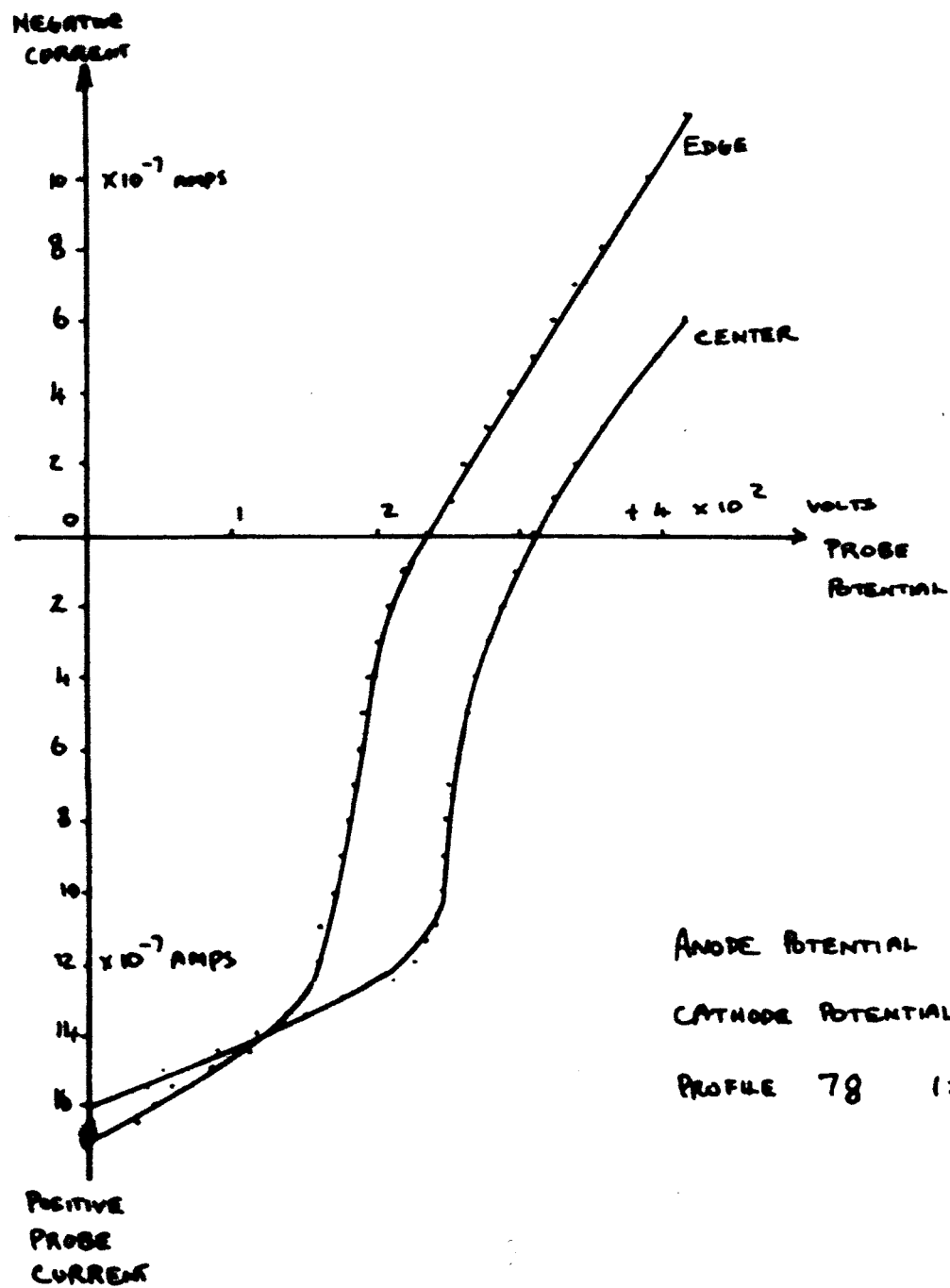


Figure 5

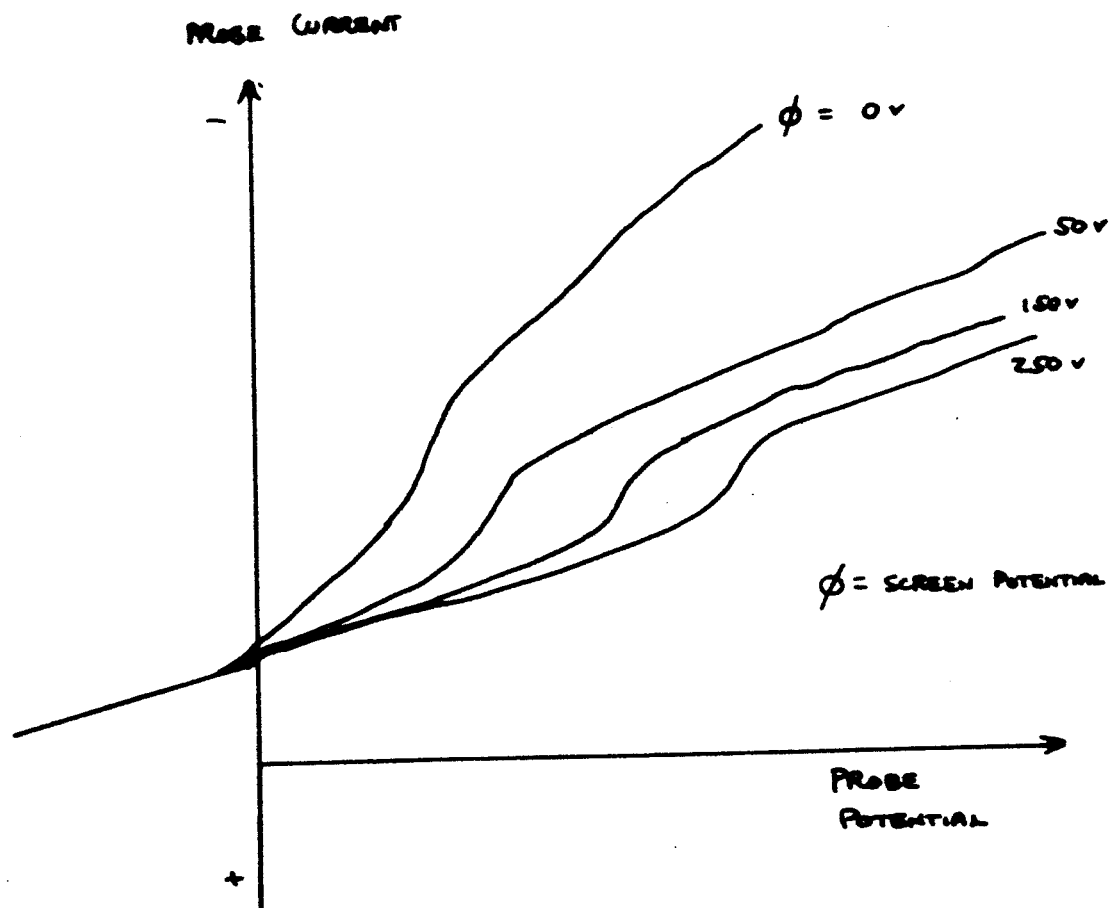


Figure 6

APPENDIX D
SECONDARY ELECTRON EMISSION
BY
ROBERT BUNNEY

Secondary Electron Emission from Porous Tungsten Surfaces.

I. Purpose of the Study- When electrons are injected into the beam of an Ion Rocket Thrust Augmentor a definite enhancement of the beam current is observed (Ref.). These injected electrons acquire high kinetic energies in the field of the accelerator and thus can not reasonably contribute to the Neutralization of the space charge since (1) their actual time in the space charge is very short and (2) their kinetic energies are far too great to effect neutralization of the space charge plasma. Therefore, one must turn to some other mechanism to explain beam enhancement. This is accomplished through postulating secondary emission from the emitter surface.

These secondary electrons are emitted from the ionizer surface with approximately the correct energy for (1) recombination with the positive cesium in the surrounding space charge allowing the neutral atoms to reemit from the field thus, reducing the space charge or (2) with the proper energy to become entrapped in the positive cloud and thereby partially reducing the plasma charge with the same net result as recombination. These considerations are expanded under a separate cover (Ref.).

The secondary emission data needed for the above model are not available for porous materials in general and porous tungsten in particular. To date, the best information available are for comparisons between smooth and "synthetic" rough surfaces. This allows some predictions and order of magnitude calculations to be made but confidence in these results are low. This study has thus been undertaken to obtain the necessary data for the model.

II. Apparatus-

A. Collector.- The electron collector was designed to provide flexibility for a number of independent experiments. These are:

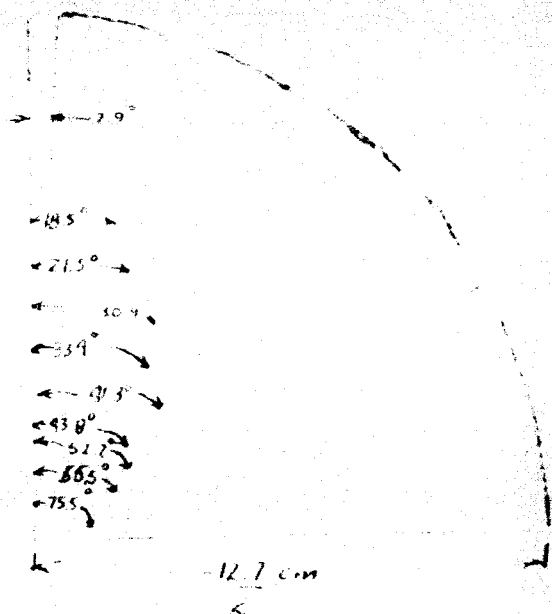
1. To measure total secondary emission over 2π solid angle from the target (ionizer) surface.
2. To measure secondary emission as a function of angle from the normal to the target surface.
3. To measure the energy of the secondary electrons.
4. To measure secondary emission as a function of the angle of the primary beam.

To obtain the above, a hemispherical shell was divided into concentric segments and split bilaterally and was mounted in a porcelain support. Entrance apertures were drilled at 15° intervals from the origin for the primary beam. This allowed step 4 above. Finally a repulsion grid was mounted and insulated from the collector segments, (Fig. 1 and 2) to do secondary energy studies.

B. Electron Gun- A standard cathode ray tube electron gun was used as a primary source. It was found however that the original filaments once exposed to the atmosphere were unreliable and so they were replaced with thoriated tungsten filaments. This new filament proved to be reliable for filament currents to 7-amps.

C. Schematic of Electronics

Figure 3.



$$\pi R^2 = 508 \text{ cm}^2$$

S. d. (cm)		$A' (cm^2)$	$A (cm^2)$	$\Delta A (cm^2)$	$\theta (deg)$	Ω (steradian)	
.056	.999	.051	(6.44) 25.8	.267	10.6	.160	95.1
.323	.998		3 (9.12)	.164	26.1	.226	96.4
.376	.930	.072	36.5 4 (10.6)	.138	37.5	.264	97.0
.540	.838	.084	42.6 4 (13.8)	.146	48.4	.342	97.7
.583	.835	.109	55.2 4 (40.0)	.350	64.9	.996	99.2
.721	.751	.117	100.7				
.766	.722						
.712	.615						
.909	.561						
1.319	.250						

B. Yield

The yield experiment for secondary electron emission from porous tungsten has produced some interesting results. As predicted previously (Dekker, A. J., Secondary Electron Emission, Solid State Physics, Academic Press 1948) the yield decreases for rough surfaces. The porosity of the surface can to a certain extent be regarded as a rough surface and this decrease in yield has in fact been observed. For smooth surfaces, McKay (Advances in Electronics, Academic Press, Vol. 1, p.68 1948, stated δ max to be 1.4 at V_p (max) of 600 volts. The δ max in porous tungsten appears to be between 1.10 and 1.13. Not predicted however is the apparent shift of V_p (max) from 600 volts to 125 volts. These curves are shown in figures 6 to 9. The numbers previously mentioned were obtained with the primary beam uniformly distributed across the target surface.

It is interesting to note however that if the incident beam is focused to a small spot on the target the yield increases greatly. As is shown in fig.10, for this condition $\delta(\text{max}) = 2.12$ at V_p (max) of 225 volts. This phenomenon is explained however through incident surface energy density. The energy per unit area applied to the target through homogeneous bombardment is much less than a focused spot on the surface. The secondaries produced at this spot should then have more energy available to them for transition through the interspace of the material therefore increasing their probability of escape to be measured.

The fine structure observed in the yield curve is of particular interest. It is noticed from the curves that there appears to be a definite reproducible absorption region at about 125 volts. Similarly, another reproducible absorption band appears at 75 volts which is not nearly as intense. Further, there also could be similar structure at 25 volts, 175 volts, etc. Although these were not nearly as intense or reproducible. Thus, it would seem that there is an absorption phenomenon taking place at 50 volt intervals.

III. Results-

A. Secondary energy distribution-

The energy distribution of the secondary electrons in porous tungsten is shown in figures 4 and 5. This distribution is limited to the so-called "true" secondaries of energies ≤ 50 ev. The rest of the characteristic curve $50 \text{ ev} \leq E_p$ could be produced, however this region is beyond the general scope of this study. As is seen from the curves, the secondary maxima is highly localized around the $0 \leq \epsilon_{\text{max}} < 10$ V region and is independent of the primary potential over a wide range. This highly substantiates the original assumption that secondary electron emission is a bulk property of the material and not as a general rule a property of surface states. In the latter case, one would expect the secondary energy to be a distinct function of the primary energy. It is rather surprising that the maxima energy is as low as ≈ 2.5 volts, however it is certainly within the range of previously reported results (i.e., Dekker, A. T.;).

To explain this phenomenon one must consider it to be one of the following:

- (1) Apparatus difficulties
- (2) Atmosphere absorption characteristics
- (3) Bragg reflection
- (4) Characteristic absorption spectra
- (5) Characteristic of porous materials.

These are considered individually.

1. Apparatus difficulties: The fine structure appears to be independent of the primary source, i.e., several different electron guns were used collecting this data and the same fine structure appears consistently. The collector assembly is symmetrical with respect to the target surface so one must ignore divergent preferential fields. The same meters were used to measure both the primary and secondary currents discounting any non-linearity of measuring devices as contributing to the fine structure in the ratio. Thus, one must discount at least as a first assumption difficulties with the apparatus as a contributing factor.

2. Atmosphere absorption- Certainly, if the apparatus were being operated in an atmosphere one would expect preferential absorption and scattering of the electrons at certain energy levels. However, one would perhaps think that both primary and secondary beams would be effected with equal probability and therefore have a self nullifying effect in the ratio. Further in the course of these experiments the usual pressure was on the order of 2×10^{-6} torr giving a very long mean free path. Thus, for this reason alone, atmosphere absorption should be negligible and should then be discounted.

3. Bragg Reflection- The fine structure, being periodic would exhibit Bragg reflection characteristics. However, the target being composed of sintered tungsten has interdistance of the order of a micron. From the Bragg reflection law, this distance would require electrons of wave length corresponding to 1.24 ev. Thus, this fine structure, to be caused by Bragg Reflection, must have spacing two orders of magnitude smaller than that in the target. Thus, it would seem that this also must be discounted as a possibility.

4. Characteristic Absorption Spectra- If this were a possibility, this phenomenon would occur in smooth surfaced materials as well as rough and porous materials and would have been previously found by experimenter's in all materials. This has not been reported in the literature. Further, it is highly unlikely that the energy differences between the absorption lines would be exactly 50 volts. Further, the normalized yield curve as exhibited in Fig. 10 still shows the fine structure. As this curve has been reported to be a so-called universal curve, absorption spectra could not appear in each of these curves. This gives confidence ~~that~~ secondary emission is generally independent of the absorption spectra.

5. Characteristic of Porous Materials- It is this experimenter's conclusion, based on the data thus far obtained, that this is the most plausible explanation of the observed fine structure. Since the $\delta(\max)$ shift is observed as reported in Dekker one has a certain amount of confidence ~~that~~ surface roughness is accounted for, thus one must now explain the structure. It is highly possible that the porosity of the material in question can cause a semi-homogeneous surface of "wells". These wells could easily preferentially absorb electrons of the correct energy.

C. Angular dependence of yield

The angular dependence of secondary electrons from porous materials is shown in fig. 11. It is noticed that these curves are quite similar to those produced in the literature, i.e. Bruining, H., Secondary Electron Emission, Pergammon Press (1954). Thus it would appear that, with exception of the rough surface correction, that the angular dependence of emission is not changed in porous materials.

IV Suggestions for further study.

This investigation has given results which should lead to many further investigations. Certainly the yield fine structure should be investigated more thoroughly with far more emphasis placed on investigating the absorption at 25, 175, etc. volts. This study should be extended to other porous materials to determine to what extent this phenomenon relies on the material used and to what extent the porosity of the material. Further, the surfaces should be contaminated. To investigate this phenomenon as a function of the contaminate.

Also, further study should be performed to determine the secondary electron characteristics as a function of primary surface energy density.

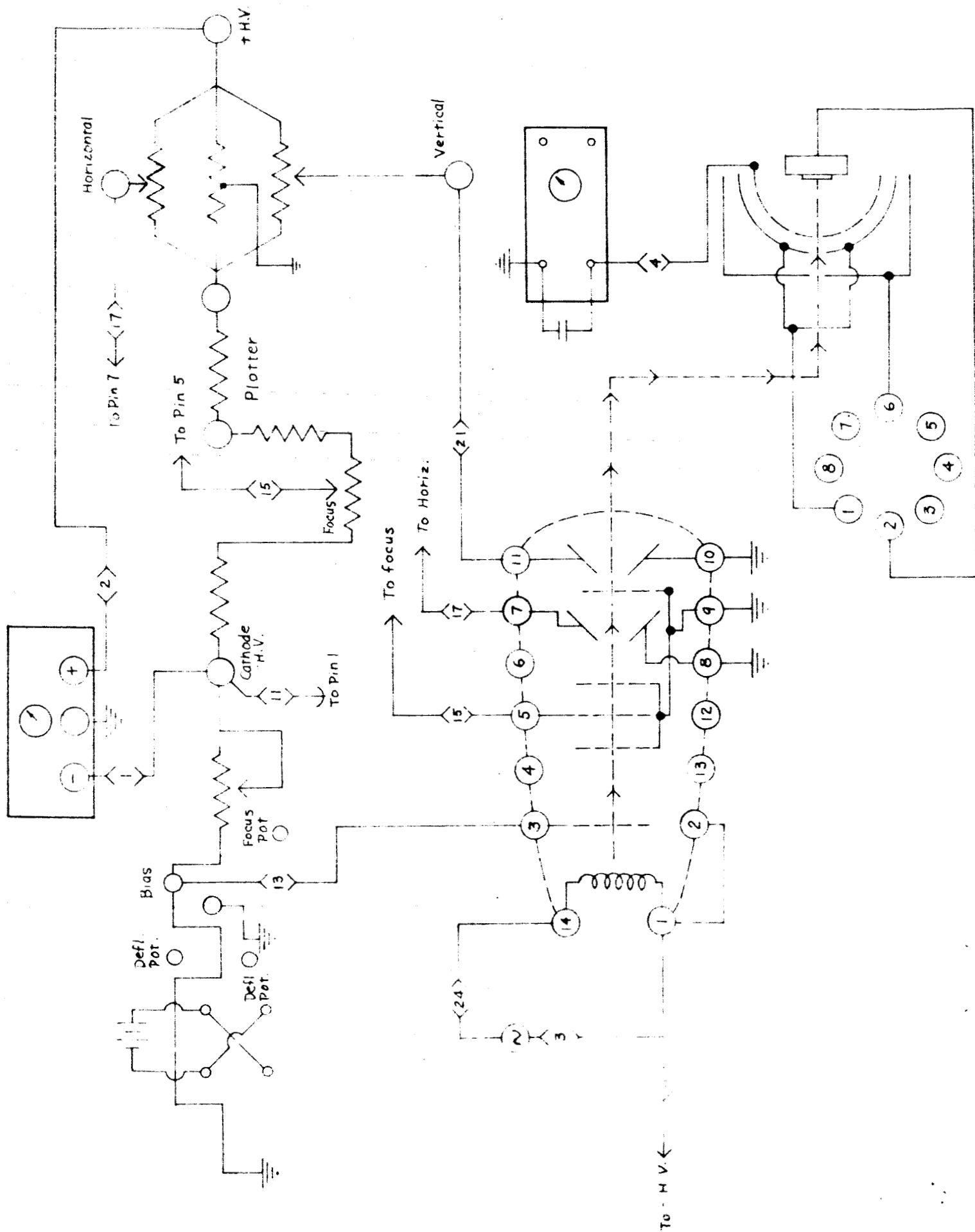
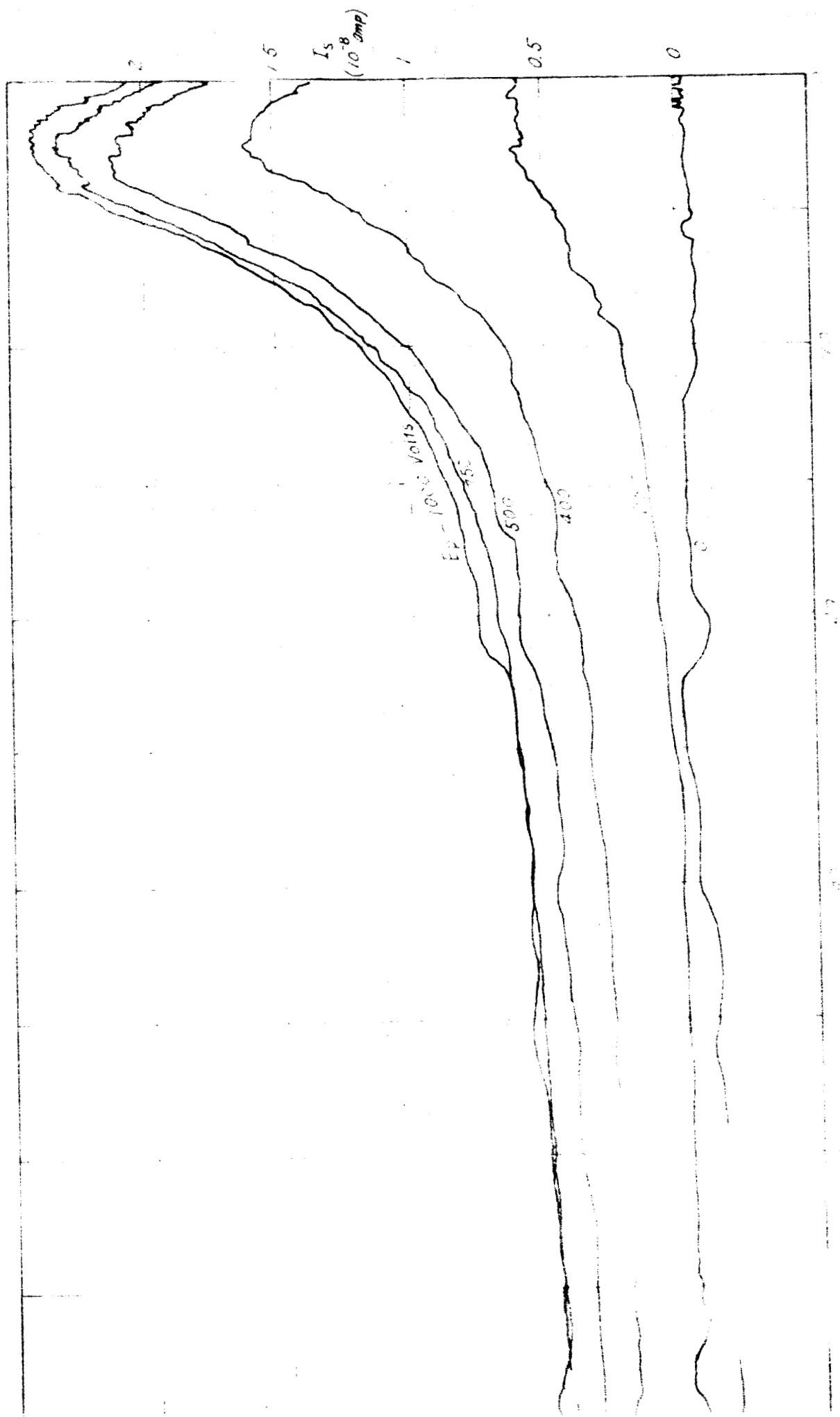
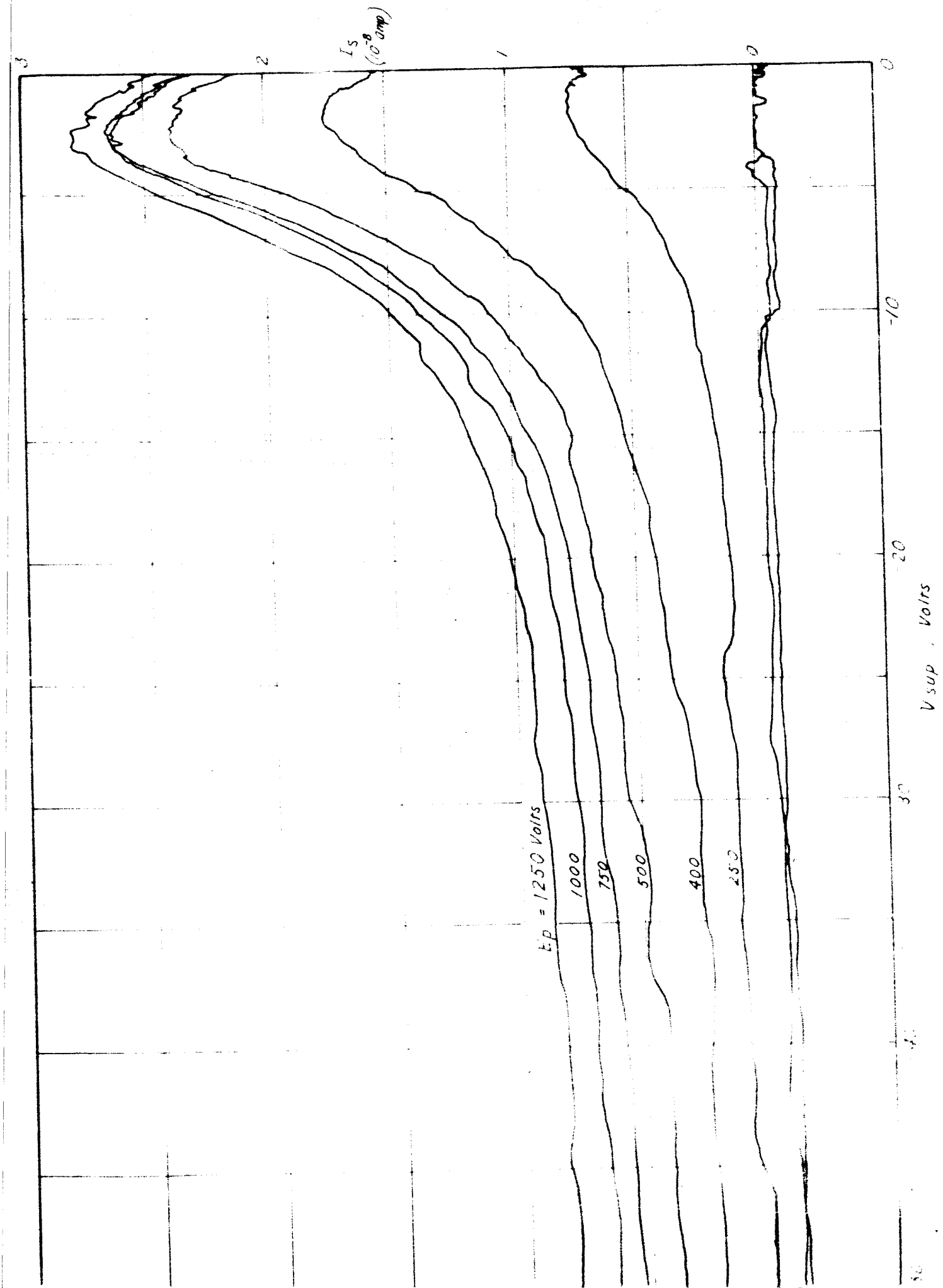
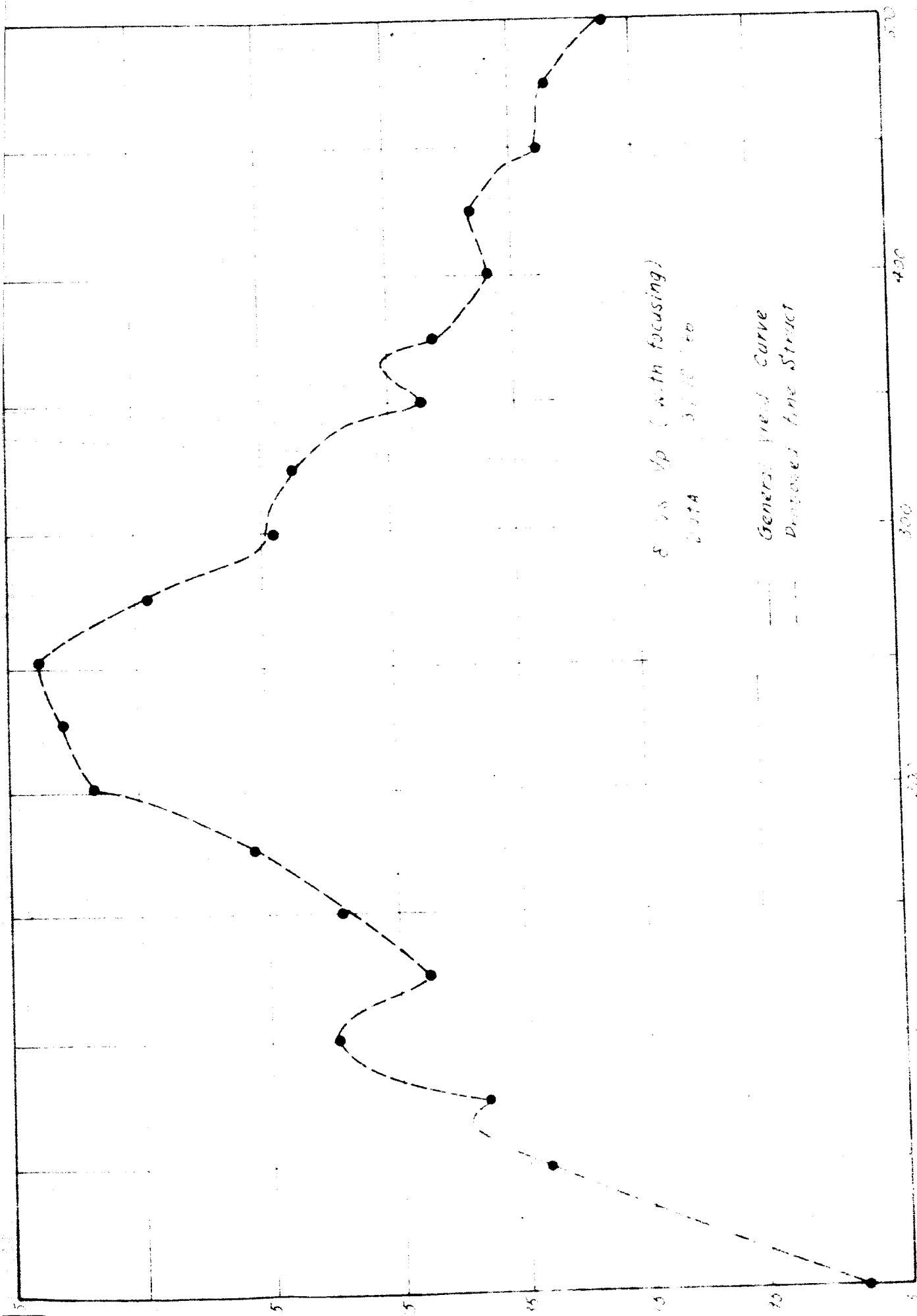
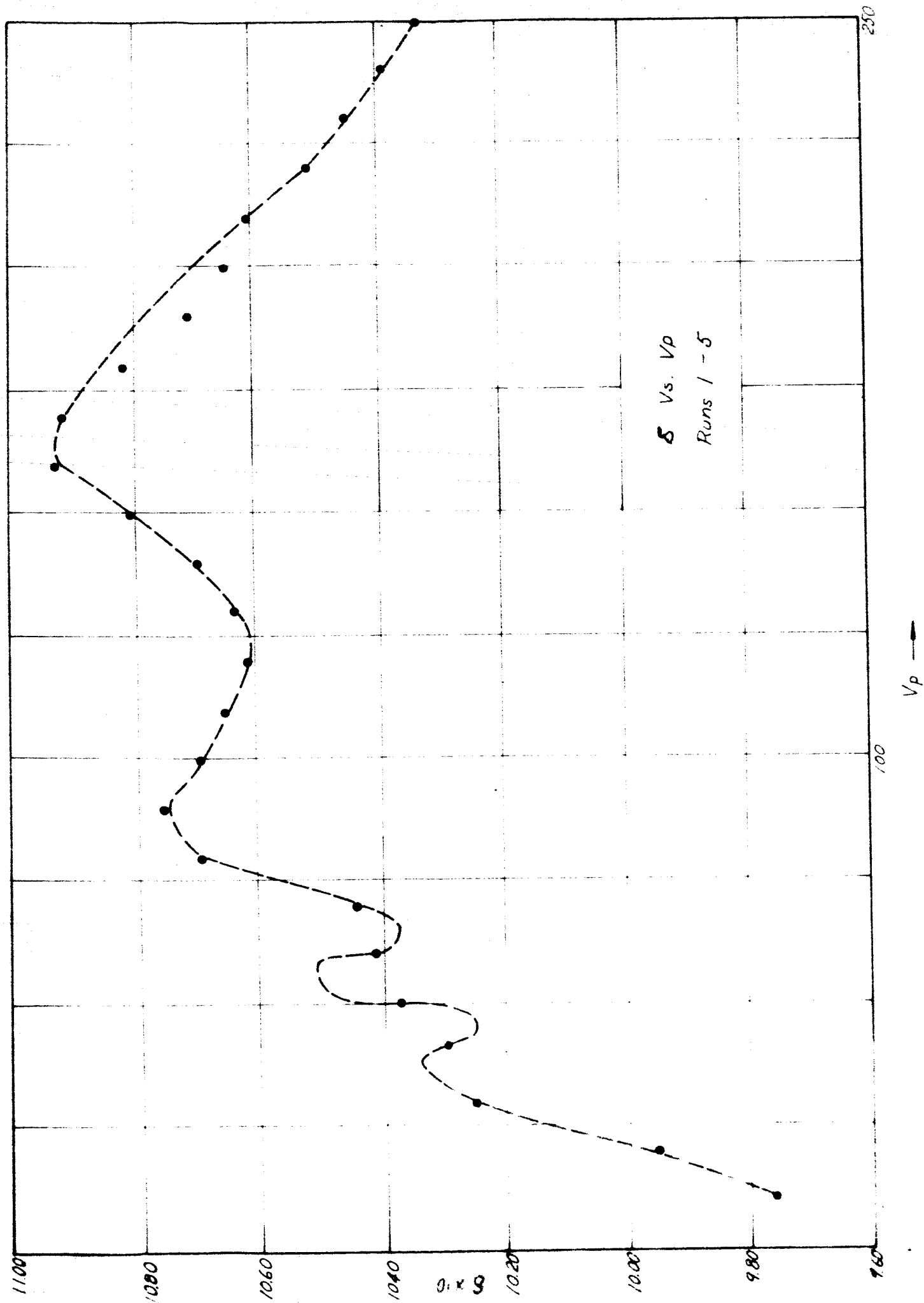


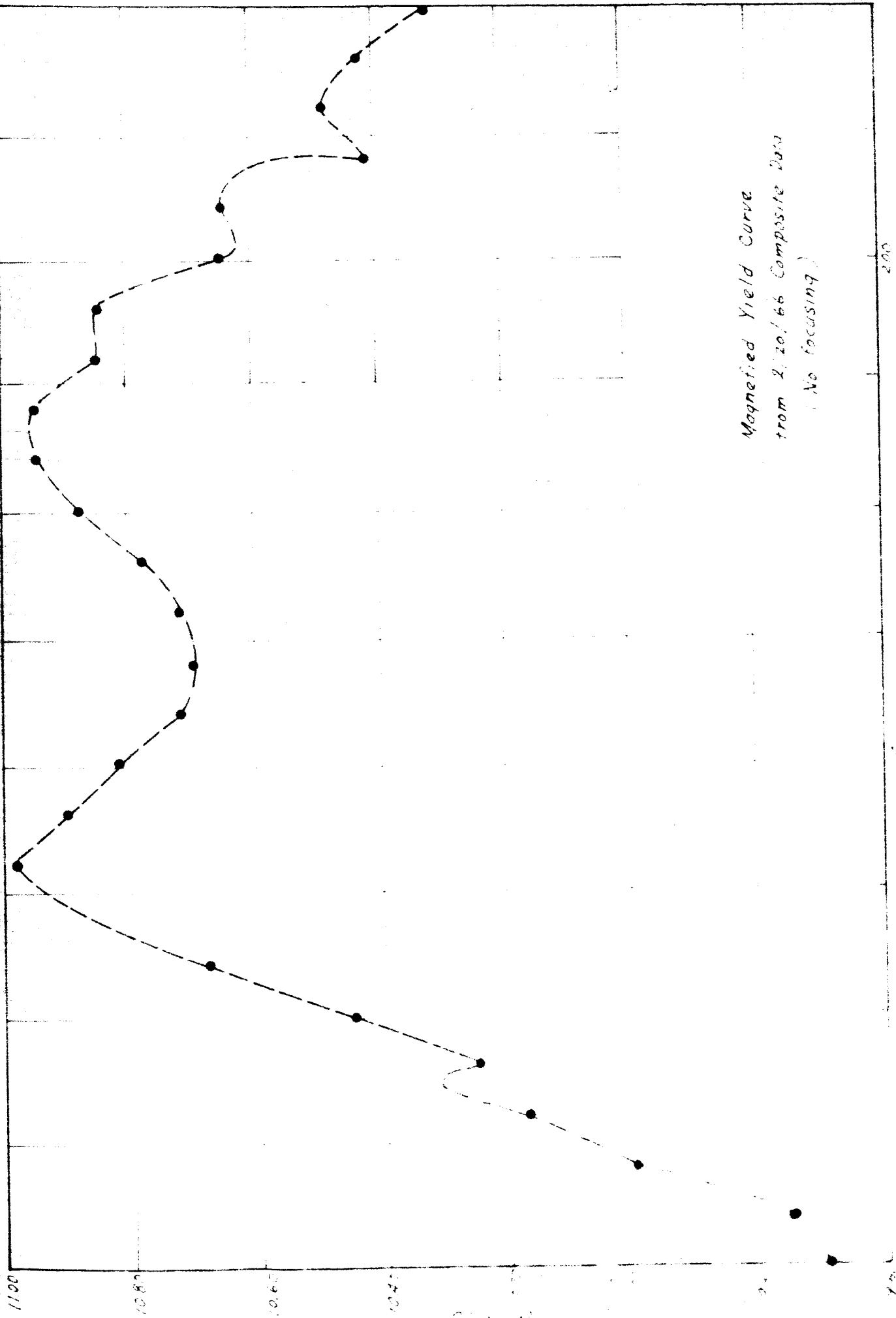
Fig. 3



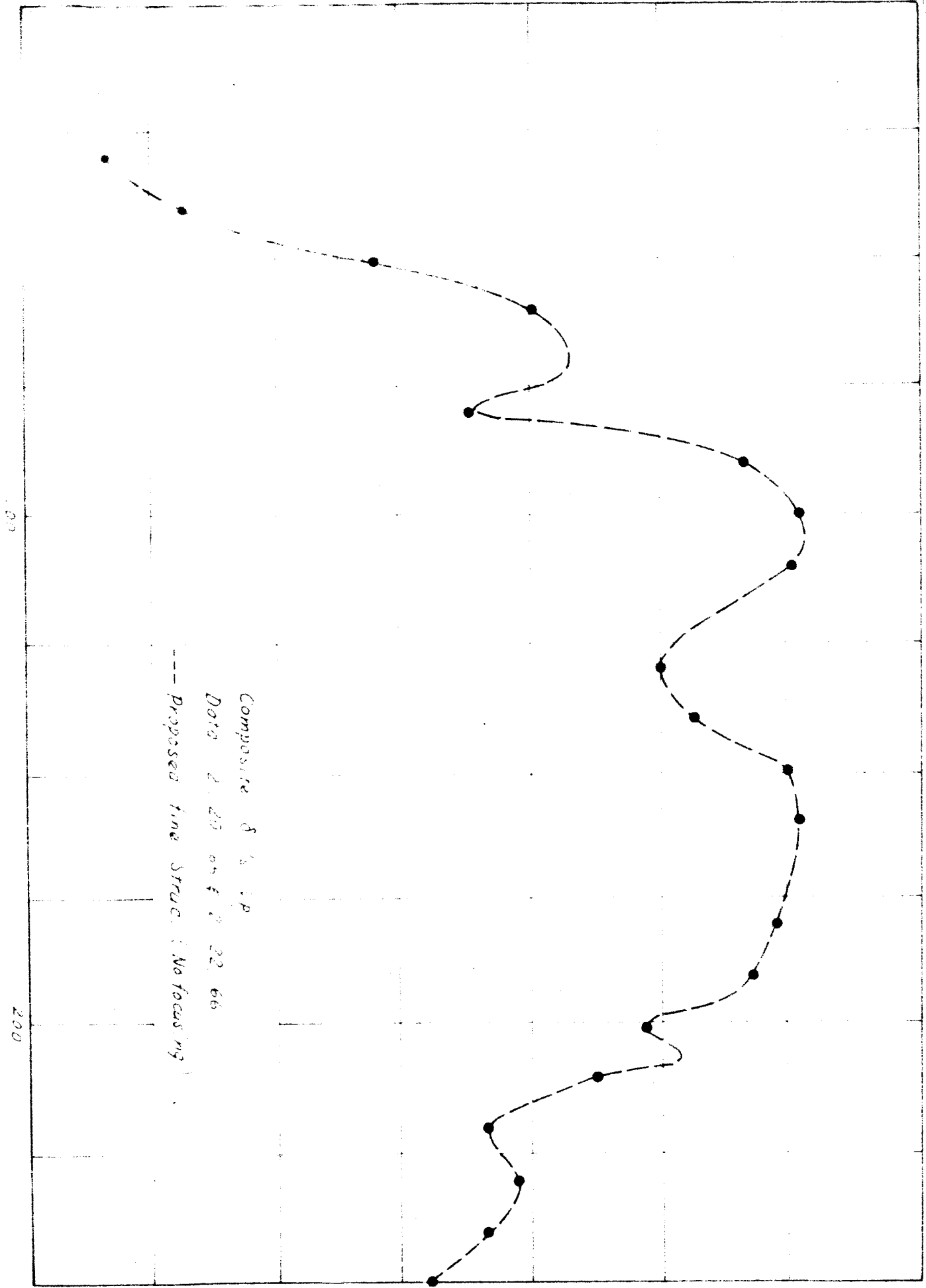


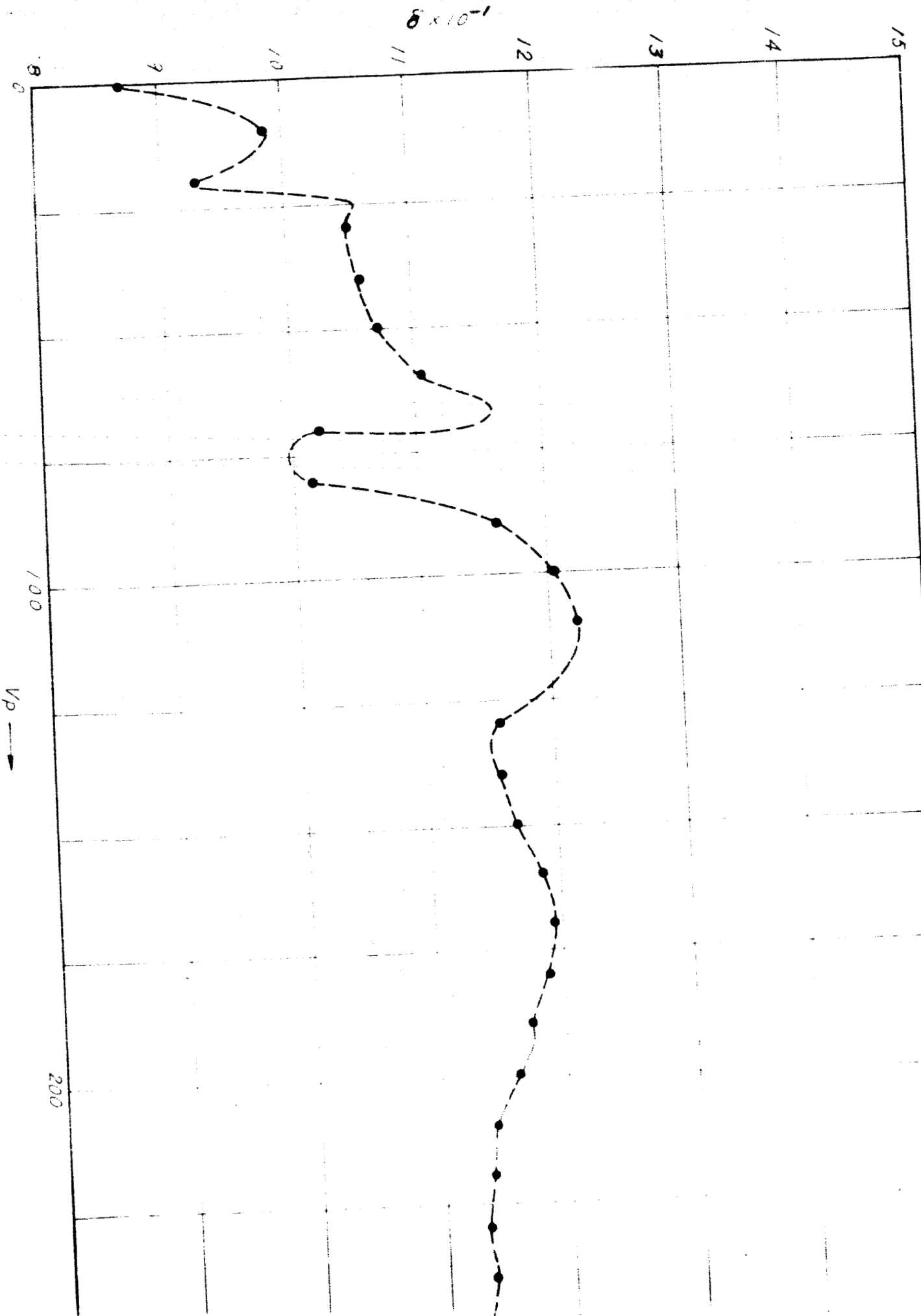






Magnetized Yield Curve
from 2, 20, 66 Composite Data
(No focusing)





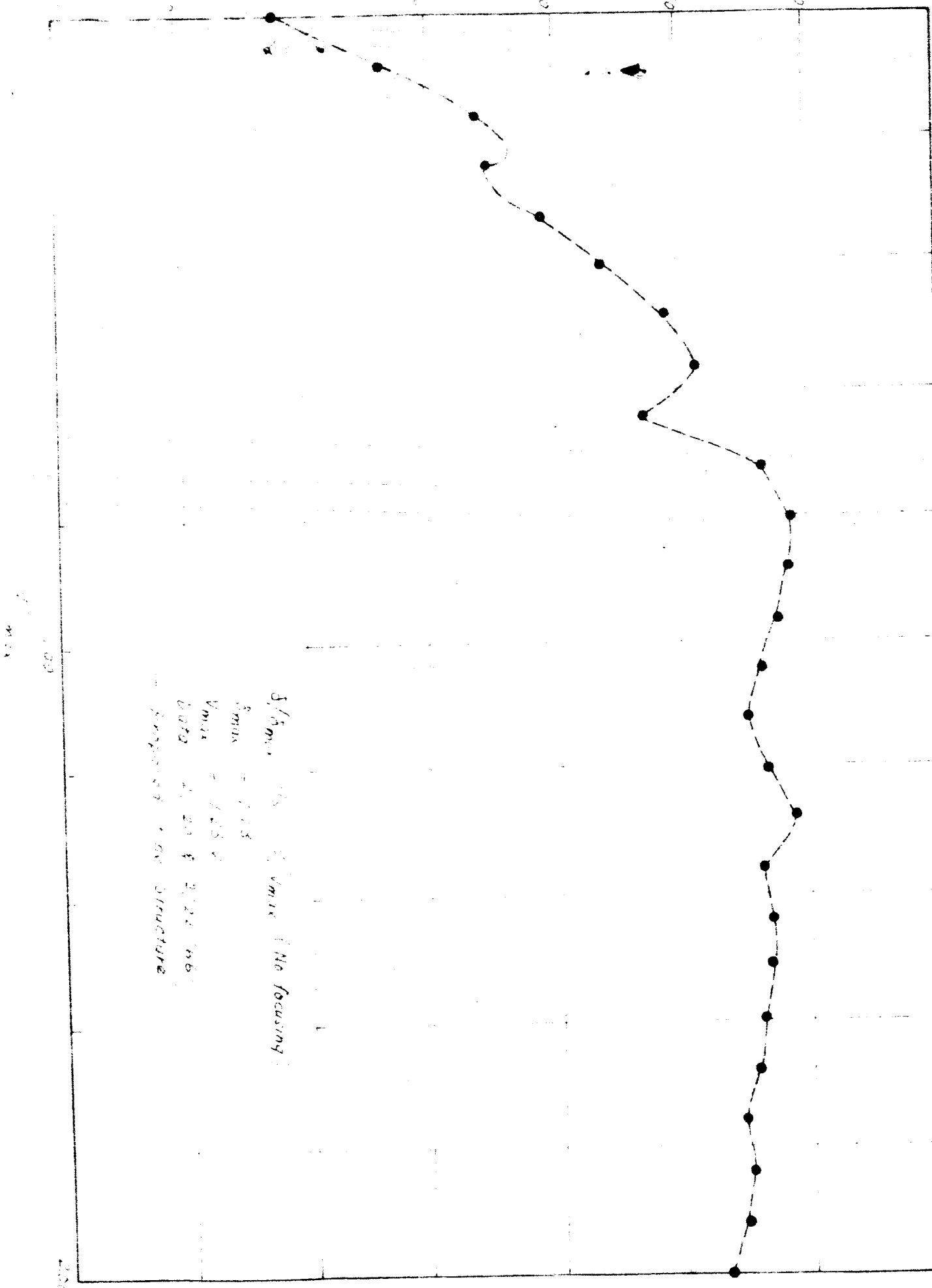


Fig. 11

N66 36790

THESIS

**HEAT TRANSFER FROM LARGE DIAMETER PIRANI
GAUGES OPERATING DOWN TO A MICROTorr**

Submitted by

John E. Braly

**In partial fulfillment of the requirements
for the Degree of Master of Science
Colorado State University
Fort Collins, Colorado
March 1966**

Chapter I

INTRODUCTION

Pirani (1) was the first to describe a gauge based on the relation between the heat conducted from a wire and the pressure. Since then, wide application and development of the gauge have taken place as is evident from the excellent review of the literature by Dushman (2) .

The typical Pirani gauge is a fine wire, 0.5 mm diameter, enclosed in a larger diameter tube. The small diameter wire has high resistance, thus it can be resistively heated with small currents. As the pressure is lowered, the gauge becomes hotter since fewer molecules are present to carry away energy. As the temperature of the wire rises, the resistance rises. Under constant current operation, the potential difference across the gauge increases proportionally with resistance. This increase in voltage can then be measured and related to the pressure.

Pirani and Yarwood (3) report the pressure range for commercially available Pirani gauges to be from 10 torr to 10^{-4} torr. They indicate, however, that by special design the pressure range can reach 1000 torr for the upper limit or 5×10^{-6} torr for

the lower. Ellett and Zable (4) report extending the lower limit even further to 10^{-8} torr by cooling the outside wall with liquid air (Appendix B) .

It will be shown in Chapter II that the conduction of heat from the wire is dependent on the radius of the wire. Large diameter wires, however, are impractical because of the large currents required to heat them. Thin films on large diameter cylindrical substrates were therefore proposed (5) as a solution to the problem. The present paper deals with the heat transfer from these large diameter cylinders.

Chapter II

THEORY OF HEAT TRANSFER
FROM COAXIAL CYLINDERS

Consider the loss of heat from a cylinder of radius r_1 , and temperature T_1 , arranged along the axis of a cylindrical tube of radius r_2 and temperature T_2 ($r_1 \ll r_2$). At molecular pres-

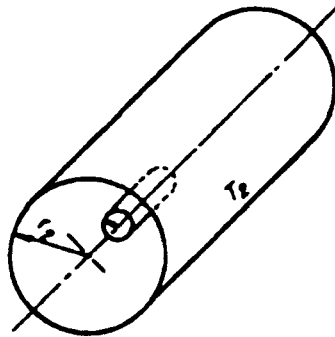


Figure 1
Concentric Cylinders

ures, where inter-molecular collisions are rare compared with impacts on the cylinder and the walls, the thermal conductivity of the gas is a function of the number of collisions with the cylinder and, hence, increases proportionally with the

pressure. Since the cylinder diameter is very small compared with the tube diameter, collisions of the molecules with the walls are much more likely than with the cylinder. Hence, the temperature of the gas may be put equal to the wall temperature. In Appendix A it is shown via kinetic theory that the power lost by the cylinder due to molecular conduction is

$$q_m = 2\pi r_1 l K_m a P (T_1 - T_2) \quad (1)$$

where l is the length of the cylinder, a is the accommodation coefficient between the gas molecules and the cylinder, P is the pressure. K_m is the molecular conductivity of the gas given by

$$K_m = \frac{C_v + R/2}{\sqrt{2\pi RMT_2}} \quad (2)$$

where C_v is the molar specific heat of the gas at constant volume, R is the gas constant, M is the molecular weight of the gas, and T_2 the Kelvin temperature of the gas.

There will also be a loss of heat from the cylinder due to thermal radiation. This is given by the Stefan-Boltzmann Law

$$q_r = 2\pi r_1 l \sigma (\epsilon_1 T_1^4 - \epsilon_2 T_2^4) \quad (3)$$

where q_r is the radiated power, ϵ_1 and ϵ_2 are the thermal emissivities of the cylinder and the wall respectively, and σ is the Stefan-Boltzmann radiation constant.

As the pressure is increased above molecular values, the gas temperature in the neighborhood of the inner cylinder increases above the wall temperature; the proportionality between pressure and rate of heat loss due to conduction, Equation 1, is then no longer maintained.

Von Ubisch (6) refers to pressures immediately above the molecular region as transmolecular pressures. In this region he

gives the semiempirical equations:

$$q'_m = \frac{2\pi r_1 l K_m a P (T_1 - T_2)}{1 + \sigma P} \quad (4)$$

where

$$\sigma = \frac{a r_1}{k' \lambda} \ln \frac{r_2}{r_c} \quad (5)$$

and

$$k' = \frac{9\gamma - 5}{\gamma + 1} \quad (6)$$

λ is the mean free path at the pressure P , γ is the specific heat at constant pressure divided by the specific heat at constant volume, and r_c is a semiempirical constant which is somewhat larger than r_1 at the lower pressures but equal to r_1 at the higher pressures.

When $\lambda < r_1$, the motion of the molecules is limited and there is consequently a temperature difference between the surfaces (of the cylinder and wall) and the neighboring gas layers. In this region the conductivity is independent of the gas pressure and the well known formula applies:

$$q_k = \frac{2\pi l K_v (T_1 - T_2)}{\ln r_2 / r_1} \quad (7)$$

where K_v is the thermal conductivity in the viscous region. In the hot-wire gauge, however, this result is modified because of the temperature discontinuities between the gas and the boundary surface. The modified equation is

$$q_k = \frac{2\pi l K_v (T_1 - T_2)}{\ln \frac{r_2 + g_2}{r_1 - g_1}} \quad (8)$$

where g_i is an apparent boundary shift (Appendix A , Fig. 16) .

According to Von Ubisch (7) , g_i is given to a first approximation, for the gases studied, by

$$g_i = \frac{15}{8} \lambda \left[\frac{2 - a_i}{a_i} \right] \quad (9)$$

Equation 8 applies, therefore, ^{in the} pressure region above the trans-molecular one. Notice q_k is still dependent to a small extent on λ and hence the pressure.

Chapter III

EXPERIMENTAL APPARATUS AND DATA

Preparation of Cylinders

Two methods were used in depositing the films on the substrates. For the "platinum" films a commercial product was used. Hanovia Liquid Bright Platinum is essentially a solution, in volatile oils, and other solvents, of organic platinum and gold compounds of resinous character. When placed on a glazed ceramic surface and heated to maturing, it yields a mirror-like film. The fired film has the luster of platinum metal. Besides the precious metals, Bright Platinum contains some base metal-organic compounds which serve as fluxes to fix the metal firmly on glass or ceramic.

This solution was brushed on a .375 inch diameter solid Pyrex rod which was 1.375 inches long. The film covered the entire curved surface of the cylinder. Copper electrodes of number 22 gauge wire were wrapped around and soldered to each end with Eutectic 157 silver solder (melting point, 425°F).

Bright Platinum was used again on a piece of thin walled (3/64") Pyrex tubing (O.D., .75 inch; length, 1.625 inch). This time the film was formed in the shape of a helix, giving higher

resistance for approximately the same length of cylinder. Electrodes were attached as described before.

The substrate for the nickel film was a piece of mica of thickness 1.1×10^{-3} inches. A metal barbell-like frame was constructed to give the mica the desired cylindrical shape (O. D., 1 inch; length 3.5 inch) when wrapped around it. The nickel film was evaporated on the mica cylinder in a 19 inch bell jar over a Haas chamber. A single source was used with the cylinder rotating above it. Shields were rigged so that either the ends, center, or entire curved surface was exposed. The gauge was first completely covered with nickel. Next only the ends of the curved surface were exposed for a silver evaporation. This thick silver film was for good electrical contact between the nickel and the electrodes. Finally, the ends were covered, center exposed, for a silicon monoxide evaporation needed as protection to keep the nickel from oxidizing and changing resistance when heated. Copper electrodes were mechanically attached to the silver film.

Vacuum System

These gauges were placed in the CSU-NASA high vacuum system for testing. The principle component of the facility is a stainless steel tank 48 inches in diameter and 15 feet long. Attached at each end of the main tank are 16 inch diameter, air-actuated valves and 16 inch diameter bell jars; one being 26 inches long, the

other 45 inches long. The pumping rate of the facility is 3×10^{-7} kilograms of air per second when the 32 inch oil diffusion pump is operating with the tank at 10^{-7} torr. The facility is also equipped with a cylindrical liner that can be maintained at liquid nitrogen temperature. With the liner in operation, condensable-mass-flow rates of several orders of magnitude higher than quoted above are obtainable.

Miscellaneous Apparatus

Pirani (1) pointed out that the gauge could be operated in three different ways.

1. The potential difference across the wire is maintained constant, and the change in current is observed as a function of the pressure.
2. The resistance (and consequently the temperature) of the wire is maintained constant, and the power input required for this is observed as a function of the pressure.
3. The current is maintained constant, and the change in potential difference is observed as a function of the pressure.

In this experiment the gauges were operated according to the third scheme. A constant current supply (built by CSU Electronics) capable of holding up to 300 ma plus or minus 0.1 ma for 24 hours

was used. During the three hour runs no change in current was noticeable. After the system was pumped down to a specific pressure and the temperature of the gauge had stabilized, the potential difference across it was measured by an Electro Instruments five place digital voltmeter (least count, 0.001 volt).

Pressure measurements were made with three different mercury manometers: for the range from atmospheric to 5 torr, a Meriam Instrument Co. open tube mercury manometer was used (least count, 0.1 inch); from 5 torr to 3×10^{-3} torr a swivel form of the McLeod gauge made by Stokes was used; and from 3×10^{-3} torr to 10^{-6} torr, a form of McLeod gauge which has a reservoir that is raised and lowered made by Consolidated Vacuum Corporation (type GM 110) was used.

The temperature-resistance data was obtained by placing the gauges in an oven with a chromel-alumel thermocouple attached to the film. A small constant current was passed through the gauge and the potential difference noted with the digital voltmeter as the temperature was slowly increased.

TABLE 1 - TEMPERATURE-RESISTANCE DATA FOR .375 INCH
DIAMETER GAUGE

Temp °F	V volts	i ma	R ohms	Temp °K
91 ± 1	.123	3.76	32.7	305.8 ± .6
106	.124		33.0	314.1
119	.125		33.3	321.4
132	.126		33.6	328.6
141	.127		33.8	333.5
150	.128		34.1	338.5
160	.129		34.3	344.0
171	.130		34.6	350.2
179	.131		34.8	354.6
192	.132		35.1	361.8
201	.133		35.4	366.8
210	.134		35.6	371.8
220	.135		35.9	377.5
232	.136		36.2	384.1
244	.137		36.4	390.9
252	.138		36.7	395.2
266	.139		37.0	403.1
277	.140		37.2	409.1
290	.141		37.5	416.4
300	.142		37.7	422.0

TABLE 2 - TEMPERATURE-RESISTANCE DATA FOR 1 INCH
O. D. GAUGE

Temp °F	V volts	i ma	R ohms	Temp °K
95 ± 1	.091	3.76	24.2	308.0 ± .6
119	.092		24.5	321.4
134	.093		24.7	329.6
156	.094		25.0	341.8
162	.095		25.3	345.2
193	.096		25.5	362.4
214	.097		25.8	374.1
232	.098		26.1	384.1
251	.099		26.3	394.8
266	.100		26.6	403.1
284	.101		26.8	413.0
297	.102		27.1	420.2

TABLE 3 - TEMPERATURE-RESISTANCE DATA FOR .75 INCH
O. D. GAUGE

Temp °F	V volts	i ma	R ohms	Temp °K
96 ± 1	.555	3.77	147	308.6 ± .6
109	.560		149	315.8
120	.565		150	321.9
130	.570		151	327.4
139	.575		152	332.5
149	.580		154	338.0
160	.585		155	344.0
170	.590		156	349.6
180	.595		158	355.2
191	.600		159	361.4
200	.605		160	366.4
211	.610		162	372.4
224	.615		163	379.9
235	.620		164	385.9
246	.625		166	392.0
255	.630		167	397.0
266	.635		168	403.1
277	.640		170	409.1
288	.645		171	415.2
297	.650		172	420.2

TABLE 4 - VOLTAGE-PRESSURE READINGS FOR .375 INCH
DIAMETER CYLINDER OPERATING IN:

AIR		
i ma	V volts	Pressure mm of Hg
200.0	6.915	3.98×10^2
	7.011	1.232×10^2
	7.061	6.09×10^1
	7.076	3.43×10^1
	7.180	4.1
	7.200	4.5×10^{-1}
	7.254	3.7×10^{-2}
	7.289	1.7×10^{-2}
	7.405	5×10^{-4}
	7.429	3.8×10^{-6}
	7.431	1.8×10^{-6}
CO ₂		
i ma	V volts	Pressure mm of Hg
200.1	7.094	4.7×10^1
	7.130	2.67×10^1
	7.172	1.25×10^1
	7.217	3.4
	7.249	3.5×10^{-1}
	7.256	2.9×10^{-1}
	7.414	4.2×10^{-4}
	7.427	1.4×10^{-5}
	7.433	8.8×10^{-6}
	7.438	3.0×10^{-6}

TABLE 4 - Continued

ARGON

i ma	V volts	Pressure mm of Hg
200.3	7.160	5.71×10^1
	7.195	3.30×10^1
	7.265	4.2
	7.276	3.7×10^{-1}
	7.282	2.0×10^{-1}
	7.440	5.4×10^{-4}
	7.462	5.0×10^{-6}
	7.464	3.5×10^{-6}

HELIUM

i ma	V volts	Pressure mm of Hg
200.1	6.767	1.872×10^2
	6.790	9.07×10^1
	6.809	3.73×10^1
	6.931	1.8×10^{-1}
	7.092	5.0×10^{-2}
	7.429	5.0×10^{-4}
	7.443	1.0×10^{-4}
	7.453	5.0×10^{-6}
	7.469	2.0×10^{-6}

TABLE 5 - VOLTAGE-PRESSURE READINGS FOR .75 INCH O. D. CYLINDER OPERATING WITH DIFFERENT CURRENTS IN AIR

i ma	V volts	Pressure mm of Hg
124.9	20.468	1.169×10^2
	20.639	5.64×10^1
	20.820	2.4×10^1
	21.040	3.8
	21.088	8.0×10^{-1}
	21.144	2.75×10^{-1}
	21.265	3.7×10^{-2}
	21.408	2.8×10^{-2}
	21.728	4.6×10^{-4}
	21.738	3.8×10^{-4}
	21.807	3.4×10^{-6}
	21.804	2.5×10^{-6}
85.1	13.017	6.37×10^2
	13.108	2.96×10^2
	13.215	1.041×10^2
	13.319	2.51×10^1
	13.414	4.3
	13.449	3.0
	13.454	7.5×10^{-1}
	13.478	1.0×10^{-1}
	13.531	3.3×10^{-2}
	13.611	1.0×10^{-2}
	13.700	9.0×10^{-4}
	13.755	2.8×10^{-4}
	13.771	1.0×10^{-4}
	13.788	1.4×10^{-5}

TABLE 5 - Continued

i ma	V volts	Pressure mm of Hg
85.1	13.735	5.6×10^{-6}
	13.797	1.8×10^{-6}
50.0	7.471	2.18×10^2
	7.475	1.045×10^2
	7.494	2.59×10^1
	7.510	4.9
	7.512	1.43
	7.519	1.75×10^{-1}
	7.526	6.2×10^{-2}
	7.549	1.8×10^{-2}
	7.569	2.5×10^{-3}
	7.591	3.4×10^{-4}
	7.600	6.7×10^{-6}
	7.601	3.0×10^{-6}

TABLE 6 - PRESSURE READINGS FOR 1 INCH O. D.
CYLINDER OPERATING IN AIR

i ma	V volts	Pressure mm of Hg
225.0	5.456	6.27×10^2
	5.497	1.65×10^2
	5.545	3.61×10^1
	5.579	4.9
	5.603	3.7×10^{-1}
	5.666	2.6×10^{-2}
	5.727	3.3×10^{-3}
	5.758	6×10^{-4}
	5.794	1×10^{-4}
	5.812	5×10^{-6}

Chapter IV

EXPERIMENTAL RESULTS AND DISCUSSION

The mechanisms of heat transfer from the cylinder include radiation, conduction through the gas, convection, and conduction through the leads. Figure 2 shows a typical example of these effects

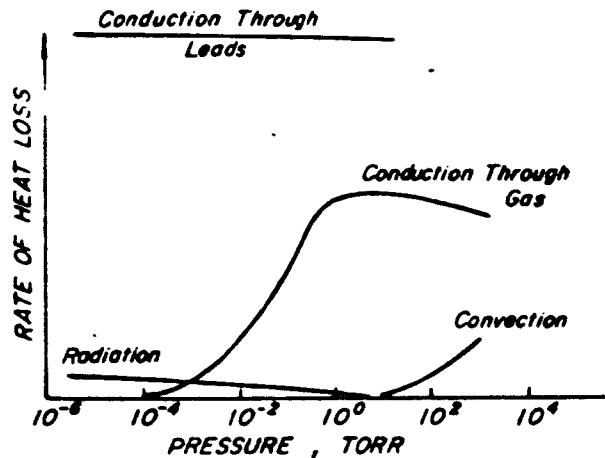


Figure 2 - Rate of heat loss due to the different mechanisms of heat transfer

when the cylinder is operated with constant current, i. e., as the pressure is lowered the cylinder temperature increases because there are fewer molecules present to carry away energy.

If the cylinder had been operated at constant temperature, radiation and the loss of heat through the leads would have been constant since they are independent of pressure. The main interest, then, is in the loss of heat by conduction through the gas, which is dependent on pressure.

From Equation 1

$$q_m = 2\pi r_1 l K_m a P (T_1 - T_2)$$

it can be seen that molecular conduction depends directly on the radius of the cylinder. Large diameter cylinders were therefore used to increase the sensitive range of the Pirani gauge. Figure 6 illustrates the effect of the large diameter. In the molecular ($P < 10^{-3}$ torr) and transmolecular (10^{-3} torr $< P < 1$ torr) regions, the advantage of a large diameter gauge amounts to approximately a hundred-fold increase in conduction. Although the larger radius helps, molecular conduction decreases very rapidly with decreasing pressure (Figures 6 and 7). Hence, it is to be expected that from 10^{-4} to 10^{-6} torr the temperature would change only slightly. This proved to be true as seen in Figures 8, 9, 10, and 11.

In Equation 2

$$K_m = \frac{C_v + R/2}{\sqrt{2\pi R M T_2}}$$

the dependence of molecular conductivity on the mass of the gas can be seen. For a heavier gas the molecular conductivity will be less, or the temperature more nearly constant throughout the pressure range. This effect is illustrated in Figures 10 and 11. It must be remembered, however, that different gases have different accommodation coefficients with respect to a particular

APPENDICES

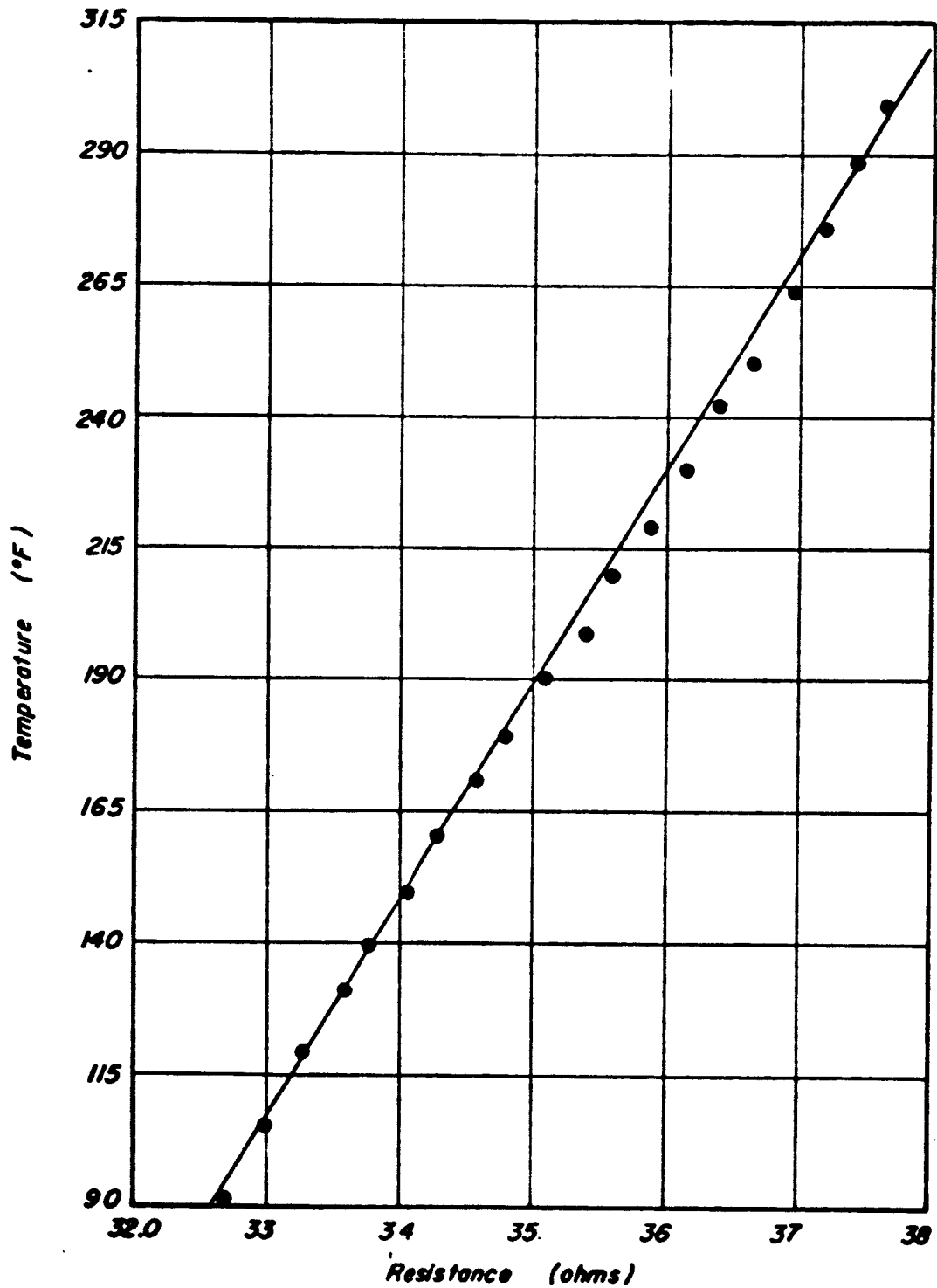


**Fig. 4 Value of resistance for different temps.
of 0.375 inch diameter gauge.**

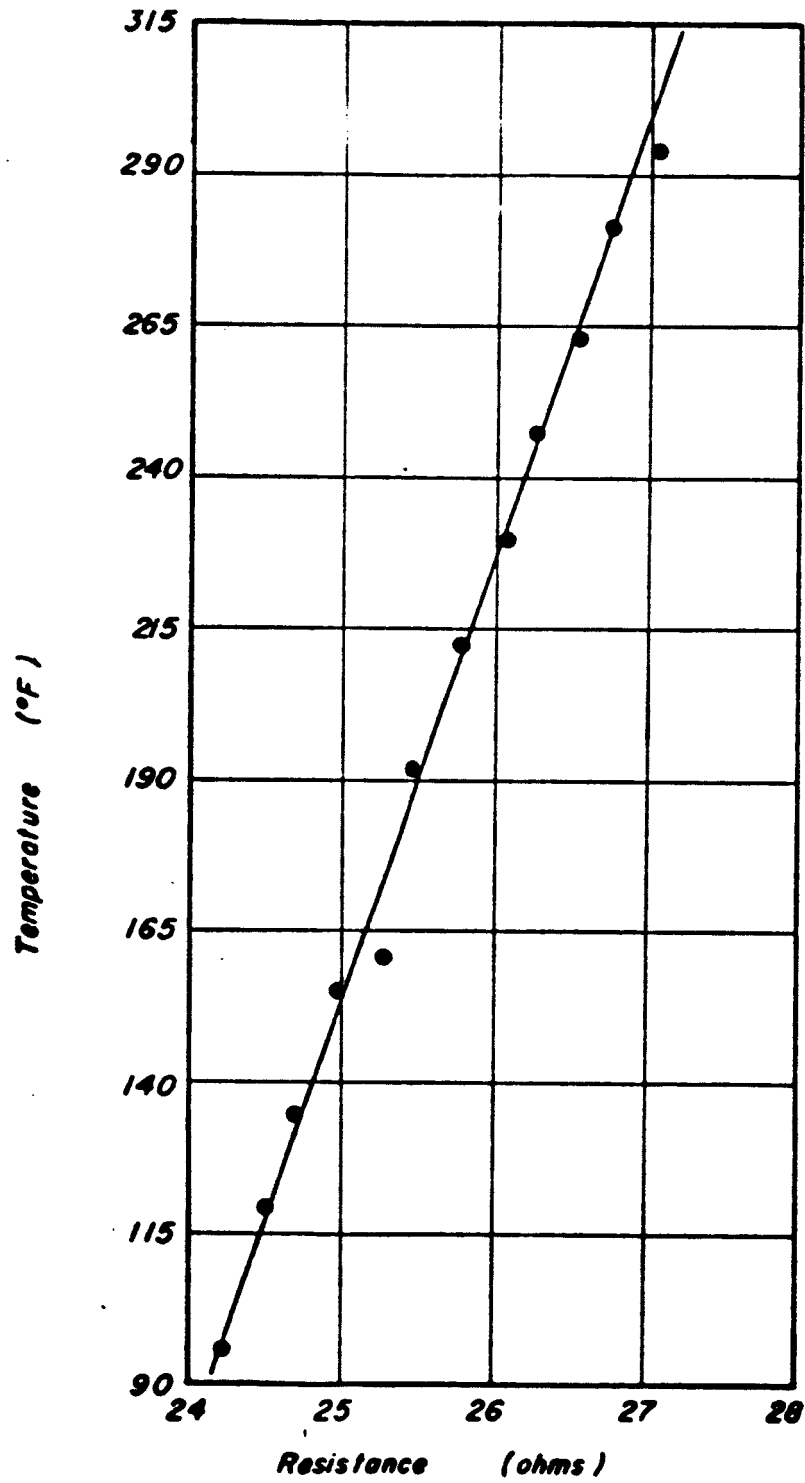


Fig. 5 Value of resistance for different temps. of 1 inch Q.D. gauge.

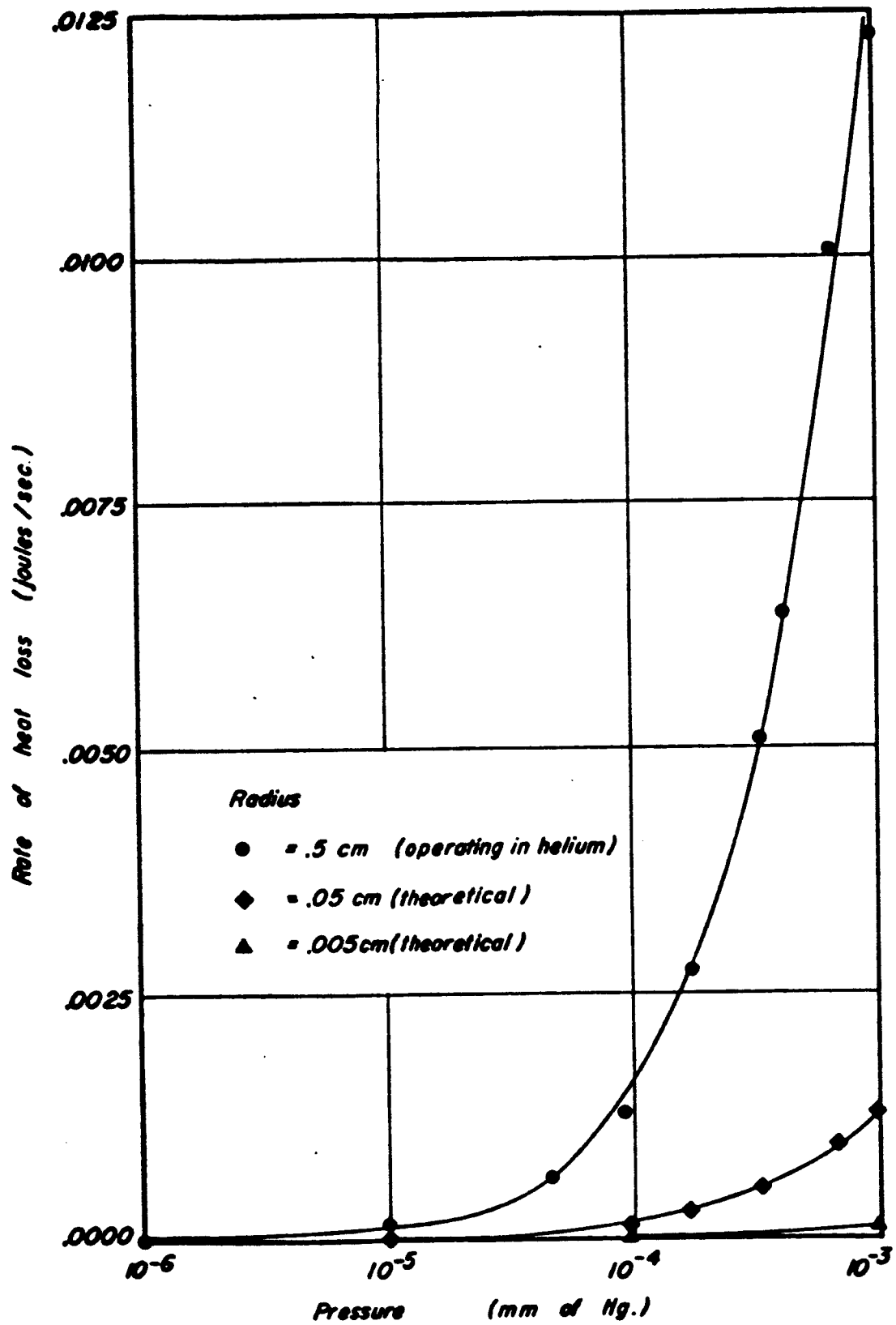


Fig. 6 Effect radius has on rate of heat loss due to molecular conduction.

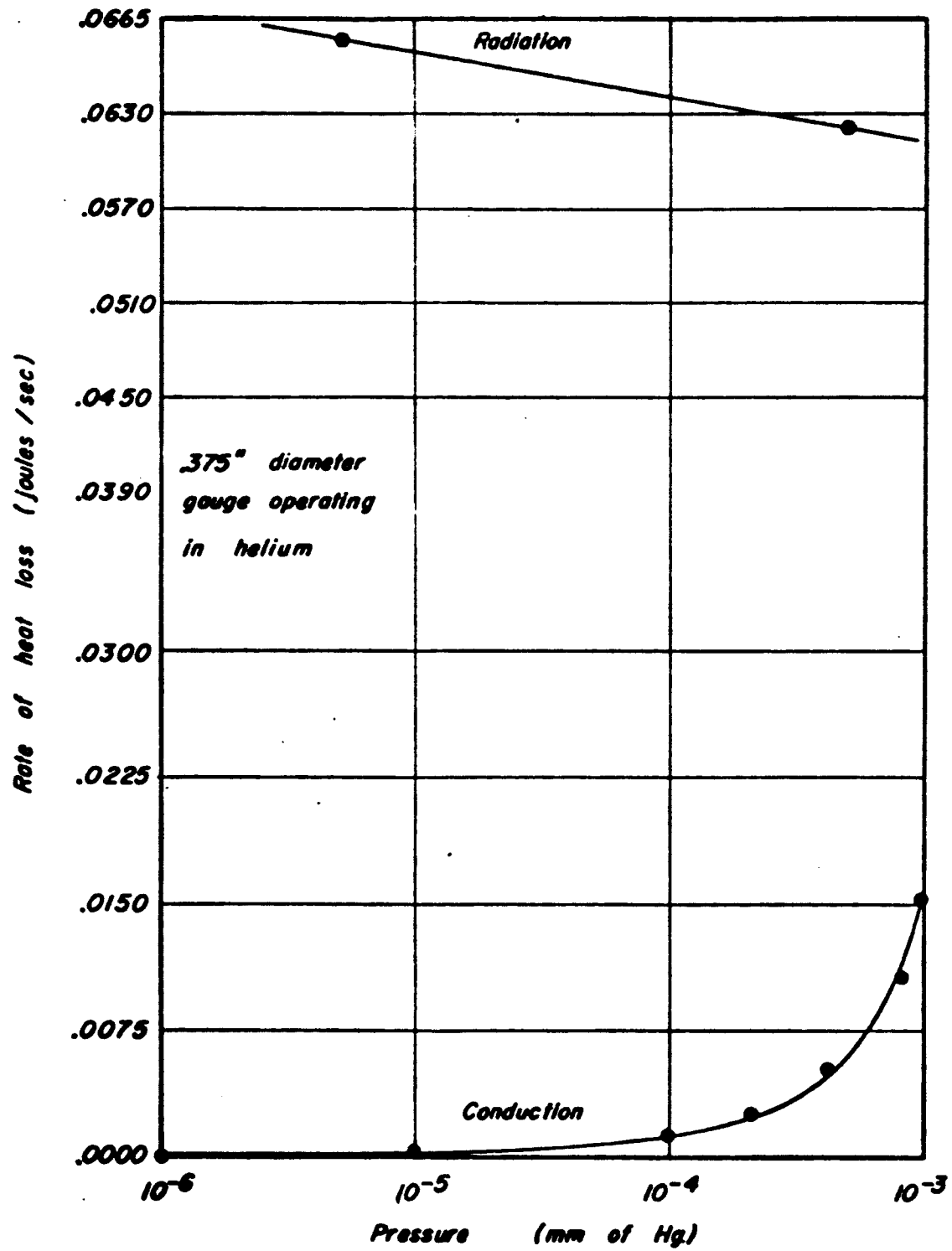


Fig. 7 Example of changing rate of heat loss due to molecular conduction and radiation.

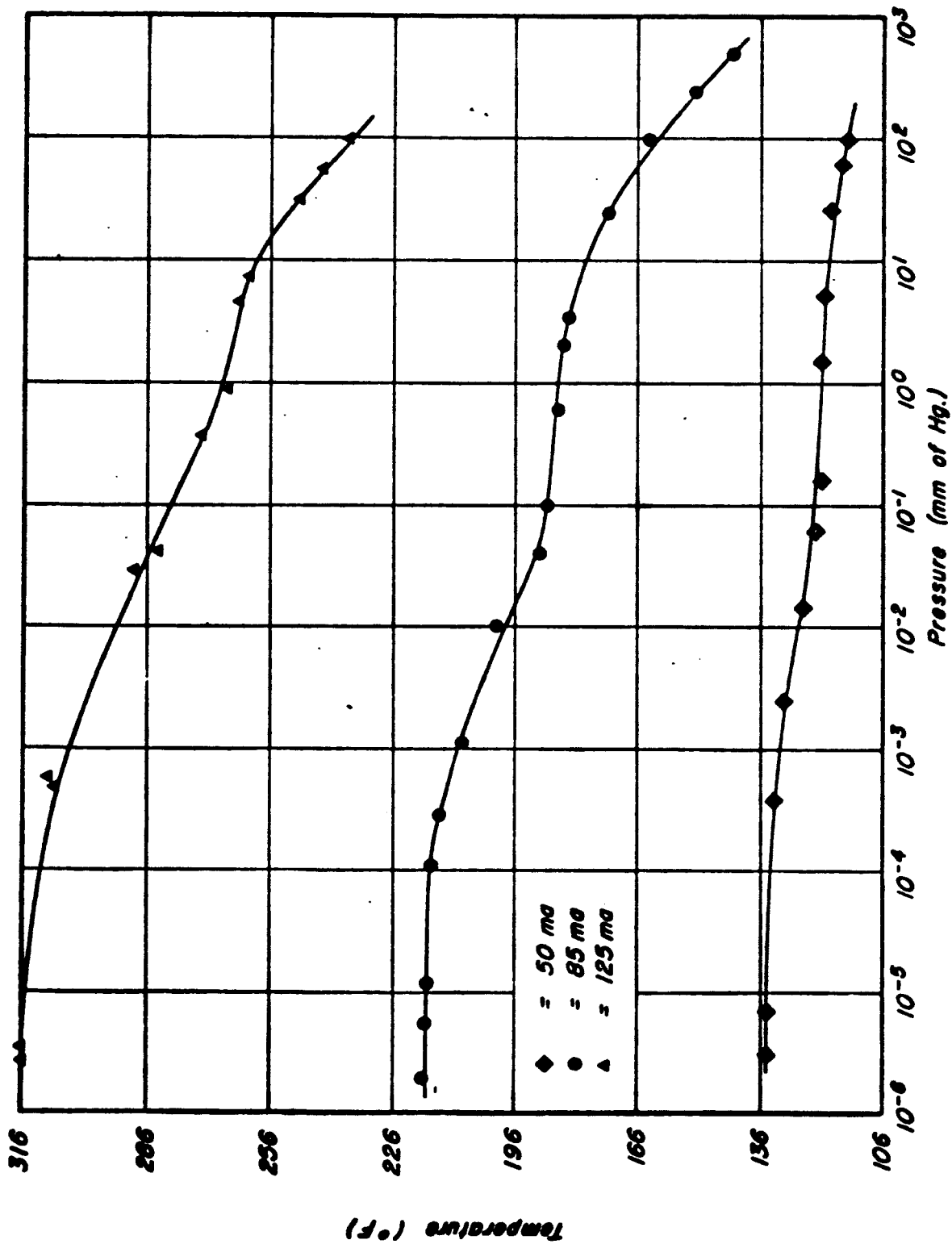


Fig. 8 Temperature of .75 inch O. D. guage operating with different currents in air.

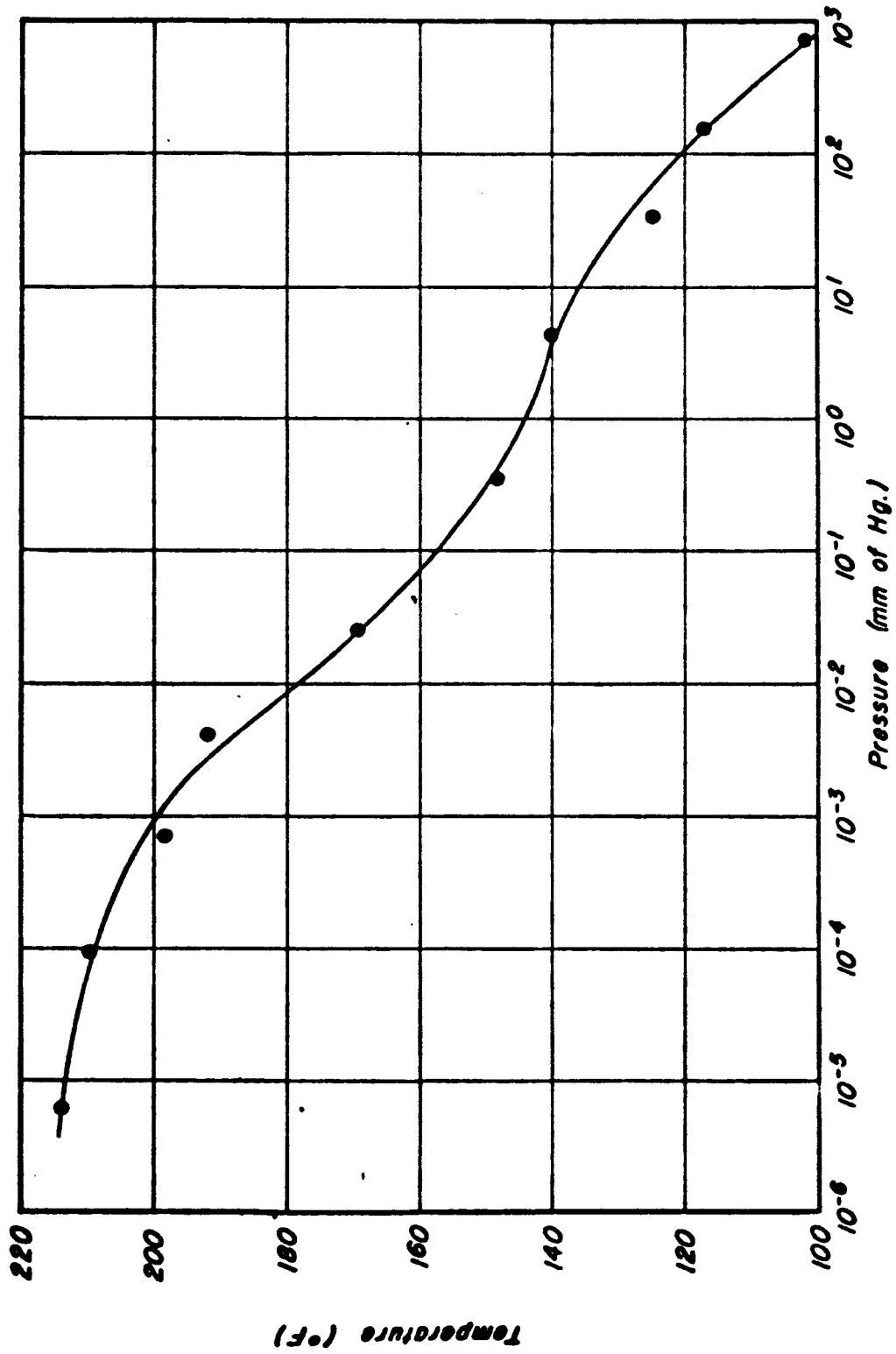


Fig. 9 Temperature of 1 inch O.D. gauge operating in air.

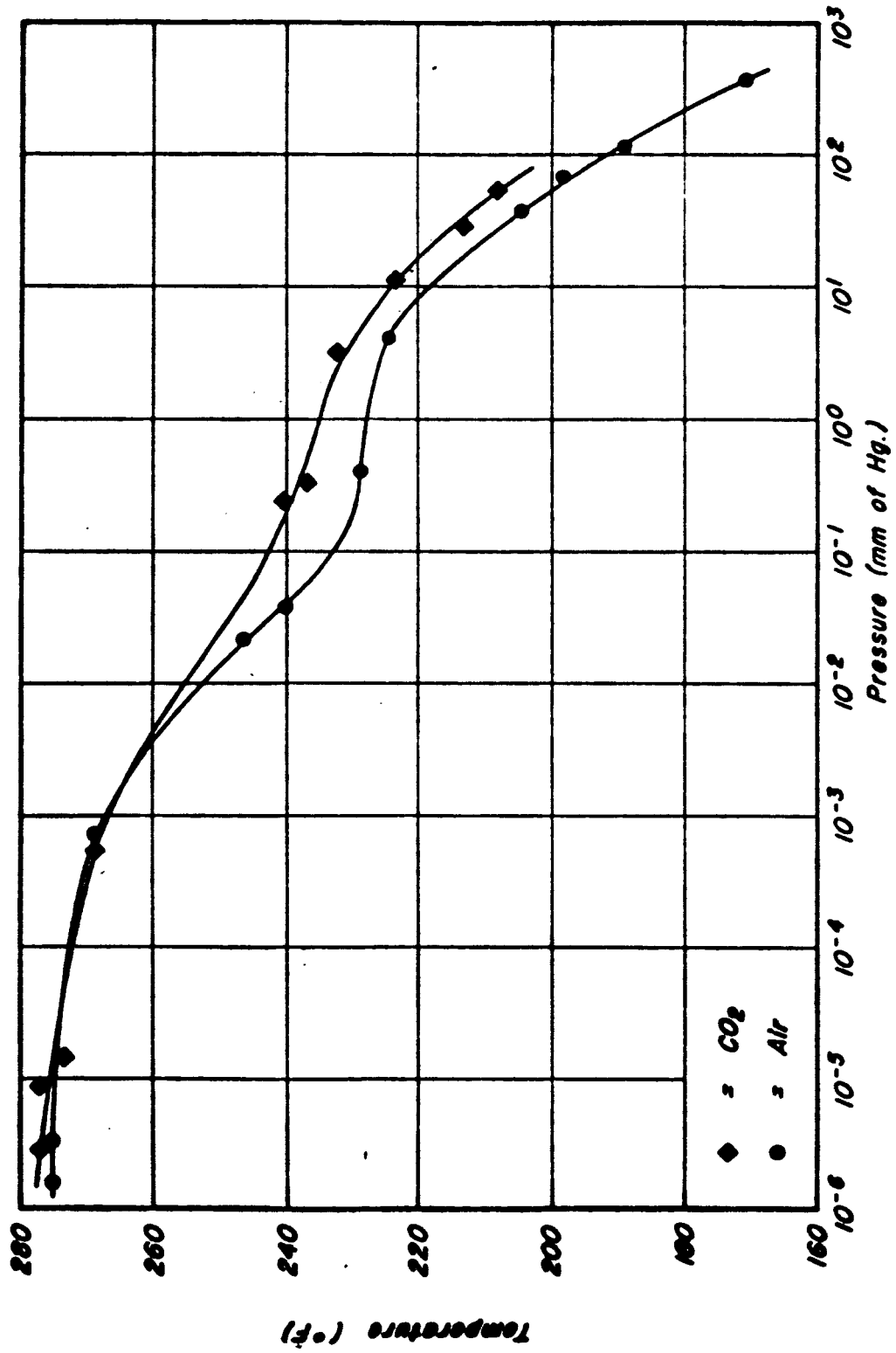


Fig. 10 Temperature of .375 inch diameter guage operating in CO₂ and air.

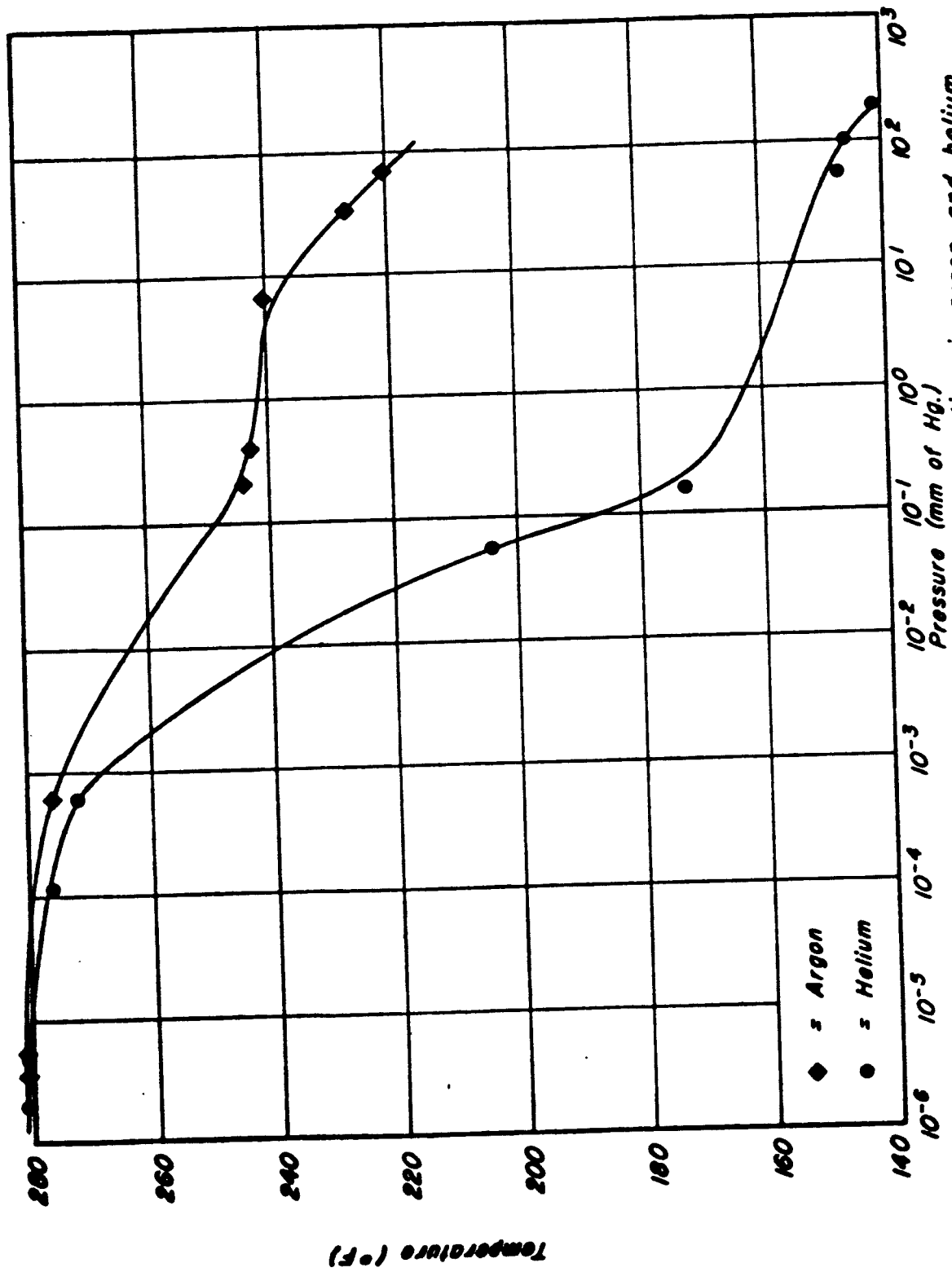


Fig. 11 Temperature of .375 inch diameter gauge operating in argon and helium.

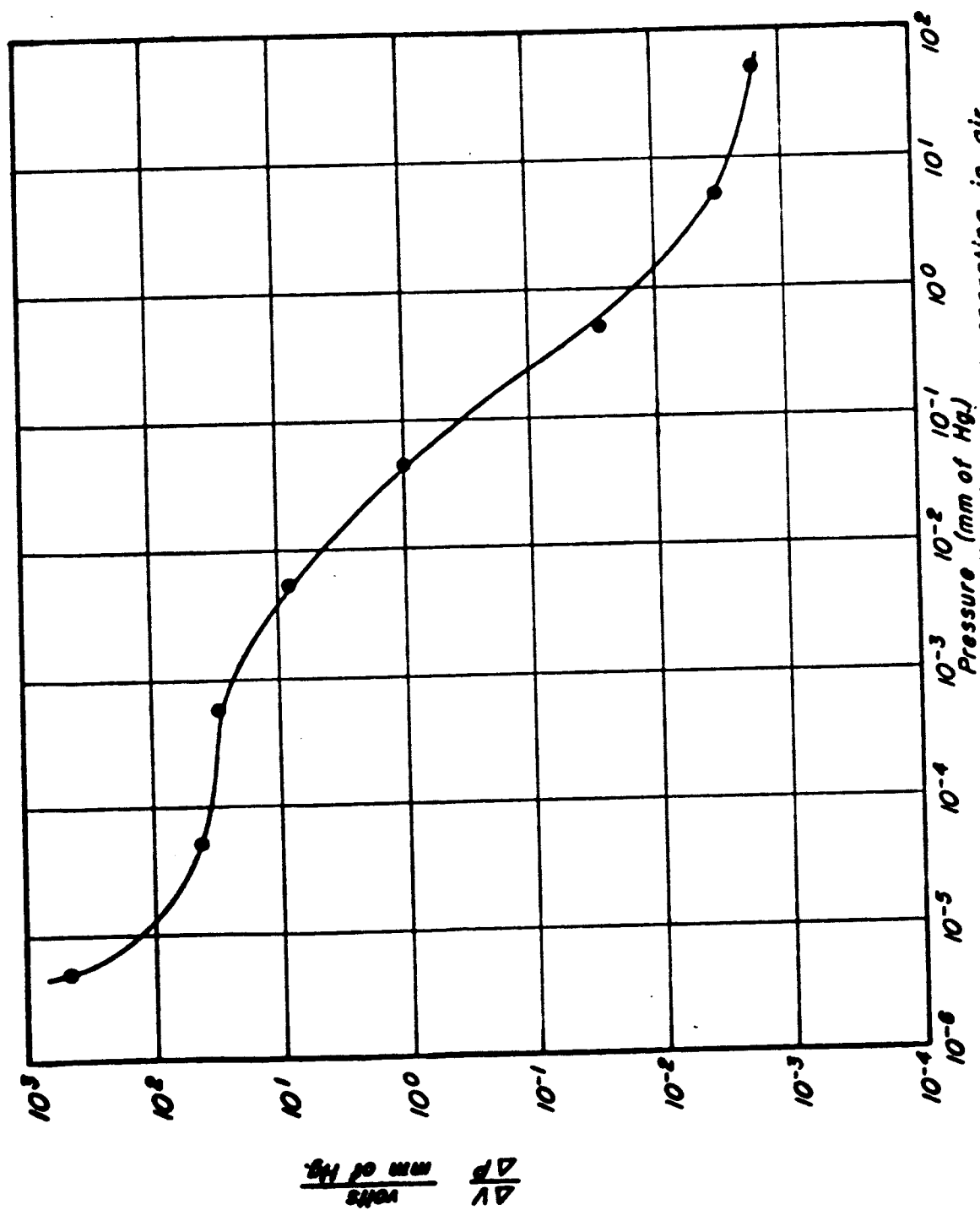


Fig. 12 Sensitivity of .375 inch diameter guage operating in air.

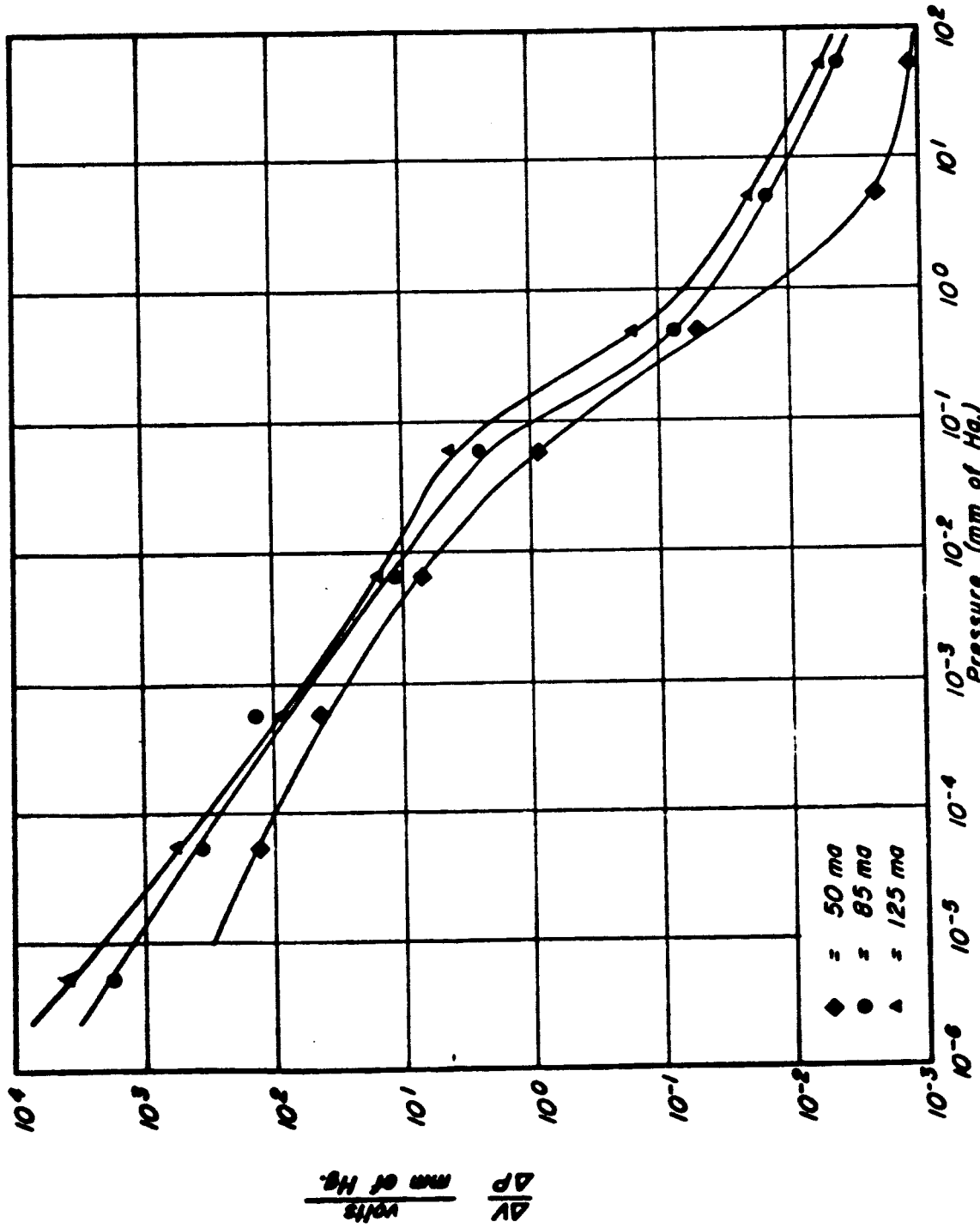


Fig. 13 Sensitivity of .75 inch O.D. gauge operating in different currents in air.

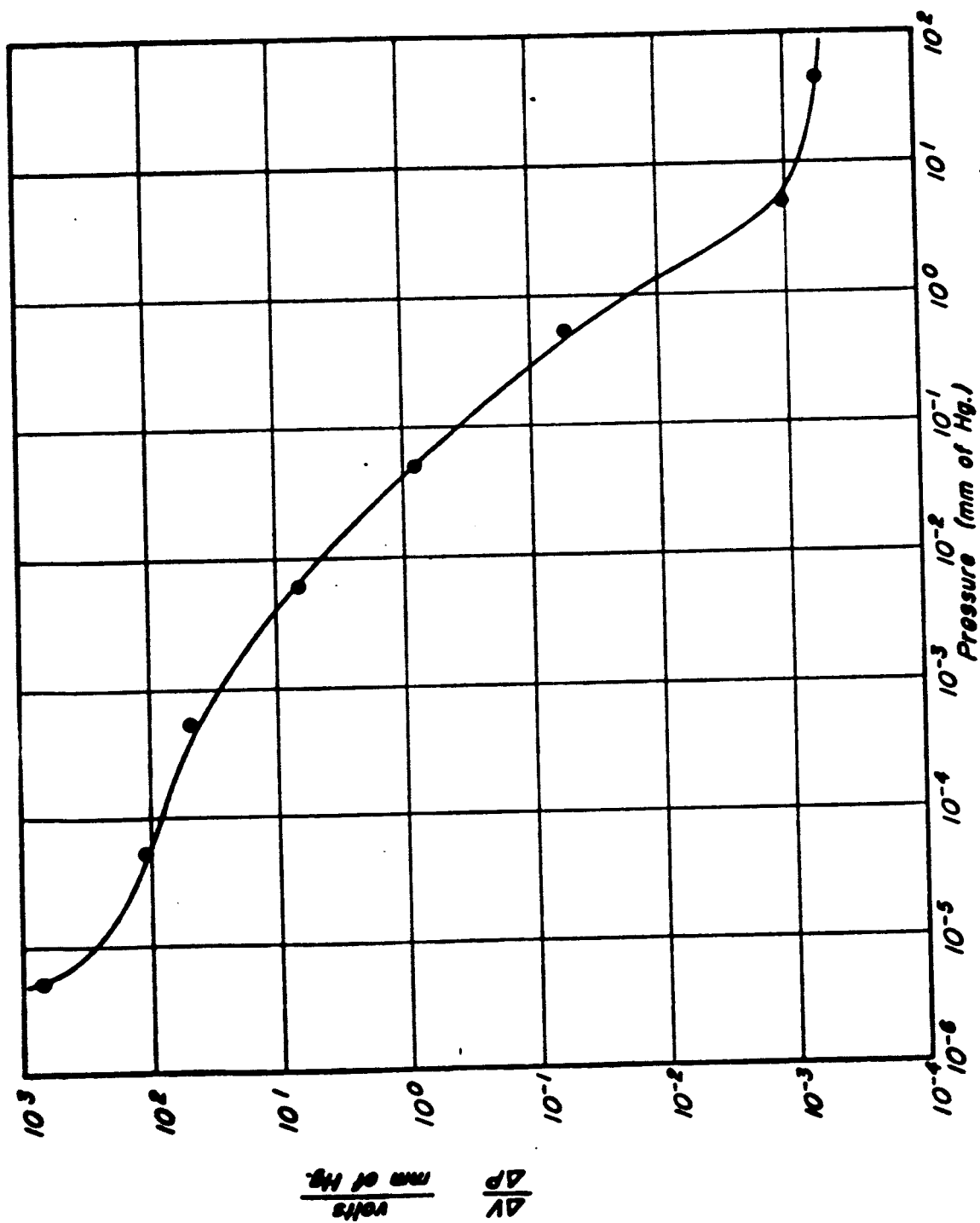


Fig. 14 Sensitivity of 1 inch O.D. guage operating in air.

surface (Table 7) which also affects molecular conductivity (Equation 1). Von Ubisch (7) gives the values found in Table 7 for the different gases indicated.

TABLE 7 - CONSTANTS INVOLVED IN THE EQUATION OF HEAT TRANSFER

	a_{Pt}	M	γ	K_m^*	n^{**}
He	.484	4.00	1.667	28.5	186.0
A	1.00	39.9	1.667	8.98	209.6
CO ₂	.866	44.01	1.304	16.69	139.0
O ₂	.933	32.00	1.401	15.11	189.0
N ₂	.917	28.02	1.404	16.00	178.1

* 10^{-3} watts cm^{-2} $^{\circ}\text{K}^{-1}$ per mm of mercury

** micropoises ($\text{dyne sec/cm}^2 \times 10^{-6}$) at 0°C

Another parameter of molecular conductivity is the temperature difference between the cylinder and gas. Optimum sensitivity to pressure change can be greatly influenced by the choice of the temperature of the cylinder as shown in Figures 8 and 13. The temperature needs to be high to maximize molecular conduction but low to reduce radiation which is varying as T_1^4 (Equation 3).

Radiation and conduction through the leads become the dominant processes in the heat transfer at low pressures. Radiation can be used as the pressure sensing mechanism if the gauge is operated properly, as pointed out in Appendix B.

In the molar region ($\lambda < r_1$), only small temperature changes with pressure are again expected due to the slight dependence of conductivity on pressure (Equations 8 and 9). This is true until convection begins to play a dominate role, at which point the temperature dependence increases. Again these conclusions are verified in Figures 8, 9, 10, and 11.

In summary, it has been shown that the temperature of the cylinder is dependent on the pressure. As the pressure decreases from atmospheric, large temperature changes are seen due to convection. Then small increases in temperature are seen, as convection becomes negligible, due to the slight dependence of conduction on pressure. The temperature again increases rapidly in the transmolecular region ($r_1 < \lambda < r_2$) because the energy conducted away is decreasing as $\frac{P}{1 + \sigma P}$. In the molecular region ($\lambda \geq r_2$), the temperature is approaching a constant value since gas conduction is now directly dependent on pressure and therefore almost zero.

Concluding Remarks

Heat transfer from a cylinder in a symmetrical chamber was investigated for dependence on pressure, size and temperature of the cylinder, and molecular weight of the gas. The system resembles the Pirani-type pressure gauge. An important deviation, however, was the use of thin films on large diameter (on the

order of 2 cm.) cylindrical substrates as the heating and sensing element. This large diameter enhanced the molecular conductivity, and hence, the sensitive pressure range. Although the temperature of the cylinder is almost constant in the 10^{-4} to 10^{-6} torr range, the potential difference, and hence readability, is still increasing with decreasing pressure in this range (Tables 4, 5, and 6). Thus, the useful range of such a gauge has been extended two orders of magnitude, 10 to 10^{-6} torr. It appears from the results of Appendix B that, with the appropriate temperature difference, the useful range could be extended even lower in future work.

Appendix A

DERIVATION OF EQUATION FOR CONDUCTION

The derivations of equations for conduction in both the molecular and molar regions are given in this appendix. Included also, is a discussion of the temperature jump and jump distance g .

To derive the equations for molecular conductivity (Equations 1 and 2), consider an element of the wall of the gauge of area dA .

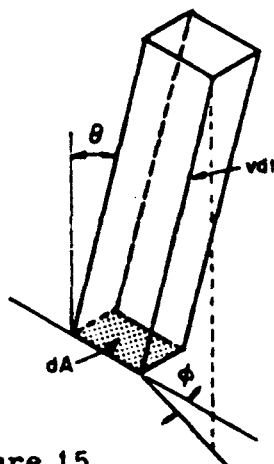


Figure 15
Oblique Cylinder

Let the normal to the wall be the polar axis and construct the oblique cylinder shown in Figure 15. This cylinder is slanted in the θ, ϕ - direction and its length is $v dt$. Assuming for the moment that all the

molecules have the same speed v , we see that any molecule in the cylinder moving in the θ, ϕ - direction will strike area dA in time dt .

Using the fact that

$$\bar{Q} = \frac{\int Q f(v) dv}{\int f(v) dv}$$

where $f(v)$ is the Maxwell-Boltzmann velocity distribution function, we can find the average kinetic energy per molecule;

$$\overline{\text{K.E.}} = \frac{\int \frac{mv^2}{2} (Be^{-v^2/v_0^2}) (v \, dt \, dA \cos\theta) (v^2 \sin\theta \, d\theta \, d\phi \, dv)}{\int Be^{-v^2/v_0^2} (v \, dt \, dA \cos\theta) (v^2 \sin\theta \, d\theta \, d\phi \, dv)}$$

where v_0 is the most probable speed and equal to $\sqrt{\frac{2kT}{m}}$, and B is a constant.

$$\begin{aligned} \overline{\text{K.E.}} &= \frac{\frac{mB}{2} \int_0^{2\pi} d\phi \int_0^{\pi/2} \cos\theta \sin\theta \, d\theta \int_0^\infty v^5 e^{-v^2/v_0^2} \, dv}{B \int_0^{2\pi} d\phi \int_0^{\pi/2} \cos\theta \sin\theta \, d\theta \int_0^\infty v^3 e^{-v^2/v_0^2} \, dv} \\ &= \frac{2\pi(1/2) \frac{m}{2} \int_0^\infty v^5 e^{-v^2/v_0^2} \, dv}{2\pi(1/2) \int_0^\infty v^3 e^{-v^2/v_0^2} \, dv} \\ &= \frac{\frac{m}{2} \int_0^\infty v_0^5 u^{5/2} e^{-u} \frac{v_0 u^{-1/2}}{2} \, du}{\int_0^\infty v_0^3 u^{3/2} e^{-u} \left[\frac{v_0 u^{-1/2}}{2} \right] \, du} \end{aligned}$$

where $u = \frac{v^2}{v_0^2}$

$$= \frac{mv_0^2}{2} \frac{\int_0^\infty u^2 e^{-u} du}{\int_0^\infty u^{2/2} e^{-u} du}$$

$$= \frac{mv_0^2}{2} \frac{\Gamma(3)}{\Gamma(2)}$$

$$= mv_0^2$$

$$= m \left(\frac{2kT}{m} \right)$$

$$= 2kT$$

Consider, now, a molecule striking the wall of the gauge with kinetic energy corresponding to temperature T_2 and leaving with energy corresponding to T_k . With each fully accomplished molecule impact the gauge will lose the amount of energy

$$2k(T_k - T_2)$$

The number of collisions per unit area per unit time is

$$\frac{1}{4} n \bar{v}_2$$

where \bar{v}_2 is the average speed of the molecules and n is the number of molecules per unit volume. The amount of heat, therefore, that the gauge gives off to the surrounding gas

per unit area per unit time is

$$\begin{aligned}\frac{q_m}{\text{area}} &= 2k(T_k - T_2) \frac{1}{4} \bar{n} \bar{v}_2 \\ &= \frac{1}{2} k \bar{n} \bar{v}_2 (T_k - T_2)\end{aligned}\quad (10)$$

In 1911, Knudsen (8) introduced what he called the coefficient of accommodation, a . This coefficient accounts for the fact that the molecules which fall on the surface do not necessarily acquire the energy corresponding to the temperature of the surface before they are reflected. If E_2 denotes the energy brought up to a unit area per second by the incident stream, and E_k that carried away by these molecules as they leave the wall after reflection from it, and if E_1 is the energy that this latter stream would carry away if it carried the same mean energy per molecule as does a stream issuing from a gas in equilibrium at wall temperature T_1 , then a is given by the equation

$$a = \frac{E_k - E_2}{E_1 - E_2}$$

Knudsen preferred to attach a temperature to each of these streams of molecules. He wrote the equivalent of the equation as

$$a = \frac{T_k - T_2}{T_1 - T_2}$$

Using this definition and the fact that

$$P = \frac{1}{3} mn (v_{RMS})^2 = \frac{mn}{2} (v_0^2)_2$$

Equation 10 becomes

$$\begin{aligned} \frac{q_m}{\text{area}} &= \frac{1}{2} kn \bar{v}_2 a (T_1 - T_2) \\ &= \frac{k \bar{v}_2}{m(v_0^2)_2} a P (T_1 - T_2) \\ &= K_m a P (T_1 - T_2) \end{aligned}$$

or

$$q_m = 2\pi r_1 l K_m a P (T_1 - T_2) \quad (1)$$

where

$$K_m = \frac{k \bar{v}_2}{m(v_0^2)_2} = \frac{k}{m(v_0^2)_2} \frac{2(v_0)_2}{\sqrt{\pi}} \quad (2')$$

$$= \frac{2k}{m\sqrt{\pi}} \sqrt{\frac{m}{2kT_2}} = \frac{2R}{M} \sqrt{\frac{mN}{2\pi RT_2}}$$

$$= \frac{2R}{\sqrt{2\pi RMT_2}} = \frac{C_v + \frac{1}{2} R}{\sqrt{2\pi RMT_2}} \quad (2)$$

Equation 7 is the integrated form of the thermal conductivity equation

$$q_k = -2\pi r l K_v \frac{dT}{dr}$$

$$\int_{r_1}^{r_2} \frac{q_k}{2\pi r l} dr = - \int_{T_1}^{T_2} K_v dT$$

$$\frac{q_k}{2\pi l} \ln \frac{r_2}{r_1} = - K_v (T_2 - T_1)$$

$$q_k = \frac{2\pi l K_v (T_1 - T_2)}{\ln \frac{r_2}{r_1}}$$

However, at a wall bounding an unequally heated gas there is a discontinuity of temperatures due to the geometrical restriction laid upon the movement of the gas molecules. As a result a "temperature jump" develops between the surface and the adjacent layer of gas. (Figure 16) The temperature in the gas between the

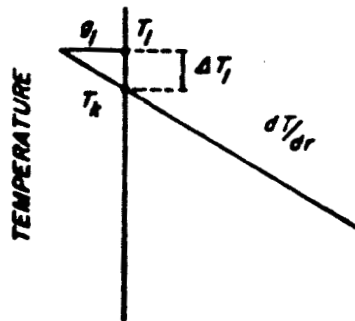


Figure 16 - The temperature jump

walls is given by the straight oblique line in Figure 16. The temperature jump, ΔT , is defined as shown in the same figure. The jump is related to the jump distance g by

$$\Delta T_1 = g_1 \frac{dT}{dr}$$

From Figure 16

$$\Delta T_1 = g_1 \frac{dT}{dr} = T_1 - T_k \quad (11)$$

In equation (10) the difference between the energy carried by two streams of molecules issuing from gases at temperature T_1 and T_k was found to be

$$\frac{1}{2} kn\bar{v}_k (T_1 - T_k)$$

where T_k is the temperature of the gas next to the wall if the temperature gradient were uniform, as shown in Figure 16. \bar{v}_k is the corresponding average speed.

If we then add to the above expression the excess energy carried by the incident stream as its contribution to the conduction, we have the difference between the incident energy and the energy carried away by the molecules on the assumption that they leave as a Maxwellian stream at the wall temperature T_1 , or

$$E_1 - E_k = \frac{1}{2} K_v \frac{dT}{dr} + \frac{1}{2} kn\bar{v}_k (T_1 - T_k)$$

On the other hand the net energy actually delivered to the surface is

$$E_0 - E_k = K_v \frac{dT}{dr}$$

and since

$$E_0 - E_k = a(E_1 - E_k)$$

$$K_v \frac{dT}{dr} = a \left[\frac{1}{2} K_v \frac{dT}{dr} + \frac{1}{2} kn\bar{v}_k (T_1 - T_k) \right]$$

from Equation 11

$$K_v = \frac{a}{2} \left[K_v + kn\bar{v}_k g \right]$$

$$g = \left[\frac{2K_v}{a} - K_v \right] \left[kn\bar{v}_k \right]^{-1}$$

$$= K_v \left[\frac{2-a}{a} \right] \left[kn\bar{v}_k \right]^{-1}$$

$$= \left[\frac{2-a}{a} \right] \frac{mv_0^2 K_v}{2k\bar{v}_k P}$$

from Equations 2' and 2

$$= \left[\frac{2-a}{a} \right] \frac{\sqrt{2\pi RMT_k}}{C_v + \frac{1}{2}R} \frac{K_v}{2P}$$

or

$$= \left[\frac{2-a}{a} \right] \frac{mv_{0k}^2}{k\bar{v}_k} K_v \left[mnv_{0k}^2 \right]^{-1}$$

$$= \left[\frac{2-a}{a} \right] K_v \frac{mc\lambda}{kn}$$

where n' is the viscosity coefficient equal to

$$n' = C\rho\bar{v}\lambda$$

$$0.491 \leq C \leq 0.499$$

Appendix B

DERIVATION SHOWING POSSIBILITY FOR
EXTENDING SENSITIVE RANGE OF GAUGE

Consider a gauge with only molecular and radiation heat loss.

The energy balance may be written as

$$i^2 R = \gamma'(T_1^4 - T_2^4) + \alpha'P(T_1 - T_2) = i^2 R_2 \left[1 + \alpha(T_1 - T_2) \right]$$

where R_2 is the resistance at temperature T_2 . For constant current operation, the sensitivity is

$$\frac{dT}{dP} = \frac{\alpha'(T_1 - T_2)}{4\gamma'T_1^3 + \alpha'P - i^2 R_2 \alpha}$$

In the molecular region where P is small, $4\gamma'T_1^3 \gg \alpha'P$. Likewise if the gas temperature, T_2 , is near absolute zero, then $R_2 \rightarrow 0$, and the term $i^2 R_2 \alpha$ is neglected compared to $4\gamma'T_1^3$.

Hence

$$\frac{dT}{dP} \approx \beta \frac{(T_1 - T_2)}{T_1^3}$$

where β is a constant. The expression on the right-hand side of

this equation has a maximum value for $T_1 = \frac{3}{2} T_2$, or

$$\left[\frac{dT}{dP} \right]_{\max} = \frac{\beta'}{T_2^2}$$

Thus, the maximum sensitivity occurs when the temperature of the outside wall of the gauge is as low as possible. This result was obtained by Ellett and Zable (4) for the case of constant power.

LIST OF REFERENCES

1. Pirani, M., "Selbstzergehendes Vakuum-Messinstrument", *Verh. der Deutsch. Phys. Ges.* 8:686, 1906.
2. Dushman, S. and J. M. Lafferty, Scientific Foundations of Vacuum Techniques, John Wiley and Sons, Inc., New York, 1962, 2nd ed., Chap. 5.
3. Pirani, M. and J. Yarwood, Principles of Vacuum Engineering, Reinhold Publishing Corporation, New York, 1963, 2nd ed., p. 83.
4. Ellett, A. and R. M. Zable, "The Pirani Gauge for the Measurement of Small Changes of Pressure", *Phys. Rev.* 37: 1102-1112, 1931.
5. Sandborn, V. A., Private communication.
6. Ubisch, H. Von, "Das moderne Hitzdrahtmanometer", *Vakuum-Technik* 6:175, 1957.
7. Ubisch, H. Von, "On the Conduction of Heat in Rarefied Gases and its Manometric Application I", *Appl. Sci. Res.* A2: 364-403, 1951.
8. Knudsen, M., The Kinetic Theory of Gases, John Wiley and Sons, Inc., New York, 1950, 3rd ed., p. 47.